THE UNIVERSITY *of* EDINBURGH

Concussion in Non-Helmeted Contact Sports: Locating and Measuring Impact on the Head

Jazim Sohail

Doctor of Philosophy

THE UNIVERSITY OF EDINBURGH

2024

Abstract

Mild traumatic brain injury (mTBI) within contact sports is a growing concern due to the serious risk it presents. Extensive research is being conducted looking into head kinematics during impacts in non-helmeted contact sports utilising instrumented mouthguards, allowing researchers to record accelerations and velocities of the head during and after an impact. This research partially focused on conducting a feasibility study of a new instrumented mouthguard to determine its suitability for professional rugby. The mouthguard, developed by Force Impact Technologies, was tested over a 5-month period with Edinburgh Rugby during matches and training sessions. The study concluded that the mouthguard was not fit for purpose in its current form, as the on-field study revealed concerning outputs.

Additionally, instrumented mouthguards utilised within research lack the ability to determine the location of the impact on the head. Therefore, this thesis proposes and validates two methods to determine impact locations to aid the research work being conducted with instrumented mouthguards in the battle against mTBI. One method proposed utilises rigid body dynamics to approximate the impact force and determines its exact location as well as the orientation from instrumented mouthguard kinematic data. The other uses machine learning clustering algorithms with a features data set consisting of features obtained from instrumented mouthguard signals to determine impact location regions on the head. Impact data recorded from finite element simulations were used to validate both methodologies with the results from validation studies highlighting the effectiveness of the proposed impact location algorithms. Impact locations were calculated within 12 mm of the impact center for all conducted tests while utilising rigid body dynamics whereas the clustering methodology correctly classified 100% of all simulated tests to the correct impact region. Additionally, components of force unit vectors (direction cosines) obtained from the algorithm utilising rigid body dynamics were within ± 0.03 of the components of applied force unit vectors, highlighting the accuracy of the proposed algorithm. The algorithms have the potential to significantly aid researchers conducting field tests within non-helmeted sports by reducing the time required to analyse and determine head impact locations.

Lay Summary

Contact sports are played worldwide in many forms, with Rugby, American Football and Soccer being the most popular ones. As exciting as contact sports are, they house a risk of injuries to the players that take part in them, the most severe of which are head injuries. Concussion is a form of head injury, which players sustain by hitting their head with an object or another players head/body. The severe nature of the long term effects of concussion is why understanding concussion is essential within contact sports currently, leading to the need for the research presented in this thesis.

This research's aim was to understand how well one of the devices used to measure head movements after it has been struck performs and whether it was suitable for the professional rugby environment. Additionally, this research looked at developing methods to determine where on the head the impact occurred from the head motion data that was captured, which would allow a better understanding of head impacts/concussions sustained by players. Two methods were developed, proposed and tested within this research to successfully achieve this.

The work presented in this research provides great value to the research field, and will hopefully aid the push to make contact sports safer for participants.

Acknowledgements

I'd like to thank my supervisor Dr Filipe Teixeira-Dias for being so supportive throughout my PhD. He helped me whenever it was required especially through the tough period of the pandemic which altered the PhD project significantly. Additionally I'd like to thank my parents who were very supportive of my passion to study within this field, and my wife Hiba who helped me with the highs and lows that came with the project. Furthermore, I'd like to thank my friends Sam Thompson and Charlotte Mitchell who guided me through a very difficult part of my research. Moreover, I would like to thank PhD partners Force Impact Technologies, who not only provided the desired technology to allow the data collection process, but were very supportive throughout the project with any issues I had, and were generally a pleasure to work with.

Finally, I'd like to thank the University of Edinburgh and EPSRC for supporting me throughout my research financially as well as with anything that was required for me to conduct my project. I wouldn't have been able to conduct my PhD without either of them.

Declaration

I declare that this thesis was composed by myself, that the work contained herein is my own except where explicitly stated otherwise in the text, and that this work has not been submitted for any other degree or professional qualification except as specified.

Jazim Sohail

Contents

Figures and Tables

Figures

Tables

Nomenclature

$\ddot{\boldsymbol{x}}$	Acceleration vector
$\boldsymbol{\delta}$	Tolerance vector
$\dot{\boldsymbol{\omega}}$	Rotational acceleration vector
$\hat{\boldsymbol{F}}_{\boldsymbol{s}}$	Applied force unit vector (numerical)
$\hat{\boldsymbol{F}}_{\boldsymbol{t}}$	Approximated force unit vector
$\boldsymbol{\omega}$	Rotational velocity vector
$\boldsymbol{a}_M$	Linear acceleration vector at mouthguard
$\boldsymbol{a}_{Cog}$	Linear acceleration vector at centre of gravity
$\boldsymbol{a}$	Linear acceleration vector
$\boldsymbol{F}_t$	Approximated force vector
$\boldsymbol{F}$	External force vector
$\boldsymbol{u}$	Initial Velocity vector
μ	cluster membership value
ρ	density
C_{pq}	Hyper-elastic rubber constants
C	Number of clusters for C-Means clustering
c	cluster centroid
$E1$	Young's Modulus components for viscous foam
$E2$	Young's Modulus components for viscous foam
E	Young's Modulus
J_{se}	Squared error function
J	Relative volume
K	Number of clusters for K-Means clustering
m	fuzziness index
n	number of cases
PLA	Peak linear acceleration
SD	Standard Deviation
t	Time
v	Poisson ratio
W_h	Hydrostatic work
W	Work from hyper-elastic constitutive law
w	Natural frequency
$-_x$	x component of a vector
$-_y$	y component of a vector
$-_z$	z component of a vector

a	Linear acceleration vector (numerical)
d	Distance vector from mouth to centre of gravity
Q	Modal force vector
r	Distance vector from centre of gravity to surface of head
T_t	Moment vector (from torque equation)
T	Euler's moment vector
x	Displacement vector
K	Global stiffness matrix
k	Local stiffness matrix
M	Global inertia matrix
m	Local inertia matrix
X	Modal shape matrix

Chapter 1

Introduction

1.1 What is Concussion?

Mild Traumatic Brain Injury (mTBI), also known as concussion, is a serious injury affecting people in the workplace, soldiers and athletes (Laker, 2011). There is no unified definition of concussion, but broadly it is agreed to be *"an alteration in brain function, or other evidence of brain pathology, caused by an external force"* (Menon, Schwab, Wright, Maas, et al., 2010) or more broadly, *"trauma induced alterations in mental functioning"* (Ommaya & Gennarelli, 1974). It can be caused by a variety of mechanisms such as impact, penetration, blast over-pressure and inertia, with the most common cases being caused by a sudden blow or jolt to the head, leading to the acceleration of the head at a high rate, most commonly seen within contact sports (Stemper & Pintar, 2014). The energy imparted from said blow causes the head to accelerate, resulting in brain motion to also commence as the brain is inside the skull surrounded by a thin layer of cerebrospinal fluid (CSF), and has the ability to move. CSF allows the brain to move, without coming in contact with the inside of the skull due to its cushioning material properties. When a significant head acceleration occurs due to a blow however, the CSF is unable to stop the brain from striking the skull (Shaw, 2002). Due to the visco-elastic nature of brain tissue, striking the skull in an aggressive manner results in deformation, distortion and compression of said tissue, potentially leading to injury (Shaw, 2002; Shuck & Advani, 1972).

It is hypothesised that linear and rotational motion are the two major mechanisms during an impact that lead to head injuries such as concussions, with several studies conducted over the years to better understand which has a higher effect on the brain. Pure linear acceleration is believed to create pressure gradients within the brain whereas pure rotational acceleration rotates the skull relative to the brain, resulting in diffuse shearing of brain tissue (Gennarelli et al., 1982; Unterharnscheidt, 1971). This was supported by the work of L. Zhang, Yang, and King (2004), who found a correlation between resultant translational acceleration and intracranial pressure, as well as a correlation between resultant angular acceleration and shear stress at the brain-stem, with R^2 value of 0.77 and 0.78 observed, respectively.

Researchers have conducted tests with primates and dogs, in order to better understand the mechanics behind head injuries and concussion. The work conducted by E. Gurdjian and Lissner (1944); E. Gurdjian and Webster (1943); JE and HR (1955) delivered blows to the heads of anaesthetized dogs via a hammer, falling weight or a striker to understand deflections and pressures of the head. E. Gurdjian and Lissner (1944) utilised two pressure plugs screwed into the dogs' skulls, with bonded resistance wire strain gauges to help detect intracranial pressure changes and deflections upon conducting the blows. The experiment concluded that the deformation of the skull and head accelerations caused changes in intracranial pressures, leading to traumatic intracranial damage. Additionally, E. S. Gurdjian, Lissner, and Patrick (1963) reported the importance of linear acceleration as the primary cause of concussion, with angular motion being of little significance in many of the conducted experiments. This conclusion was supported by other researchers, such as by Hodgson et al. (1969) who conducted a neuropathological experiment with monkeys. The experiments consisted of a 1 kg striker travelling at 38-58 km/h, inflicting blows to the back of the monkeys' heads, where the researchers established that although rotational motion existed, linear acceleration is the most important mechanism behind head injuries. This was further backed up by Ono, Kikuchi, Nakamura, Kobayashi, and Nakamura (1980) who conducted impacts on 63 monkeys using a head restraint mask and an unrestrained head setup, drawing to a similar conclusion to Hodgson et al. (1969) stating that concussion in monkeys showed no correlation with rotational acceleration of the head.

Other researchers have, however, suggested that rotational acceleration has a larger effect on the brain leading to concussion (Post, Hoshizaki, Gilchrist, & Cusimano, 2017). Gennarelli, Thibault, and Ommaya (1972) used controlled sagittal plane head motion on 25 monkeys, splitting the monkeys into groups of 12 and 13, with one group subjected to pure translation and the other to head rotations. They found that all monkeys subjected to rotational motion were concussed, whereas none were concussed that were subjected to linear motion. Additionally, Löwenhielm (1975) utilised a viscoelastic mathematical model to simulate the deformation of the brain, establishing that angular acceleration resulted in gliding contusion from strain in cerebral vessels. They also found that the surface of the brain can be perceived to be unaffected while deeper lying tissues within the brain are heavily affected and therefore results in extensive brain related injury. Furthermore, J. Zhang, Yoganandan, Pintar, and Gennarelli (2006) used a Simulated Injury Monitor (SIMon) human finite element head model with lateral head impact experimental data, to better understand whether linear or rotational acceleration plays more of a role in inducing excessive brain strain from blunt head impacts. These authors analysed maximum principle strain in different regions of the head model for three cases of acceleration loading; rotational, translational and translational + rotational, and found that translational acceleration produced minimal principal strain as it was established to be only 10% of the principal strain calculated for rotational motion. This led to the same conclusion as Löwenhielm (1975) and Gennarelli et al. (1972), suggesting rotational accelerations are more

prone than linear accelerations to inducing brain injuries and concussion. Furthermore, other research has determined, angular acceleration, angular velocity and impact duration as key factors within injury severity, with a strong correlation between rotational kinematics and injury severity also reported (Gennarelli, Pintar, & Yoganandan, 2003; Gennarelli et al., 1982, 1987). Despite the continuous debate among researchers regarding which has a bigger impact on brain injuries, the importance of linear and rotational motion in understanding concussion is evident, highlighting the need to understand head kinematics during impacts.

1.2 Concussion Effects

The severity of concussive injuries in contact sports comes from the degree of short term and long term effects on a player post concussion(s). Short term symptoms post-concussion include dizziness, a difficulty in concentrating, fatigue, headache, among others, which can last anywhere in the range of a few days to a few months (De Kruijk et al., 2002; Evans, 1994; Ryan & Warden, 2003). Lundin, de Boussard, Edman, and Borg (2006) conducted a study with 122 patients with mTBI, and assessed their symptoms after 1, 7, 14 days and 3 months to establish trends within short term effects post trauma. As well as highlighting the several different symptoms of mTBI, Lundin et al. (2006) were able to observe that the majority of the symptoms gradually declined from day 1 to 3 months, with the number of patients reporting one or more symptom of mTBI dropping from 86% to 49% from day 1 to 3 months. These authors observed, however, that some symptoms worsened over the 3 month period, specifically poor memory, irritability and restlessness.

Long term effects sustained from concussions, however, have been hypothesised to be much more serious and damaging. It is believed that multiple concussions or subconcussive impacts over time can result in severe long term brain damage, which is usually common within athletes competing in contact sports as they can be subjected to multiple mTBI events during the course of their playing careers (Guskiewicz, Marshall, et al., 2007). Long term effects include mild cognitive impairment (Jellinger, 2004), depression (Guskiewicz, Marshall, et al., 2007) and Chronic Traumatic Encephalopathy (CTE) (McKee et al., 2009), highlighting the potential severity of the injury to players health after they have retired. The research conducted by Guskiewicz et al. (2005) highlights the potential long term effects of multiple concussions. The researchers provided 2,552 retired professional football players that had previously been concussed, with a series of questionnaires, hoping to better understand a relationship between concussion and late life cognitive impairment. They established, that although there wasn't an evident correlation between Alzheimer's disease and recurrent concussions, Alzheimer's disease was prominent earlier in retired football players in comparison to the general population.

Other research has been conducted, focusing on the understanding of CTE. CTE is described as a progressive brain disease that is distinctive from other neurodegenerative diseases such as Alzheimer's, with symptoms including memory disturbances, parkinsonism, speech and gait abnormalities and behavioural and personality changes(McKee et al., 2009; Stemper & Pintar, 2014). The disease, also known previously as *punch drunk*, is frequently seen within boxers due to the multi-head impact nature of the sport (McKee et al., 2009). However, recent cases have been reported within other contact sports such as soccer, wrestling and American football where five different middle aged ex-players dying suddenly with verified CTE at autopsy (Cajigal, 2007; Geddes, Vowles, Nicoll, & Revesz, 1999; McKee et al., 2009).

Due to the nature of these long term effects, potentially leading to fatalities, research has focused drastically in trying to understand the causes and in detecting concussion in order to prevent repeated concussions and hence severe injuries. Some techniques utilised currently include the use of eye tracking (Samadani et al., 2015), nanoparticle-enabled protein biomarker implementation for saliva based detection (Caswell, Cortes, Mitchell, Liotta, & Petricoin, 2015), MEG low frequency source imaging detection (Huang et al., 2012) and wearable sensors (Bartsch, Samorezov, Benzel, Miele, & Brett, 2014).

1.3 Concussion Causes and Statistics

Statistics showing the rate of concussion within the workplace, military and contact sports, coupled with the severity of symptoms post trauma, highlights the ever-growing cause for concern. Workplace mTBI is an underestimated area of concussion, with 1 in 4 reported concussions occurring there (Kristman et al., 2010). The study conducted by Colantonio et al. (2010) provided an overview of occupational traumatic brain injury in Ontario, in which they found that the highest rate of mTBI was seen within the transport and storage sectors (82/100,000). These authors also found the injuries were predominantly caused by people getting struck by or against objects, as well as falls. Within soldiers in the military, where concussions can occur from blast over-pressure or impact with an object during a blast event (Hoge et al., 2008; Stemper & Pintar, 2014), Wilk et al. (2010) reported that 14.9% returning from combat deployment met concussion assessment criteria. Additionally, a survey conducted by Hoge et al. (2008) found that 4.9% of soldiers suffered a loss of consciousness post injury, with a further 10.3% reporting no loss of consciousness but their mental status altered.

1.3.1 Contact Sports

Contact sports are played and enjoyed by millions across the world in different forms, at youth, amateur and professional levels, and provide the participants the ability to compete physically, mentally and technically against their peers in a team environment. Injuries are the resultant of the physical nature of most contact sports, with the most severe being concussion, which makes up 5-20% of all injuries within contact sports (Kerr et al., 2008). Sport-related concussions occur due to the impact nature of most contact sports resulting in the head to decelerate, whether in player-to-player contact, which makes up 75% of concussions, or player contact with a surface (McCrory et al., 2017; Meehan, d'Hemecourt, & Dawn Comstock, 2010; Stemper & Pintar, 2014; VanItallie, 2019).

Several studies have been conducted to understand the rate of concussion within different contact sports at high school and collegiate level (ages 14-21). The rate of concussions, defined as number of concussions per 1,000 athletic exposures (AE), was found to be the highest in American football in some studies, with values between 0.37-0.61 reported (Gessel, Fields, Collins, Dick, & Comstock, 2007; Hootman, Dick, & Agel, 2007; Lincoln et al., 2011; Prien, Grafe, Rössler, Junge, & Verhagen, 2018; Schulz et al., 2004). Furthermore, Hootman et al. (2007) reported concussion rates of 0.28, 0.26 and 0.25 for soccer, lacrosse and wrestling, highlighting that concussion is a multi sport issue. More recently, Prien et al. (2018) and Pfister, Pfister, Hagel, Ghali, and Ronksley (2016) conducted systematic reviews to analyse the number of concussive events seen within different sports at both professional and youth level. Their results showed concussion rates within rugby to be the highest, with 3 and 4.3 concussions recorded per 1,000 AE within professional and youth level rugby match play, respectively, with men's soccer providing the lowest concussion rate. The nature of both American football and Rugby results in frequent contact opportunities, whether that is tackling or getting tackled, which in turn results in a higher chance of concussion for the players taking part within these sports. Additionally, Hootman et al. (2007) established that concussion rates were higher during match play than in training, which was supported by Prien et al. (2018). Meehan et al. (2010) established a similar trend during the analysis of high school concussions during an academic year, where they found that 78.5% of reported concussions were during competitive play. This is hypothesised to be due to training sessions often being less intense and competitive than matches, with drills setup to avoid injuries of any kind.

1.4 Project Overview

The project presented within this thesis focuses on the concussion problem, specifically in non helmeted sports. Non-helmeted contact sports are popular worldwide in a number of different forms, one of the most popular being Rugby Union which has a registered player base of 9.6 million and a fan base of 405 million (Rugby, 2019). Rugby Union is a physical contact sport played by two teams of 15 players, using an oval-shaped ball which cannot be thrown forwards. The aim of the sport is to score more points than the opposition, which can be achieved by touching the ball to the ground past the opponent's goal line, or kicking it through the opponent's goalposts. To stop the opponent from scoring, players who do not have possession of the ball use their arms and shoulders in an attempt to tackle, and hence stop the ball carrier from advancing. These tackles can result in forceful collisions, as the tackler and player in possession are running in opposite directions and with great momentum, which leads to high risk of injuries and more importantly concussions (Fuller, Taylor, & Raftery, 2015). Head-to-head impacts are common, which results in head injuries accounting for 17% of injuries within Rugby Union with 13-17% of rugby players sustaining a concussion during a season (Marshall & Spencer, 2001; Tucker, 2017). Wearable sensors are utilised to potentially help solve the problem and are a major focus within this project. Specifically, the feasibility of wearable sensors that are being utilised to detect concussions is examined, as well as determining methods to contextualise impact data from said sensors to better understand concussions.

1.4.1 Wearable Sensors Background

Understanding head kinematics during and after an impact, predominantly the linear and rotational acceleration of the head, is being extensively researched within contact sports as they are hypothesised to be the two major mechanisms during impacts that lead to concussion, as previously discussed. Different methods have been proposed and used in the past to understand the kinematics of the human head during and after an impact, with video footage being the only source of data available at the early stages of this area of research. McIntosh, McCrory, and Comerford (2000) used video recordings of impacts to estimate the head impact velocity in two dimensions, allowing the estimation of the energy transfer to the head from an impact. This method, however, proved not to be an accurate way of understanding head kinematics due to the impact velocity being approximated as well as a number of parameters required for the calculations being estimated.

Wearable sensors housing accelerometers and gyroscopes were therefore utilised to provide head kinematic data in order to establish head impact trends within contact sports. For helmeted sports, head mounted sensors placed inside helmets are utilised in order to quantify impacts. Researchers predominantly used the Head Impact Telemetry (HIT) system that incorporated 6 single-axis linear accelerometers embedded in the padding of the helmet for

studies in helmeted sports (Brolinson et al., 2006; Funk, Rowson, Daniel, & Duma, 2012; Guskiewicz, Mihalik, et al., 2007; Schnebel, Gwin, Anderson, & Gatlin, 2007). The accuracy of the kinematic data obtained from HIT and helmet-mounted sensors was rigorously studied, with researchers establishing errors above 15% in resultant peak linear accelerations, which could be due to the lack of helmet/head coupling resulting in false recordings or over inflated magnitudes (Allison et al., 2014; Jadischke, Viano, Dau, King, & McCarthy, 2013; O'Connor, Rowson, Duma, & Broglio, 2017).

For non-helmeted sports, a skin-mounted wireless sensor known as a 'skin patch' was developed and placed behind the ear of the player (Tiernan, Byrne, & O'Sullivan, 2019). This device records key data when an impact occurs, such as linear acceleration and rotational velocity components of the head. This technology was used extensively by D. King, Hume, Gissane, and Clark (2017), Hecimovich, King, Dempsey, Gittins, and Murphy (2018) and Willmott et al. (2018). The aforementioned studies sampled data from within different levels of Australian Rules Football, from youth to sub-elite, as well as amateur Rugby League. D. King et al. (2017) conducted a study to quantify head impacts within amateur Rugby League players over the course of two seasons. Their study monitored kinematic data obtained from skin-mounted sensors worn by 42 players in order to observe the trends of impact magnitudes within rugby league. These researchers found that linear acceleration characteristics for head impacts were similar to those reported in helmeted sports and the majority of the 52 head impacts per players observed fell into the mild category of impact severity. Other studies have, however, questioned the accuracy of kinematic data obtained from skin-mounted wireless sensors, as measurement errors for peak resultant accelerations were found to be as high as 50% due to skin dynamics and lack of skull coupling (O'Connor et al., 2017; L. C. Wu et al., 2016).

Further technological advancements saw the development of instrumented mouthguards, which house a sensor strip that can capture kinematic data via a gyroscope and linear accelerometer (Bartsch et al., 2014; Camarillo, Shull, Mattson, Shultz, & Garza, 2013; Hernandez et al., 2015; Kuo et al., 2018; Rich et al., 2019). Instrumented mouthguards are currently being used more widely in research as they allow more accurate data recording in comparison to the skin-mounted sensors. L. C. Wu et al. (2016) found that mouthguards showed tighter skull couplings than skin-mounted sensors, providing more accurate kinematic results. This technology has predominantly been used for research purposes within helmeted sports such as American football (Bartsch et al., 2014; Camarillo et al., 2013; Hernandez et al., 2015; Kuo et al., 2018), with a small number of research projects focusing on non-helmeted sports (D. King, Hume, Clark, Tarvirdizade, & Hind, 2024; Tooby et al., 2023; Waldron, Jones, Melotti, Brown, & Kilduff, 2021). D. King, Hume, Brughelli, and Gissane (2015) conducted one of the first studies with an instrumented mouthguard, quantifying head impacts within amateur Rugby Union players. In this study, 38 male amateur players were given custom fitted instrumented

mouthguards sampling at 1000 Hz to wear for the duration of the 19 game season. Their study found the mean number of head impacts sustained by a player over the season was 95 with a mean magnitude of 22g and evaluated that forwards as a position group recorded more impacts than backs. They concluded the acceleration magnitudes and number of head impacts recorded within their research exceeded most other sports. More recently, Kieffer, Vaillancourt, Brolinson, and Rowson (2020) conducted a study to quantify concussive and sub concussive impacts in non helmeted athletes, analysing head impacts as well as body impacts. Their research found a median peak linear acceleration of 15.2g and 13.6g frrom head and body impacts respectively.

1.4.2 Aims and Objectives

The work presented in this thesis is multi-faceted, including the collection and analysis of head impact data from a new instrumented mouthguard in order to understand the feasibility of said mouthguard in contact sports. The feasibility study was conducted by working closely with a professional rugby team during matches and training, to help understand if the wearable device was fit for purpose. Additionally, the research focuses on developing a method to contextualise impact data collected by wearable sensors. More specifically, a key focus of the work presented was to determine impact location on the head from instrumented mouthguard data by exploring to usability of rigid body dynamics and machine learning algorithms, helping future research understand and quantify concussive events.

Rigid body dynamics is the study of how solid objects move and interact when forces are applied to them, assuming the objects don't change shape. It simplifies the analysis by treating the object as a single, unchanging entity, making it easier to calculate how fast or how far it might go as well as how it might spin. This concept is widely used in fields like engineering, robotics, and animation to accurately simulate the movement of objects in the real world and is a concept that could be utilised with the human head and neck to help determine impact locations (Hibbeler, 2004; Meriam, Kraige, & Bolton, 2020). Machine learning algorithms however, are advanced tools that help computers learn from data and make decisions or predictions without being explicitly programmed. Instead of giving the computer specific instructions for every possible scenario, it is provided with a large amount of data, letting it find patterns and relationships on its own accord. With regards to impact location, machine learning algorithms could establish patterns between different types of impacts occurring at different locations (Domingos, 2015; Russell & Norvig, 2016).

A major research push has been made to establish the magnitudes of head impacts, which when coupled up with the work presented in this research regarding impact location, would aid the clinical understanding of concussion within contact sport.

The overall objectives of this research are:

1. To evaluate the performance of a new instrumented mouthguard, working with professional rugby players. The work presented in Chapter 2 is conducted to tackle this aim of the thesis.
2. To explore the potential of using rigid body dynamics and/or machine learning algorithms to understand impact location on the head from the obtained six kinematic signals, highlighted in the work presented in Chapters 3 and 4.

Chapter 2

Force Impact Technologies Mouthguard Feasibility

2.1 Introduction

Instrumented mouthguard usage within contact sport is ever growing, with sports teams medical personnel as well as researchers gaining more interest regarding the technology. One of the new instrumented mouthguards utilised in industry currently is produced by Force Impact Technologies (FIT), who aim to solve the problem of athletes prematurely returning to play when there is a high probability of head-injury or concussion. FIT's device houses technology to determine kinematic response of the head during impacts, which can assist the sports coaching and medical teams to better protect their athletes. The following chapter looks into conducting a feasibility study for the FIT mouthguard as no previous feasibility study evaluating the device has been published. Feasibility and validation studies are conducted within industry to establish if the devices are fit for purpose, with some of the leading instrumented mouthguards taking part in studies previously.

Different mouthguards have been developed, with extensive efforts being placed into the validation of kinematic data obtained from these devices. Camarillo et al. (2013) developed a novel instrumented mouthguard and evaluated the accuracy of the kinematic data by impacting a custom anthropomorphic test device (ATD) head-form. The head-form was fitted with a helmet on top of a Hybrid III ATD neck, and was struck from various sites using a linear impactor. The study established a high correlation between the mouthguard and ATD with regards to peak linear acceleration, peak angular acceleration and peak angular velocity measurements, validating the ability of instrumented mouthguards as a research tool to obtain reliable kinematic data. Additionally, Bartsch et al. (2014) developed a mouthguard to be able to quantify single head impact events, which was tested and validated by three distinct methods: (i) bench top component drop tests comparing the results of the mouthguard with a reference accelerometer; (ii) linear impactor tests and (iii) in vivo tests within Boxing and American Football.

While every mouthguard developed gets the kinematic output validated by companies internally, they do require external feasibility testing to ensure the strengths and weaknesses of each device is understood by the potential users. Liu et al. (2020) conducted a feasibility study comparing five of the most commonly used instrumented mouthguards utilising a pneumatic impactor to impact a head form in order to evaluate the kinematic output of all the mouthguards. The study established all the tested mouthguards provided a high level of accuracy regarding peak angular acceleration and velocity. More recently, B. Jones et al. (2022) lead a more in depth research project understanding the feasibility of four leading mouthguards. Unlike the study by Liu et al. (2020), this study focused on kinematic output of the devices as well as other factors to ensure the devices were fit for purpose. These include the feel and comfort of the devices and the usability of the hardware and software systems that come alongside the mouthguards.

The study conducted to evaluate the FIT mouthguard within this chapter utilises principles from the validation study presented by B. Jones et al. (2022), with an emphasis on: i) Comfort and fit, ii) On field data validation and iii) Usability of the system.

2.2 Methodology

This three-phase study evaluated FITs instrumented mouthguard in order to establish if the device is fit for purpose within professional non helmeted contact sport. Phase I evaluated the comfort and fit of the mouthguard from a players perspective. Phase II analysed the on field data in order to validate the kinematic output from the device as well as determining if the device is able to determine true impacts. Phase III evaluated the usability of the entire FIT system, whether the preparation and management of the device is easy and feasible for a professional team staff members to conduct alongside their existing roles.

In order to achieve the aim of testing the instrumented mouthguard, it was integral to find the appropriate partners to effectively facilitate the desired testing environment. FIT provided sensor strips that create their instrumented mouthguards for the feasibility study. Additionally, It was established that a professional Rugby Union team would be important as the aim was to understand feasibility of the instrumented mouthguard within professional non-contact sport. The team selected for this research was Edinburgh Rugby, a professional club rugby team operating under the Scottish Rugby Union (SRU) umbrella. The team competes in the Pro 14, a professional league housing teams from Scotland, Wales, Ireland and South Africa. The agreed partnership with Edinburgh Rugby allowed the research team to work with their first team players and allowed access to matches and training sessions. Furthermore, to mould the mouthguards for the professional team required the use of a dental practice to help embed the

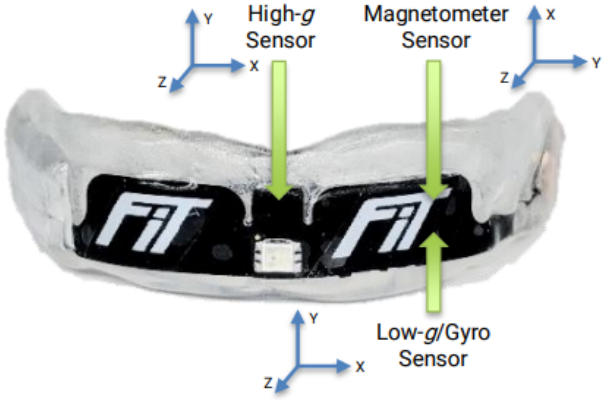

Figure 2.1: FIT sensor strip with positioning of all sensors highlighted (image courtesy of FIT (2014), unpublished).

FIT sensors. The dental practice selected for the project was the Edinburgh based practice, SmilePlus Dental. SmilePlus Dental were the official partner for the SRU, therefore already created custom fitted mouthguards for all players that play for the Scotland national team and Edinburgh Rugby, making them the logical choice for the study.

2.2.1 FITs Sensor Strip Design and Components

The sensor strip provided by FIT housed technology that provides kinematic data from impacts. The strip consisted of High- and Low-g sensors, a gyroscope and a magnetometer, the locations of which on the sensor strip are highlighted in Figure 2.1. The High-g sensor (ST H3LIS331DL) provided the desired linear accelerations ($\pm$ 200g @ 1000 Hz) with the gyroscope (ST LSM6DS3H) providing rotational velocity ($\pm$2000 dps @ 1666 Hz) data required for this research. Additionally, the sensor strip contained a Light-Emitting Diode (LED) situated below the High-g accelerometer, a charging coil, data memory storage and a Bluetooth connectivity interface.

The LED is a feature added by FIT inorder to notify impact severity. Figure 2.2 provides a schematic snapshot of impact data, with different threshold levels, that when breached illuminate the LED light in the colour of the threshold. This provides the user and coaching team with immediate impact severity notification. Although configurable, default impact threshold levels are set at 30g, 60g and 100g for low (LOW), medium (MED) and high (HIGH) impact levels, respectively. Additionally, Once the LOW impact threshold has been exceeded, an impact snapshot is taken and stored, allowing the user to analyse the impact kinematics post session. The default impact snapshot duration was set at 40 ms, with it capturing 15 ms of data pre-impact and 25 ms of data post-impact. The impact data snapshot window is also configurable, however making it larger would require more memory space to store each impact.

Figure 2.2: Example impact snapshot and threshold levels that illuminate LED within the sensor strip (image courtesy of FIT (2014), unpublished).

2.2.2 Phase I - Comfort and Fit of Mouthguard

The eight male players from Edinburgh rugby were supplied with a instrumented mouthguard that had been developed specifically for them. All created mouthguards followed the same process. Initially, the players' mouth-moulds were created, like the one seen in Figure 2.3a, in order to custom fit each mouthguard to the shape of each players upper jaw. Mouth-moulds were created by dispensing alginate, a thick liquid material, in a U-shaped tray which was placed on the upper set of teeth. This was held in place for a few moments to allow the liquid to harden around the teeth and become solid rubber, at which point the tray was removed. Dental stone was then poured into the created dental rubber impression, which upon solidifying created the stone mouth-moulds.

(a) **(b)**

Figure 2.3: (a) Example mouth-mould for a player and (b) mouth-mould with instrumented mouthguard moulded around it.

Thermoforming was used to create the mouthguards by using a thermoformer, as shown in Figure 2.4a, and the stone mouth-moulds. Prior to placing the mouth-mould within the thermoformer, all the moulds were sanded to ensure that they had smooth surfaces, as highlighted in Figure 2.4b. This was conducted to aid the thermoforming process, as rough surfaces within the stone mould could damage the mouthguard material, or cause air pockets during thermoforming.

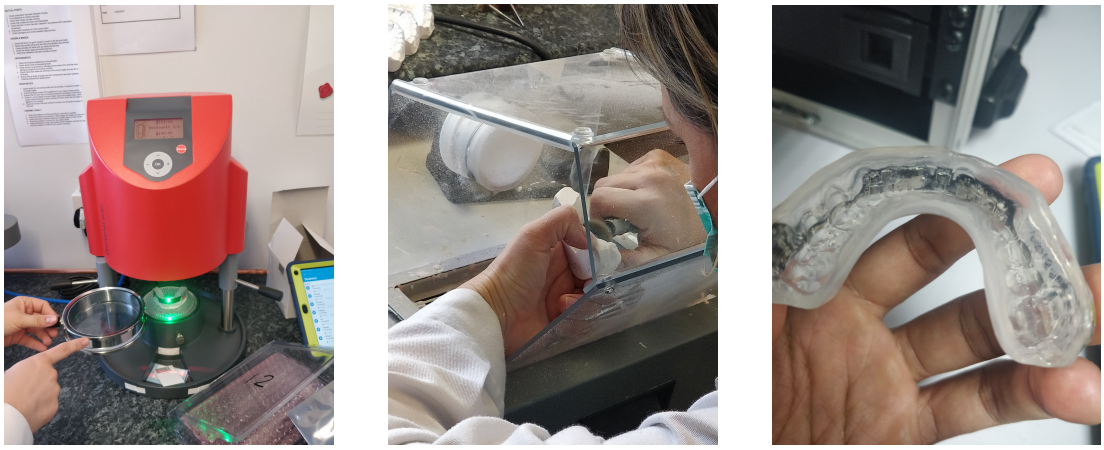

(a) (b) (c)

Figure 2.4: Mouthguard creation process: (a) sanding of the mould, (b) thermoforming equipment and procedure, and (c) finished mouthguard.

Drufosoft, a thermoforming blank made up of ethyl vinyl acetate, is commonly used to create mouthguards and was utilised for the instrumented mouthguards created for this research. Initially, a clear 3 mm layer of Drufosoft was placed within the thermoformer, with the stone mouth-moulds placed on the tray below. The thermoformer heated the material which was then levered down around the mouth-mould and held in place for 1-2 minutes, ensuring the material took the shape of the mouth-mould before cooling. Upon completion of the cooling process, the thermoformed part was taken out of the thermoformer and trimmed using a heat knife, removing excess material and concluding the creation of the inner layer of the instrumented mouthguard.At this stage in the process, the sensor strip was added by placing it on the outside of the freshly created mouthguard layer. The sensor strips provided by FIT, were trimmed at the edges to ensure that the hardware was not longer than the mouthguard. The final stage of the process involved another 3 mm layer of Drufosoft being placed in the thermoformer, with the mouth-mould housing the inner layer and the sensor strip, placed on the tray below. The thermoforming process, as described above, was repeated, embedding the sensor strip within two 3 mm layers of material, completing the instrumented mouthguard creation process, as shown in Figure 2.4c. The addition of the sensor strip increased the thickness of the mouthguard by between 1 and 1.5 mm from the usual mouthguards the players were used to wearing. The players were invited to try the mouthguards and provide feedback on the fit and comfort, and whether they noticed any differences from their existing non-instrumented mouthguards.

2.2.3 Phase II - On field Validity

On field validity of the mouthguard looked into the data output from the device while being worn by players during matches and training sessions. Five of the eight players were eligible to take part within this phase of the study and were selected to ensure most of the rugby position groups were involved, with three forwards, at least one on each line, and two backs chosen. Forwards are a position group within rugby consisting of heavier athletes who usually wear numbers 1 to 8, whereas backs tend to be quicker, lighter, more agile players who wear numbers 9 to 15. The players selected for this phase of the study were ones that were likely to be part of the first team squad and hence get game time.

The main focus of the on-field validity phase was to examine the kinematic output, ensure the instrumented mouthguard's storage is sufficient to hold data for the duration of a game or training session, and determine how accurately the mouthguard identifies and stores positive impacts rather than false positives. Threshold values are implemented within instrumented mouthguard systems to collect positive impacts above a certain impact acceleration value. The FIT system was initially set to trigger only at 30g, as it was built to alert customers to extreme impacts. For research purposes, however, the impact threshold was set at $14g$, which is the lowest value the FIT system is configurable to, although still higher than the 5 to $10g$ configuration utilized in existing research (D. King, Hume, Gissane, Brughelli, & Clark, 2016; Tooby et al., 2024). This phase was conducted over a five-month period during games and one training session per week.

2.2.4 Phase III - Usability of system

Understanding the usability of the system is essential as sports scientists/ physiotherapists require and efficient and straightforward method to collect and analyse data. FIT supplied an overview of their recommended data collection process, as seen in the Flowchart in Figure 2.5, which house two key phases, pre-session and post-session.

The pre session phase consisted of cleaning, charging and supplying of the mouthguards. Cleaning mouthguards was trivial as it required a rinse of the mouthguard under warm water however FIT recommended that once a week the mouthguards were cleaned using proper oral appliance cleaner such as a denture cleaner. The charging process included placing the mouthguard within a FIT supplied charging tray (see Figure 2.6a). Each mouthguard housed a coil, which allowed for conductive charging of the instrumented mouthguards to take place with an estimated 90 minute charging time required for a them to be fully charged. During the charging process, a red flashing LED on the instrumented mouthguard notified if the mouthguard was charging, which turned to green when the charging process had completed, as shown in Figure 2.6a. The methodology to activate mouthguards included using the FIT

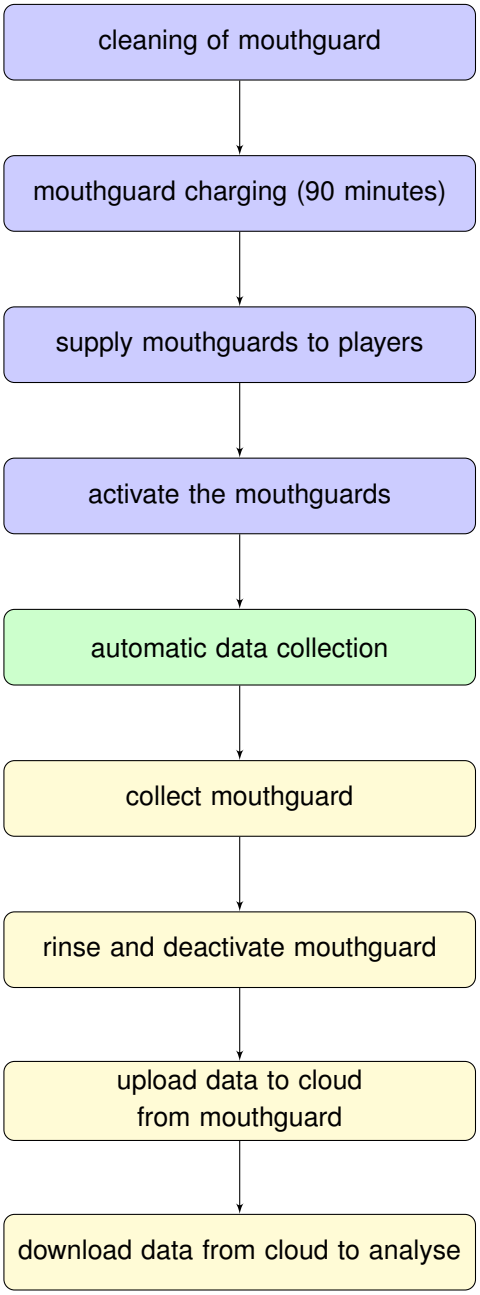

Figure 2.5: Flow-chart outlining the data collection process. Blue blocks showcase the steps within the Pre-Session pahse, green block the step within the During-Session phase and yellow blocks the steps within Post-Session phase.

app on a tablet device via Bluetooth. The FIT app, shown in Figure 2.7, allowed the researcher to select a mouthguard and then activate the device remotely, allowing it to be ready to collect impact data. The mouthguard LED provided confirmation of the activated state by flashing green twice upon activation.

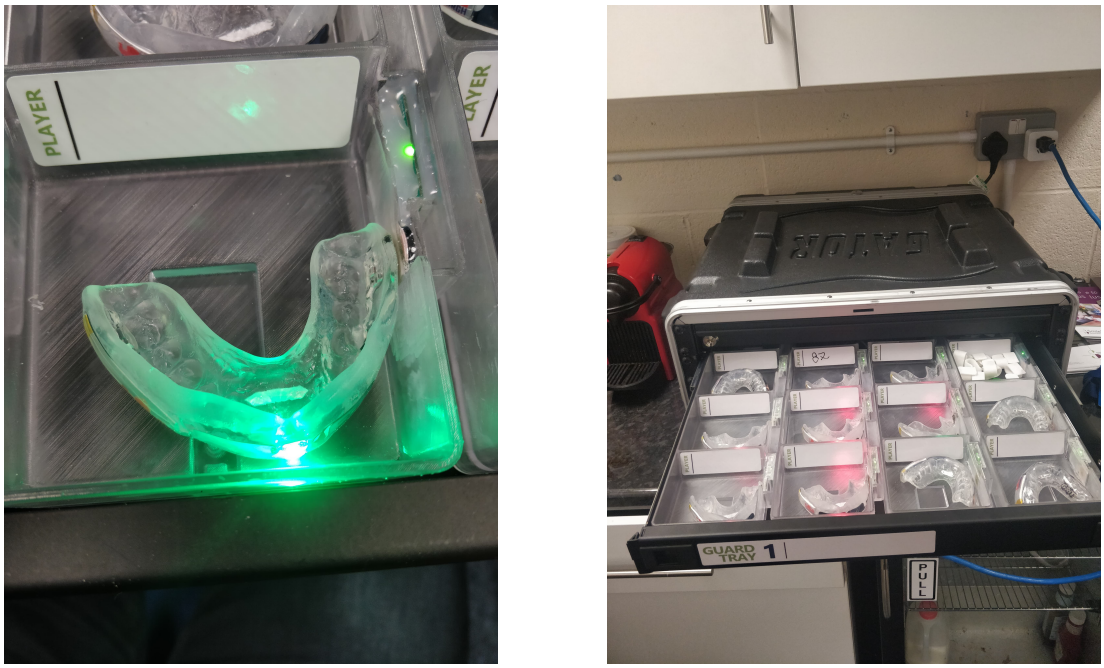

(a) **(b)**

Figure 2.6: Mouthguard charging station: (a) highlighting the charging coil with the LED at green to show fully charged state and (b) the multi-tray charging box supplied by FIT to allow for simultaneous charge of all mouthguards.

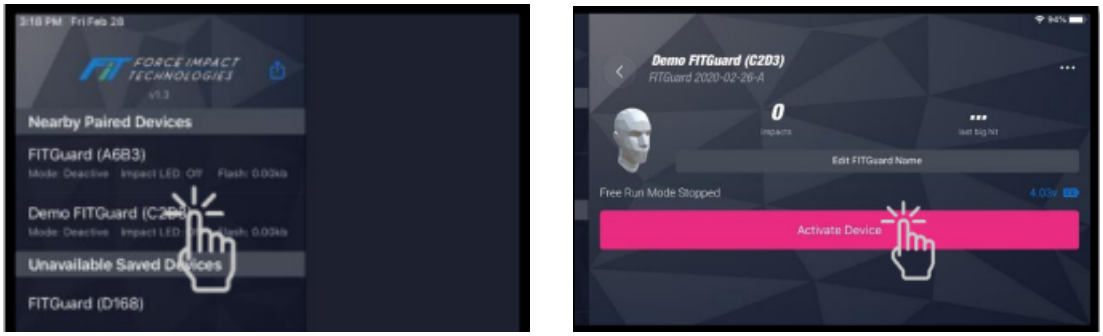

(a) **(b)**

Figure 2.7: Example screenshots of the FIT app: (a) showcasing the interface where mouthguards can be selected and (b) highlighting where the specific mouthguards are activated. Courtesy of a unpublished document from FIT (2014).

The post session phase consisted of collecting and deactivating the mouthguards, followed by uploading impact data from the mouthguard to the cloud and downloading impact data to analyse. Deactivation methodology followed the same process as activation procedure described. Once the mouthguard connected to the FIT app, impact data was automatically transferred, which was then readily accessible on the tablet, as seen in Figure 2.8, while being simultaneously uploaded to the FIT cloud. Downloading data from the FIT cloud required accessing the cloud and simply downloading the data zip file for specific impacts, as seen in Figure 2.9. The downloaded zip file housed the following data: (i) gyroscope data, (ii) High-g accelerometer data, (iii) sensor settings, (iv) Low-g accelerometer data and (v) magnetometer data.

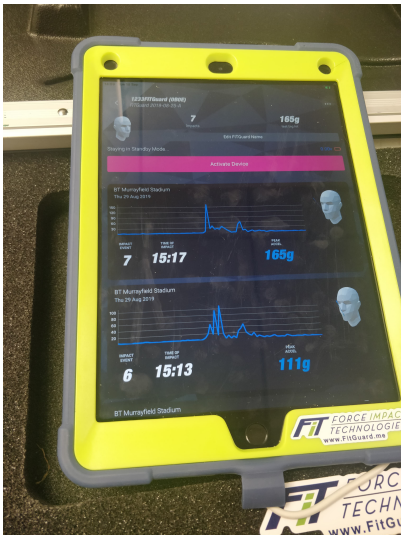

Figure 2.8: Tablet device connected with instrumented mouthguard, showcasing the downloaded impacts from a session

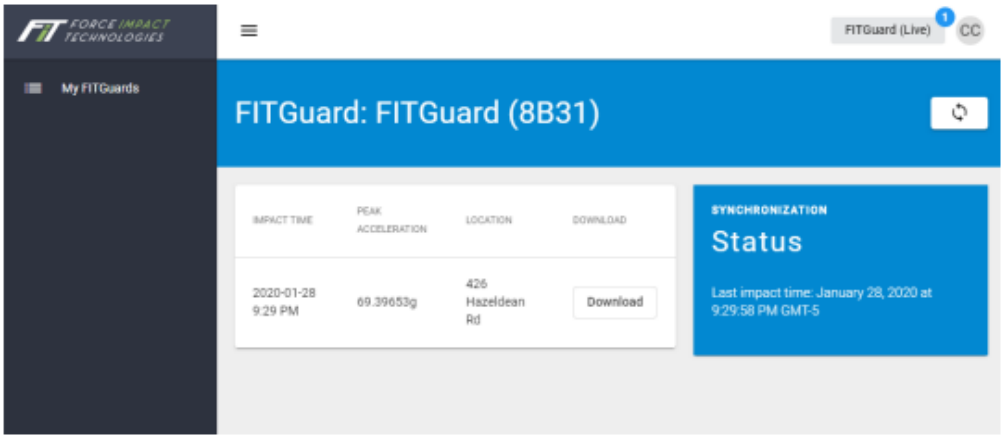

Figure 2.9: FIT cloud highlighting the kinematic data uploads from instrumented mouthguards

To test the feasibility of the methodology supplied by FIT, the researcher and a sports science practitioner with no prior experience of using instrumented mouthguard systems followed the processes over the five month period, evaluating if it was fit for purpose for a fast paced professional team, logging any issues that were faced. Additionally, members of the Edinburgh Rugby medical and coaching staff were asked if the data collection process hindered the ability to conduct pre-session tasks with players.

2.3 Results and Discussion

2.3.1 Phase I - Comfort and Fit of Mouthguard

Eight professional rugby players were invited to provide feedback on the fit and and comfort of mouthguards custom fitted to them.Despite the instrumented mouthguard being only 1 to 1.5 mm thicker, three of the players noticed the added thickness around the sides, where the battery pack within the sensor strip was located, reporting they wouldn't wear them in their current format. Additionally, two of the players reported the mouthguards were acceptable, however their comfort levels were compromised due to them preferring shorter mouthguards that covered only up until their first molar. This was challenging to achieve with the sensor strip provided by FIT due the length of the hardware.

The bulkiness experienced by the players with FIT mouthguards is consistent with accounts reported in existing research.B. Jones et al. (2022) found that approximately 80 % of players expressed bulkiness of the Biocore-FRI and ORB mouthguards, with 37% and 33% reported for HitIQ and Prevent respectably. In this study, 37.5% of participants reported the mouthguard as bulky, and 62.5% were dissatisfied with its feel. Consequently, the FIT mouthguard's performance in this phase ranks in the middle among commonly used instrumented mouthguards in the industry.

2.3.2 Phase II - On-field Validity

On field validity of the device was tested by analysing the kinematic output from some of the recorded impacts with a key focus on analysing the linear acceleration, rotational velocity, and identifying and storing positive impact data.

Linear Acceleration

Kinematic data obtained from a few of the impacts sustained were video verified to understand if the data replicated video footage. The linear acceleration as seen in Figure 2.11, highlights the magnitudes for each component faced for two separate impacts that were extensively analysed. The nature of both impacts were similar, with the player being the ball carrier and running into contact. For the first impact, Figure 2.11a, the player carried the ball from the back of a maul straight into contact. A maul is a tactical ploy in Rugby, where the ball is held off the ground with minimum one player from each team, excluding the ball carrier, are bound together while on their feet, as highlighted in Figure 2.10b. The player lowered his head as he went into contact, making it difficult for the opposing player to tackle and slow him down, which resulted in a head-to-head collision between the tackler and the player. The impact location was verified by video at the top of the head, which was expected as player B went into contact with the coronal plane of the head parallel to the ground. The Peak Linear Acceleration (PLA) of 100g in the negative Oy direction reflects the extreme nature of the impact sustained. For the second impact, a player carried the ball from a ruck into contact. A ruck is a phase of play in Rugby where the ball is on the ground, with minimum one player from each team is in contact over the ball, as seen in Figure 2.10a. Upon picking the ball up from the ruck and running towards the opposition, the player was met with two opposition players waiting to tackle him. The ball carrying player, lowered the head again, however one of the tacklers had got lower than the ball carrier at the point of contact, resulting in the impact location of the collision being more frontal than the impact described above. This is reflected within the kinematic data obtained from the instrumented mouthguard, Figure 2.11b, which highlights the negative Oz direction as the major impact axis with a PLA of 77g.

(a) **(b)**

Figure 2.10: Example Rugby tactical plays: (a) showcasing a Ruck (Rees, 2020) and (b) a Maul (Mahon, 2014).

Where the linear acceleration data may seem correct regarding the direction of impact being translated within the linear acceleration components, the validity of the magnitudes seen within some of the impacts can be questioned. The impact shown in Figure 2.11 showcases an impact duration of less than 5 milliseconds and a PLA of 100g, which is extremely rare, as

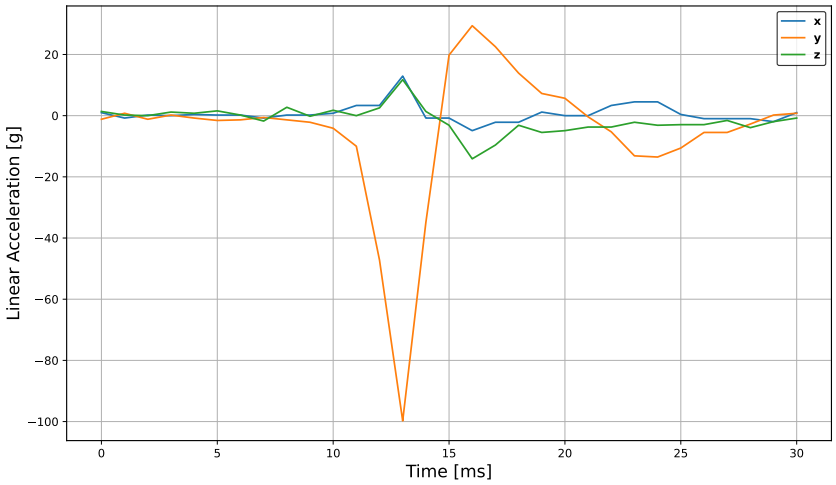

(a)

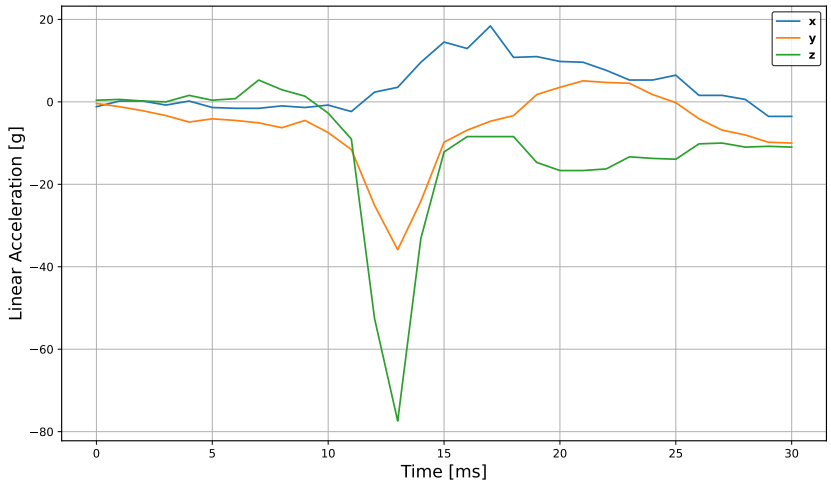

(b)

Figure 2.11: Linear acceleration from impacts sustained by a player: (a) running into a tackle from a maul peel off and (b) running into a tackle from a ruck pick up.

reported in many existing research studies (Roe et al., 2024; Tooby et al., 2024). Roe et al. (2024) established the probability of head impact magnitudes for multiple event types, reporting a ball carry probability of above 65g as being less than 0.5%. However, in this study, impacts like the one shown in Figure 2.11 were recorded multiple times. In the majority of cases, from observation, the impacts didn't seem big, and players were able to continue playing as normal post-impact, suggesting the magnitude of the impact may not have been as high as reported by the FIT mouthguard. This raises some concerns regarding the validity

of the linear acceleration output from the FIT mouthguard device during live games and may require more validation studies before deeming the kinematic linear output as accurate. Additionally, the sampling rate of the linear accelerometer being 1000Hz is also of concern. Where sampling rates of 1000Hz were utilised in older instrumented mouthguards (Liu et al., 2020), more recent research studies have established high sampling rates are beneficial in order to establish more accurate linear acceleration readings. One of the leaders within this field, Prevent Biometrics samples data as 3200Hz, which would be the recommended setting for FIT going forward to further improve their product (B. Jones et al., 2022).

Rotational Velocity

Upon collecting and analysing rotational velocity kinematic data, it was noticeable that the gyroscope was providing false signals. The signals were observed to flat line, as well as starting at the upper or lower extremities. Within the pre-impact state it was expected that components of rotational velocity are around 0 as the mouthguard should be in a stable state, therefore the signals starting at the extremities highlighted the false nature of the gyroscope data. This can be seen in the example provided in Figure 2.12, where its evident that the Oy and Oz components are showing extreme rotational velocity in the pre-impact phase prior to the impact occurring at approximately 50 ms. Additionally, all three components flat line at periods between 55 and 100 ms. While comparing this data to ones stated within literature (C. M. Jones et al., 2023), it is even more evident the rotational velocity components are not fit for purpose. Upon analysis of multiple impacts, it is hypothesised that the gyroscopes supplied within the sensor strip may have had a hardware issue or the issue may lie within the software resulting in chunks of gyroscope data going missing.

Furthermore, the sampling rate configured for the gyroscope may require alteration. The FIT gyroscope operates at 1600 Hz, which differs from the sampling rate of the accelerometers. This discrepancy presents challenges in matching timestamps of impact data between the two sensors, an issue not seen with competitors in the field. ORB, Biocore-FRI, and Prevent Biometrics instrumented mouthguards have sensors that operate at the same frequency, while HitIQ has configured their sensors so that they are multiples of each other (B. Jones et al., 2022). It is recommended that FIT follow other competitors in this field by raising the sampling frequency, as discussed earlier, and maintaining consistency between the two sensors.

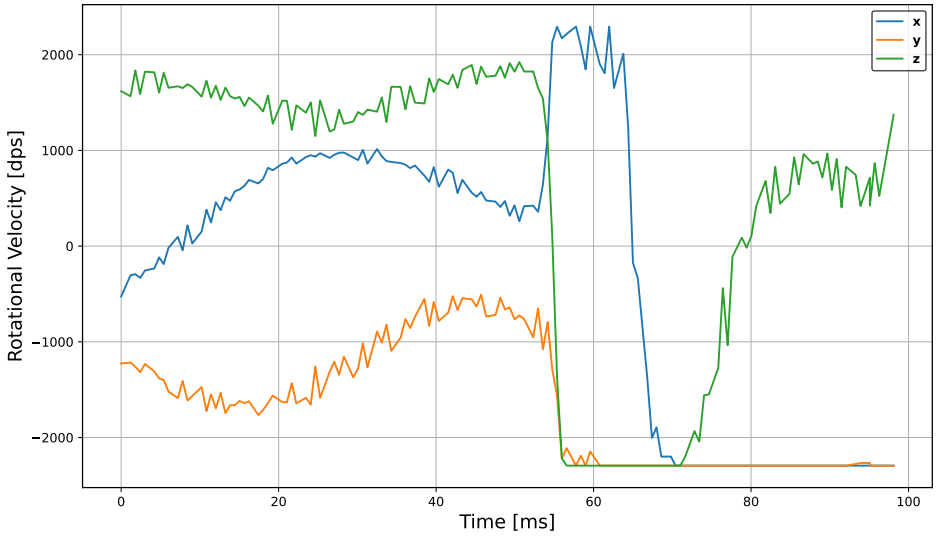

Figure 2.12: Example of gyroscope data obtained from the instrumented mouthguard during the pilot study. Kinematic response for components not starting at 0, and flat lining during the course of the impact.

Identifying and Storing Positive Impacts

Setting the impact threshold to $14g$ uncovered an issue regarding data storage. The mouthguard's data storage capacity was not able to handle the number of true and false impacts recorded by the sensors, resulting in the memory reaching capacity before the sessions concluded. The data storage capacity within the mouthguard is 140 by default but can rise to 350 by reducing impact snapshot times, which seems sufficient for a 2-hour session. However, it was evident that the FIT mouthguard lacks the technology that some other leading mouthguards have to activate only when in use, ensuring most impacts captured are positive collisions. This means FIT's device captures and stores many false impacts, such as players dropping the devices, putting them down, biting the device, or placing it in their sock while they walk or warm up.

A distribution analysis was conducted to better understand the problem and help determine a recommended threshold that would be low enough to capture as many impacts as possible, yet high enough to filter out enough false impacts so that the memory would be sufficient for an entire session. The distribution analysis, as seen in Figure 2.13, was conducted on impact data collected from one of the mouthguards with a $14g$ threshold setting. The memory reached full capacity of 140 recorded impacts within 20 minutes of the mouthguard being active, all of which were false impacts, as the player was still taking part in warm-up drills when the mouthguard reached full capacity. With the number of impacts that could be stored increasing to 350 with ease, and the session duration being up to 2 hours, a threshold value

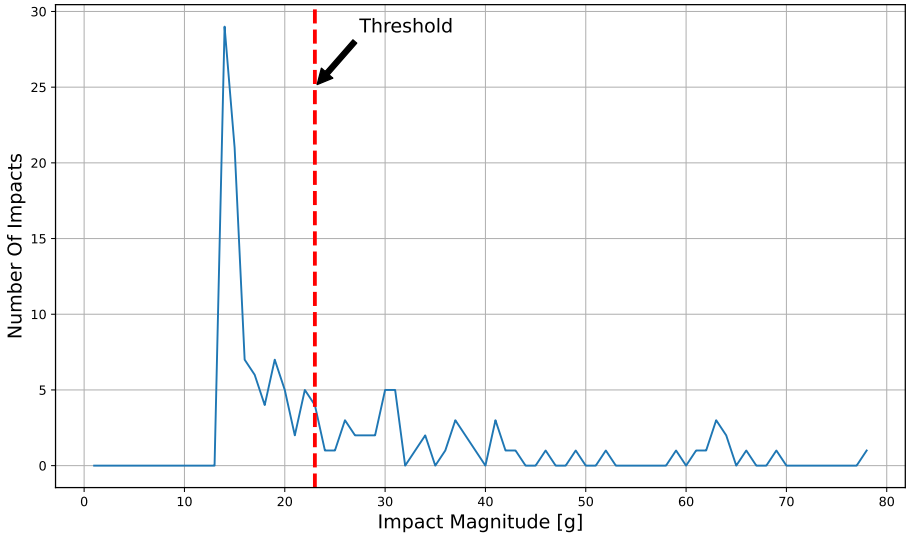

Figure 2.13: Distribution analysis for impacts recorded by the instrumented mouthguard with the recommended threshold value highlighted.

was chosen based on what would allow for 55 impacts to be stored in the 20-minute time frame. The recommended threshold value setting for the FIT mouthguard should be $23g$, which would still fail to record the majority of impacts seen in rugby, as recent research has reported impact magnitudes in rugby to be predominantly below $10g$ (Tooby, Weaving, Al-Dawoud, & Tierney, 2022).

In its current format, the FIT mouthguard is unable to fully capture positive impact data and requires a system to eliminate false impacts from being recorded. Additionally, with the research work presented by Tooby et al. (2022), it is essential that for research purposes, the mouthguard needs to be configurable as low as $5g$, which in turn will require a better data storage system within the sensor strip in order to make it fit for purpose.

2.3.3 Phase III - Usability of system

The usability of the system was predominantly very promising, particularly in terms of how straightforward the process laid out by FIT was for the researcher and the sport scientist with no prior experience of the system. However, one prominent issue during the study was related to the charging of the device. The charging tray's wireless charging coil needed to be close to the mouthguard coil to commence charging. It was established that during charging, the coil in the mouthguard heated the plastic around it, softening the material. Upon cooling, this caused the mouthguard to stick to the charger, resulting in damaged mouthguards when force was required to detach them from the charging tray wall. This issue is critical for FIT to solve,

as supplying damaged mouthguards with exposed electronics to players is very dangerous. To avoid this issue, it was found that adding a slight air gap between the mouthguard and the charger wall reduced the risk of sticking during charging and is thus the recommended practice with the current FIT mouthguard.

Furthermore, the sport science practitioner appreciated that the charging tray housed the entire team's devices in one place. However, they reported that the charging time of 90 minutes might be too long for away games, as the team sometimes arrives with only an hour before warm-up routines commence. Additionally, the practitioner found activating and deactivating mouthguards individually very time-consuming and requested a method to activate or deactivate the devices together, something that FIT may need to consider going forward to save time.

Despite these few issues, the overall usability of the system is promising. With some improvements, it has the potential to be fit for purpose in the fast-paced professional rugby world. This was highlighted by the players and coaching staff, who, upon being interviewed, conveyed that they appreciated that the process didn't hinder their pre-session and post-session routines.

2.4 Conclusion

In conclusion, Force Impact Technologies released a new instrumented mouthguard designed to identify head kinematics during and post-impacts in contact sports. As the mouthguard had only been tested in a lab, a feasibility and validity study was conducted to determine if it was fit for professional sports. Three major aspects were tested during the study with Edinburgh Rugby: the comfort and fit of the device, the on-field kinematic data, and the usability of the system.

The device by FIT performed between the best and worst-performing mouthguards in the industry regarding comfort and fit, with 62.5% of players dissatisfied with the feel of the device. Furthermore, the on-field kinematics testing raised multiple concerns. The reported linear acceleration components matched well with video footage; however, the magnitudes reported for some impacts were deemed potentially inaccurate. Additionally, gyroscope data was flawed throughout the study, showing signs of missing data resulting in flatlining, and pre-impact values for components were at the upper or lower extremities. Other issues included the frequency of the gyroscope/linear accelerometer being too low, the lack of a system to determine when the mouthguard was in use to minimize false impacts, and the inability to configure the mouthguard threshold to 5g to capture the majority of head impacts. However, the mouthguard performed well in the usability study, with Edinburgh Rugby's staff and players commending how the process didn't hinder them. A sports science practitioner with no prior knowledge of instrumented mouthguards was able to conduct the data collection process with ease.

Nevertheless, FIT's mouthguard requires a lot more development before it can be deemed fit for professional contact sports. The on-field kinematics require more rigorous testing to improve the quality of the output, as well as implementing the changes recommended in this study. In its current form, it is highly advised not to utilise the FIT mouthguard for any research or injury detection purposes.

Chapter 3

Impact Location Using Rigid Body Dynamics

3.1 Introduction

The second phase of this research focused on establishing impact locations in order to better understand concussive head impacts and aid the battle against mTBI. The main aim of the research presented in this and following chapter is to propose and develop methods, algorithms and numerical tools that will allow researchers to analyse kinematic data from instrumented mouthguards. The data collected from the sensors is in the form of tri-axial acceleration and rotational velocity components. The proposed methods in the following chapters determine the location and orientation of the impact on the head, based in this data.

3.1.1 Impact Location Research

Little research has been conducted to propose a robust method to determine the impact locations from sensor data. In most reported cases, peak linear acceleration components are used to approximate the direction of impact and hence an impact location region (back, side, front) (Crisco et al., 2010). Video footage is often utilised alongside to verify impact location regions, as PLA component based regions have shown inaccuracies (Kuo et al., 2018). In most cases, however, this is an extremely costly and time consuming process. Crisco, Chu, and Greenwald (2004) developed an algorithm that allows the location of an impact to be calculated. This algorithm is based on data collected from several single axis non-orthogonal accelerometers and was found to be an effective method for helmeted sports, where multiple accelerometers can be placed within the helmet. For instrumented mouthguards with a tri-axial linear accelerometer and gyroscope, Bartsch et al. (2014) and Kuo et al. (2018) proposed methodologies to approximate the location of the impact. Bartsch et al. utilised rigid body dynamics with assumptions, to simplify the problem in order to determine an approximated impact location whereas Kuo et al. utilised integrated linear and rotational position values to determine an impact region. The methodology proposed by Kuo et al. however, was only able to classify 37% of impacts to the correct impact region, highlighting the need for a methodology

to improve upon the accuracy of impact location classification. The following section describes a proposed method, which builds on the work published by Bartsch et al. (2014), utilising rigid body dynamics and a multi-degree of freedom (MDOF) lumped-mass system replicating the head and neck, to determine the orientation, magnitude and location of an impact force from instrumented mouthguard data.

Unlike the approaches by Bartsch et al. and Kuo et al., the method described within this chapter aims to determine the impact location rather than a region of the head where the impact occurs. The accuracy of the impact location determined by the proposed method is established by an author-defined metric as described in the following sections. It is hypothesised, with the extensive data collection push expected in the recent future, knowing where on the head the impact occurs will be very useful, as different areas of the same region (back/side/front) could be more or less susceptible to concussions, making the methodology presented in this chapter extremely useful in the battle against mTBI (Sohail, Teixeira-Dias, & Merriman, 2022). [1]

3.1.2 Finite Elements and Synthetic Kinematic Data

Due to the inability to collect live data, and lack of access to a testing laboratory, the ability to obtain impact kinematic data sets was severely impacted to the point of not being possible. Therefore, the creation of synthetic data sets was essential to allow for the impact location methodologies described in this chapter and Chapter 4, to be tested and validated. Numerical simulation and in particular the finite element method (FEM) was chosen as an efficient approach to generate synthetic kinematic data sets that closely replicate live impacts sustained by players taking part in non-helmeted contact sports, namely Rugby Union.

Finite Element (FE) models have been used extensively in a number of areas as a cost-effective alternative and complement to extensive and costly experimental campaigns. Examples of fields in which FEM has been utilised include bridge analysis (Duan, Wang, & Yau, 2019; Rahmzadeh, Alam, & Tremblay, 2018; Song, 2019), structure analysis (Benaroya & Rehak, 1988; Chen & Liu, 2018; Marques, Silva, & Pereira, 2020) among others. FE head models have also been extensively used within existing research in an attempt to model head impacts to better understand head injuries. Originally, 2D plane strain FE head models were developed representing multiple cross-sections of the head. The initial models developed consisted of just a skull (Hardy & Marcal, 1973), which was later developed to include a fluid-filled brain (Shugar, 1975). The 2D approach, however, was in general found to produce unreasonable results, leading to the development of 3D models which consisted of simple geometries, such as spherical or ellipsoidal solids, to represent the skull and brain (Chan, 1974; Kenner & Goldsmith, 1972; Khalil & Hubbard, 1977). However, more recently head

1. The work presented within this chapter has been published in Proceedings of the Institution of Mechanical Engineers, Part P: Journal of Sports Engineering and Technology.(Sohail et al., 2022)

models have been created with detailed facial functions, representing the the human head in a more accurate manner, and therefore are being extensively utilised within current head and brain injury research. One of the most well known head models being utilised is the the Wayne State University Brain Injury Model (WSUBIM) which is a detailed model representing the features of a 50th percentile male (A. I. King, Yang, Zhang, Hardy, & Viano, 2003; L. Zhang et al., 2001). The model, validated by using cadaveric test data, is utilised to predict the stress/strain level within key regions of the head, induced by direct and indirect impacts. Other similar models currently being utilised include the University of Louis Pasteur FE head model (H.-S. Kang, Willinger, Diaw, & Chinn, 1997), Kungliga Tekniska Hogskolan FE head model (Kleiven & Hardy, 2002), Simulated Injury Monitor FE head model (Takhounts et al., 2003) and the University College Dublin Brain Trauma Model (Horgan & Gilchrist, 2003) amongst others.

For the purpose of the research presented within this thesis, only head kinematics that replicated data obtained from instrumented mouthguards were required, therefore FE models designed to understand internal brain injuries, like the ones described above, were deemed to be too complex. This research therefore hypothesised that a Hybrid III Dummy FE head model would be more fit for purpose, as it would provide the desired kinematic data signals in a more efficient manner, as less computing time would be required to simulate impacts. This hypothesis was evident when comparing models, for instance a Hybrid III Dummy FE head model consists of 67400 nodes where as the WSUBIM consists of over 280000 nodes (S. Kang & Xiao, 2008; A. I. King et al., 2003; L. Zhang et al., 2001).

The Hybrid III Dummy anthropomorphic test device (H3ATD) was originally created to better understand head and neck dynamic response during automotive impacts (Mertz & Patrick, 1971; Mertz Jr & Patrick, 1968). Several studies have been conducted within the automotive industry over the years with the Hybrid III Dummy ATD, in an attempt to enhance the safety within vehicles (Duma, Crandall, Rudd, & Kent, 2003; Friedman, Hutchinson, & Mihora, 2007). More recently, however, it has been utilised within athletic injury analysis research (Rousseau & Hoshizaki, 2009). The H3ATD has been at the forefront of research within contact sports and has been utilised in a number of methods to help aid research. Pellman, Viano, Tucker, Casson, and Waeckerle (2003) utilised a H3ATD to reconstruct head impacts to help evaluate concussion biomechanics. The researchers were able to determine the speed, location and direction of numerous significant impacts by analysing multiple impact videos. This data was then utilised with a helmeted H3ATD, recreating the impacts seen within games in the laboratory and allowing the researchers the ability to understand head kinematic trends within contact sport. Additionally, wearable sensor validation has been conducted by utilising H3ATD as shown by research partners FIT, who utilised a H3ATD with the biokinetics impactor to validate their instrumented mouthguard (FIT, 2014; Siegmund, Guskiewicz, Marshall, DeMarco, & Bonin, 2014a). Furthermore, Beckwith, Greenwald, and Chu (2012) established a correlation

between impact kinematics determined from wearable sensors and impact kinematics determined using a H3ATD under conditions that replicated on field impacts. The ability of the H3ATD to replicate on field impacts also resulted in them being utilised for helmet design testing, ensuring the helmets are fit for purpose within helmeted contact sport (Bartsch, Benzel, Miele, & Prakash, 2012; Pellman et al., 2006). The capabilities of the H3ATD to perform well in existing head impact kinematics research highlights that a validated FE model of the H3ATD would be fit for purpose within this research. Options of a validated Hybrid III Dummy head model include the ones developed by Humanetics (D. A. Jones et al., 2019), Livermore Software Technology Corps (LSTC) (S. Kang & Xiao, 2008) and Biomedical Engineering Society (Giudice et al., 2019).

3.2 Impact Magnitude and Location Algorithm Methodology

The method proposed to determine the magnitude, orientation, and location of an impact based on mouthguard linear acceleration and rotational velocity components is based on rigid body dynamics. In layman's terms, the methodology assumes the head is a rigid body that has moved due to an external force (impact). Therefore, the methodology seeks to find the turning force, also known as the moment, that the impact caused to the head. Moments can be found in two ways: by using rotational velocity or by establishing how much force is applied and how far from the rotation point it was applied. In this study, we are interested in finding the distance from the rotation point where the impact force was applied to achieve the same moment as the one determined from reported rotational velocity values. The main steps in the Impact Magnitude and Location Algorithm (IMLA) developed in this work can be summarised as follows:

1. Calculation of the components of the moment, from Euler's equations. Implementation of the theory is available in Listing A.1
2. Estimation of the magnitude of the impact force with a multi-degree of freedom (MDOF) system. This is achieved with modal analysis to establish the mechanical response of the system in three linear directions. Implementation of the theory is available in Listing A.2
3. Moment matching between Euler's and torque equations to determine the location of the impact.Implementation of the theory is available in Listing A.3

3.2.1 Impact moment calculation

The moment experienced by the head because of the impact is first calculated using Euler's equations, where the Cartesian components of the moment vector $\boldsymbol{T}$ are

$$\boldsymbol{T} = \left\{ \begin{array}{c} T_x \\ T_y \\ T_z \end{array} \right\} = \left\{ \begin{array}{c} I_{xx}\dot{\omega}_x - (I_{yy} - I_{zz})\omega_y\omega_z \\ I_{yy}\dot{\omega}_y - (I_{zz} - I_{xx})\omega_z\omega_x \\ I_{zz}\dot{\omega}_z - (I_{xx} - I_{yy})\omega_x\omega_y \end{array} \right\} \tag{3.1}$$

$$\left\{ \begin{array}{c} I_{xx} \\ I_{yy} \\ I_{zz} \end{array} \right\} = \left\{ \begin{array}{c} I_{xcog} + m(y^2 + z^2) \\ I_{ycog} + m(x^2 + z^2) \\ I_{zcog} + m(x^2 + z^2) \end{array} \right\} \tag{3.2}$$

where I_{ij}, with $i, j = x, y, z$ as shown in Figure 3.1, are the moments of inertia about the head/C1 vertebrae joint established by using the parallel axis theorem (Eq 3.2), $\dot{\omega}_i$ are the rotational acceleration components of the head and ω_i are the rotational velocity components of the head. The head/C1 vertebrae joint is used as the main rotation point to replicate realistic head motion. The parallel axis theorem is used to determine the second moment of area about the rotation point from the center of gravity. The theory presented requires a consistent timestamp within the peak linear acceleration phase to be used when obtaining kinematic data. This ensures that the methodology performs effectively and yields the best results.

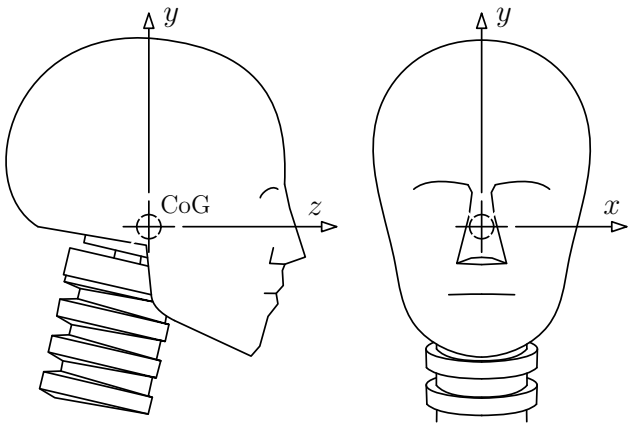

Figure 3.1: Global axis orientations. xy plane representing the coronal plane, yz plane representing the sagittal plane and xz plane representing the transverse plane.

3.2.2 Impact force magnitude

To establish a force in three dimensions, a multi-degree of freedom (MDOF) mass-spring system was utilised. An MDOF mass-spring system is a way to model and analyse the behavior of systems with multiple masses connected by springs, where each mass can move independently. This type of model helps us understand how complex structures or mechanical systems respond to forces. A simple mass-spring system would move a certain distance over time if an external force was applied. An example of a mass-spring system can be found in Rao (2011), where an external force is applied to a two-mass system with the goal of finding the displacement of the masses. These principles are utilised in this research; however, the goal here is to determine the force value required to move the mass (head) by an amount (distance) that corresponds to the kinematic output observed from an instrumented mouthguard. In this research, a three-dimensional mass-spring MDOF system is used to estimate the magnitude and direction of the impact force on the head. This 4-mass system as visualised in Figure 3.2, replicates the human head and neck with the springs replicating the stiffness of the intervertebral joints. m_1 is the mass of the head and m_2, m_3 and m_4 are the masses of the cervical vertebrae pairs C1-C2, C3-C4 and C5-C6, respectively, as defined by Luo and Goldsmith Luo and Goldsmith (1991). The equations of motion of the system are

$$\mathbf{M}\ddot{\boldsymbol{x}} + \mathbf{K}\boldsymbol{x} = \boldsymbol{F} \tag{3.3}$$

where $\mathbf{M}$ and $\mathbf{K}$ are the inertia and stiffness matrices, and $\boldsymbol{F}$ is the vector of external forces acting on the system. Damping is not considered in the MDOF model as in the short impact times that are characteristic of head impacts in sports, there are no significant energy dissipation mechanisms and the response of the system is dominated by stiffness.

The stiffnesses of the intervertebral disks were determined by Luo and Goldsmith (1991) using stiffness data previously reported by Deng and Goldsmith and Panjabi (Deng & Goldsmith, 1987; Panjabi, 1973), considering that the stiffness of each individual joint is proportional to the cross-sectional area of the corresponding disk. These authors calculated a stiffness matrix for the C2/C3 joint and a proportionality factor for the remaining ones, allowing stiffness matrix calculations for any intervertebral joint. The (6$\times$ 6) C2/C3 joint stiffness matrix supplied by Luo and Goldsmith (1991) incorporates all six degrees of freedom, three linear and three rotational. As the MDOF system is a linear three-dimensional system, the stiffness matrix provided by Luo and Goldsmith Luo and Goldsmith (1991) becomes

$$\mathbf{k} = \begin{bmatrix} 122 & 0 & 0 \\ 0 & 390 & 25 \\ 0 & 25 & 140 \end{bmatrix} \times 10^3 \quad [\mathrm{N/m}] \tag{3.4}$$

The individual springs $\mathbf{k}_i = \alpha\mathbf{k}$ $(i = 1,\ldots,4)$ are the (3×3) stiffness matrices for each joint, which replicate the head/C1, C2/C3, C4/C5 and C6/C7 intervertebral joints as highlighted in Figure 3.2, and α is the proportionality factor. The global stiffness matrix $\mathbf{K}$ then becomes

$$\mathbf{K} = \begin{bmatrix} \mathbf{k}_1 & -\mathbf{k}_1 & 0 & 0 \\ -\mathbf{k}_1 & \mathbf{k}_1+\mathbf{k}_2 & -\mathbf{k}_2 & 0 \\ 0 & -\mathbf{k}_2 & \mathbf{k}_2+\mathbf{k}_3 & -\mathbf{k}_3 \\ 0 & 0 & -\mathbf{k}_3 & \mathbf{k}_3+\mathbf{k}_4 \end{bmatrix} \tag{3.5}$$

The global inertia matrix compiles the four individual mass matrices as

$$\mathbf{M} = \begin{bmatrix} \mathbf{m}_1 & 0 & 0 & 0 \\ 0 & \mathbf{m}_2 & 0 & 0 \\ 0 & 0 & \mathbf{m}_3 & 0 \\ 0 & 0 & 0 & \mathbf{m}_4 \end{bmatrix} \quad \text{with} \quad \mathbf{m}_i = \begin{bmatrix} m_i & 0 & 0 \\ 0 & m_i & 0 \\ 0 & 0 & m_i \end{bmatrix} \tag{3.6}$$

The inertia of the individual vertebrae couples and head are also taken from Lou and Goldsmith Luo and Goldsmith (1991).

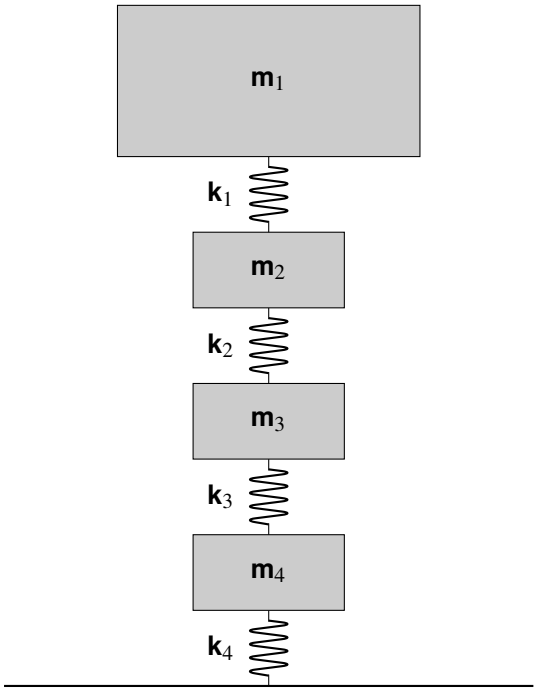

Figure 3.2: Simplified schematics of MDOF system replicating the human head and neck.

The external force vector is

$$\boldsymbol{F} = \begin{Bmatrix} F_x \\ F_y \\ F_z \\ 0 \\ \vdots \\ 0 \end{Bmatrix} \tag{3.7}$$

where F_x, F_y and F_z are the unknowns of the problem. Note that, as the proposed method models head impacts, the only non-zero external forces are associated with $\mathbf{m}_1$.

Modal analysis is used to calculate the natural frequencies and mode shapes of the MDOF system, which are in turn used to determine the mechanical response of the system when a force is applied Rao (2011). The equation of motion, Equation 3.3, can then be re-written as

$$\left(\mathbf{K}\mathbf{M}^{-1}\right) \boldsymbol{X}_i = w_i^2 \boldsymbol{X}_i \tag{3.8}$$

where $\boldsymbol{X}_i$ ($i = 1, \ldots, 12$) are the system's mode shape vectors and w_i are the corresponding natural frequencies. The modal force vector $\boldsymbol{Q}$ can then be calculated as

$$\boldsymbol{Q} = \mathbf{X}^{\mathsf{T}} \boldsymbol{F} \tag{3.9}$$

where $\mathbf{X}$ is the modal shape matrix. In order to determine the unknowns within the modal force, the following displacement equation is solved

$$\boldsymbol{x} = \mathbf{X}\boldsymbol{q} \tag{3.10}$$

where $\boldsymbol{x}$ is the displacement vector of the system, consisting linear displacements for all four masses, and $\boldsymbol{q}$ is the vector with components

$$q_i = \frac{1}{w_i}\left[\frac{Q_i}{w_i}\left(1 - \cos(w_i t)\right)\right] \tag{3.11}$$

The linear acceleration components of the head are obtained directly from mouthguard data and then converted to linear acceleration components at the center of gravity (CoG) of the head with

$$\boldsymbol{a}_{CoG} = \boldsymbol{a}_M + \dot{\boldsymbol{\omega}} \times \boldsymbol{d} + \boldsymbol{\omega} \times \boldsymbol{\omega} \times \boldsymbol{d} \tag{3.12}$$

where $\boldsymbol{a}_M$ are the linear accelerations recorded at the mouthguard, $\dot{\boldsymbol{\omega}}$ and $\boldsymbol{\omega}$ are the rotational accelerations and velocities of the head, and $\boldsymbol{d}$ is the position vector of the CoG relative to the mouthguard. This value is challenging to calculate accurately and will vary from player to player, therefore for the purpose of the IMLA, $\boldsymbol{d}$ can be estimated by determining the distance from a selected node in the mouth of a generic FE Head model to the corresponding center of gravity.

Integrating $\boldsymbol{a}_{CoG}$ twice allows the displacement of the head to be calculated. By solving Equation 3.10, the unknown components of the impact force within the modal force, Equation 3.9, and unknown displacement components for the system can be calculated.

3.2.3 Impact location

The impact location was determined by matching the moments calculated with Equation 3.1 and the torque equation

$$\boldsymbol{T}_t = \boldsymbol{r} \times \boldsymbol{F}_t \tag{3.13}$$

where $\boldsymbol{r}$ is the position vector from the axis of rotation, as defined in the impact moment calculation section, to a point on the surface of the skull. $\boldsymbol{F}_t$ is the force vector consisting of force components on the head as calculated from the MDOF system in Equation 3.10.

For the purpose of the IMLA, the moments are calculated for coordinates on the surface of a head using Equation 3.13. Coordinates can be established by utilising nodes from a generic FE model or from MRI scans for specific players. Obtaining an MRI scan for every player within a team could be very impractical therefore the authors proposed that a generic FE model approach to be used with the IMLA. A three-stage process is implemented to determine the location of the impact. Initially, the algorithm matches moment signs, eliminating nodes with position vector $\boldsymbol{r}$ that produce differentiating $\boldsymbol{T}_t$ component signs to $\boldsymbol{T}$. Secondly, moments values $\boldsymbol{T}_t$ not within $\boldsymbol{T} \pm 100\%$ are eliminated leaving a small cluster of nodes, providing an estimation of the impact location. For this algorithm a broad tolerance of $\pm 100\%$ established good results in identifying approximated impact regions. Finally, the tolerance is incrementally reduced until only one node is remaining, which is determined as the best fitting node (BFN) and the location of the impact on the surface of the head. For the purpose of this research, where coordinates were established from a Hybrid III Dummy model, The impact location calculated by the algorithm is deemed accurate and fit for purpose if the BFN matches the node of the impact center or is a neighboring node to the impact center. This equates to the calculated BFN being within 14 mm of the impact center, due to the mesh size of the Hybrid III Dummy head..

3.3 Validation

The IMLA was validated by obtaining head impact kinematic data by two methods. The primary method used a head-neck finite element Hybrid III Dummy model simulating impacts on the dummy head. Impact simulations were conducted on different locations of the head, and the kinematic responses were used to validate the IMLA. Additionally, kinematic impact data was obtained in a laboratory test from an instrumented mouthguard similar to the one described in Section 2.2.2. The two methods complement each other to provide a validation of the proposed IMLA. The Hybrid III finite element (FE) simulations allow control over key impact parameters such as head dimensions, minimising errors when testing the IMLA. Additionally, the simulations provide a method to test the developed algorithm against impacts of varying magnitudes and locations with ease. The observations from the experimental test ensure the IMLA is accurate and can be used to determine the location of impacts while using instrumented mouthguards.

3.3.1 Numerical modelling

A validated Hybrid III Dummy FE model developed by LSTC was utilised on LS-DYNA to generate the synthetic kinematic data sets required (Kan, Marzougui, & Bedewi, 2003; S. Kang & Xiao, 2008; Mohan et al., 2010). As head impacts were required for the purpose of this research, a subset of the full Hybrid III model consisting of the Head and neck was utilised, as seen in Figure 3.3. The model consisted of 23 parts, 50,478 elements, 67,400 nodes and was created with hexahedral constant stress solid finite elements. The number of nodes, elements and mass of each part listed in Table 3.1. Additionally, the list of parts within the model with their corresponding material card and properties are listed in Table 3.2. Furthermore, the density values of the Neck Adaptor, Lower Neck Force Gauge - Upper Part and Lower Neck Force Gauge - Lower Part were selected to be 2.50×10^{5} as highlighted in Table 3.2, as it resulted in the 17 kg mass of the upper torso to be accurately modelled (Foster, Kortge, & Wolanin, 1977).

Five numerical simulations were conducted using the validated LS-DYNA Hybrid III Dummy head/neck model, with a custom made impactor (Kan et al., 2003; S. Kang & Xiao, 2008).

A cylindrical impactor with a diameter of 100 mm and a thickness of 40 mm was created with hexahedral solid reduced integration constant stress finite elements as seen in Figure 3.4. The impactor consisted of 4,329 nodes, 3,680 elements with 12,987 degrees of freedom and a mesh size of 3.5 mm with Table 3.3 listing the impactor mass, density and initial conditions (velocity components) for each test.

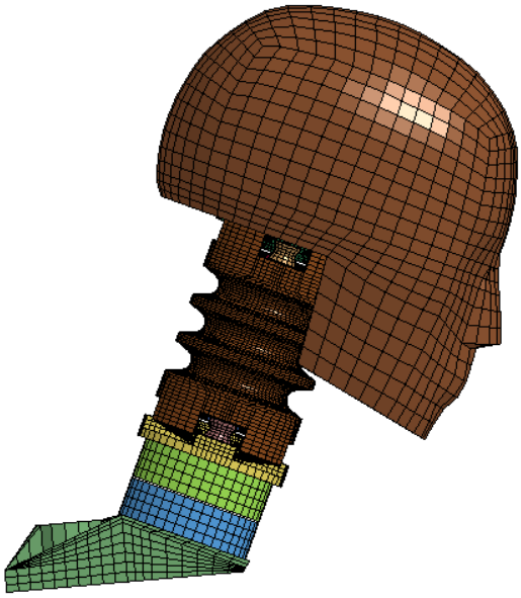

Figure 3.3: Livermore Software Technology Corps LS-Dyna Hybrid III Dummy Head FE model.

The material properties and initial conditions selected for the impactor were chosen to provide impact magnitudes and durations that closely reflect on-field impacts within rugby (D. King et al., 2015). A hyper-elastic rubber constitutive law was used for the impactor (MAT_077_H on LS-DYNA) defined as

$$W(J_1,J_2,J) = \sum_{p,q=0}^{n} C_{pq}(J_1-3)^p(J_2-3)^q + W_h(J)$$

where W_h is the hydrostatic work and the required C_{pq} constants are $C_{10} = 1.07$, $C_{01} = 0.99$, $C_{11} = 0.99$, $C_{20} = 10$, $C_{02} = 0$ and $C_{30} = 10$ [MPa]. These constants describe the strain energy functional, which is a function of the relative volume J and models hyper-elastic rubber behaviour with $J_1 = I_1 I_3^{-1/3}$, $J_2 = I_2 I_3^{-2/3}$, and is explained in great detail in LSTC (2014). This material card was utilised for the impactor as it was the material card used to define the flesh of Hybrid III Dummy Head. The constants values for the impactor therefore were originally based of the constants values selected for the Flesh of the Hybrid III Dummy head. However, upon testing those values, it was evident that the impact magnitude was higher and impact duration was lower than desired, in order to replicate kinematic signals obtained from on field head impacts. This was expected as the Hybrid III Dummy head is not considered an exact representation of the human head (it is comprised of a vinyl deformable skin and steel skull) (Post & Blaine Hoshizaki, 2015). Therefore, constants' values were iterated, by lowering the orders of magnitude and running test simulations, until the kinematic output was within

Table 3.1: Hybrid III Dummy parts list with number nodes, number of elements and mass of each part.

Part Name	Nodes	Elements	Mass [kg]
Upper Neck Mounting Plate	795	528	0.11
Upper Neck Force Gauge - Upper Part	881	528	0.20
Upper Neck Force Gauge - Lower Part	400	176	0.04
Neck Rubber	32232	26432	0.71
Upper Neck Rigid Plate	4688	3104	0.18
Lower Neck Rigid Plate	4688	3104	0.18
Upper Neck Adaptor Plate	3401	1968	0.19
Lower Neck Adaptor Plate	3401	1968	0.19
Upper Neck Central Pivot	1601	1464	0.02
Lower Neck Central Pivot	1601	1464	0.02
Upper Neck Pivot 1	425	256	0.01
Upper Neck Pivot 2	425	256	0.01
Upper Neck Pivot 3	425	256	0.01
Upper Neck Pivot 4	425	256	0.01
Lower Neck Pivot 1	425	256	0.01
Lower Neck Pivot 2	425	256	0.01
Lower Neck Pivot 3	425	256	0.01
Lower Neck Pivot 4	425	256	0.01
Neck Adaptor	2311	1644	4.28
Head Flesh	3273	2120	1.71
Skull	3566	2330	3.44
Lower Neck Force Gauge - Upper Part	1006	800	6.53
Lower Neck Force Gauge - Lower Part	1006	800	6.53
Total	**67400**	**50478**	**24.41**

the desired range, an example of which can be seen from the kinematic output in Figure A.1. Finally, a *Automatic Surface To Surface* contact card was used between the impactor and head flesh parts, with all of the contact card friction coefficients kept to default values for the simulations.

Simulations with the impactor were conducted to replicate impacts on different locations of the head as shown in Figures 3.5a to 3.5d. Side, left-upper-side-frontal, right-upper-side-frontal and lower-side-frontal locations were selected for impacts for the FE simulations with the laboratory test providing a frontal impact. The kinematic output from the simulations were obtained by selecting the Part_ID assigned to the head and selecting linear acceleration and angular velocity tabs providing outputs at the centre of gravity. Tests 1 and 4 were conducted from the same location with differing velocity components applied to the impactor to test the IMLA with different impact levels at the same location as highlighted in Table 3.3. Boundary conditions were applied to the base of the shoulder piece to fix movement in all rotational and linear directions in order to replicate the boundary conditions of the MDOF. Additionally, the simulation duration was set to 30 ms, with a data output time-step of 1 ms to replicate the FIT instrumented mouthguard's operating frequency of 1000 Hz.An analysis was conducted

Table 3.2: Hybrid III Dummy parts list and corresponding material properties [GPa, kg/m^3] .

Part Name	Material Card	Material Properties
Upper Neck Mounting Plate	Rigid (MAT_020)	ρ = 2.65$\times 10^3$, E = 70, v = 0.3
Upper Neck Force Gauge - Upper Part	Rigid (MAT_020)	ρ = 2.65$\times 10^3$, E = 70, v = 0.3
Upper Neck Force Gauge - Lower Part	Rigid (MAT_020)	ρ = 2.65$\times 10^3$, E = 70, v = 0.3
Neck Rubber	Viscous_Foam (MAT_062)	ρ = 2.29$\times 10^3$, E1 = 0.014, E2 = 0.5, V2 = 0.04, v = 0.48
Upper Neck Rigid Plate	Rigid (MAT_020)	ρ = 3.90$\times 10^3$, E = 70, v = 0.3
Lower Neck Rigid Plate	Rigid (MAT_020)	ρ = 3.90$\times 10^3$, E = 70, v = 0.3
Upper Neck Adaptor Plate	Rigid (MAT_020)	ρ = 3.90$\times 10^3$, E = 70, v = 0.3
Lower Neck Adaptor Plate	Rigid (MAT_020)	ρ = 3.90$\times 10^3$, E = 70, v = 0.3
Upper Neck Central Pivot	Rigid (MAT_020)	ρ = 2.65$\times 10^3$, E = 70, v = 0.3
Lower Neck Central Pivot	Rigid (MAT_020)	ρ = 2.65$\times 10^3$, E = 70, v = 0.3
Upper Neck Pivot 1	Viscous_Foam (MAT_062)	ρ = 2.29$\times 10^3$, E1 = 0.014, E2 = 0.5, V2 = 0.04, v = 0.48
Upper Neck Pivot 2	Viscous_Foam (MAT_062)	ρ = 2.29$\times 10^3$, E1 = 0.014, E2 = 0.5, V2 = 0.04, v = 0.48
Upper Neck Pivot 3	Viscous_Foam (MAT_062)	ρ = 2.29$\times 10^3$, E1 = 0.014, E2 = 0.5, V2 = 0.04, v = 0.48
Upper Neck Pivot 4	Viscous_Foam (MAT_062)	ρ = 2.29$\times 10^3$, E1 = 0.014, E2 = 0.5, V2 = 0.04, v = 0.48
Lower Neck Pivot 1	Viscous_Foam (MAT_062)	ρ = 2.29$\times 10^3$, E1 = 0.014, E2 = 0.5, V2 = 0.04, v = 0.48
Lower Neck Pivot 2	Viscous_Foam (MAT_062)	ρ = 2.29$\times 10^3$, E1 = 0.014, E2 = 0.5, V2 = 0.04, v = 0.48
Lower Neck Pivot 3	Viscous_Foam (MAT_062)	ρ = 2.29$\times 10^3$, E1 = 0.014, E2 = 0.5, V2 = 0.04, v = 0.48
Lower Neck Pivot 4	Viscous_Foam (MAT_062)	ρ = 2.29$\times 10^3$, E1 = 0.014, E2 = 0.5, V2 = 0.04, v = 0.48
Neck Adaptor	Rigid (MAT_020)	ρ = 2.50$\times 10^4$, E = 70, v = 0.3
Head Flesh	Hyperelastic_Rubber (MAT_077_H)	ρ = 1.77$\times 10^3$, C_{10} = 10.69, C_{01} = 9.904, C_{20} = 1004, C_{02} = 0,C_{30} = 1005, v = 0.49
Skull	Rigid (MAT_020)	ρ = 2.65$\times 10^3$, E = 70, v = 0.3
Lower Neck Force Gauge - Upper Part	Rigid (MAT_020)	ρ = 2.50$\times 10^4$, E = 70, v = 0.3
Lower Neck Force Gauge - Lower Part	Rigid (MAT_020)	ρ = 2.50$\times 10^4$, E = 70, v = 0.3

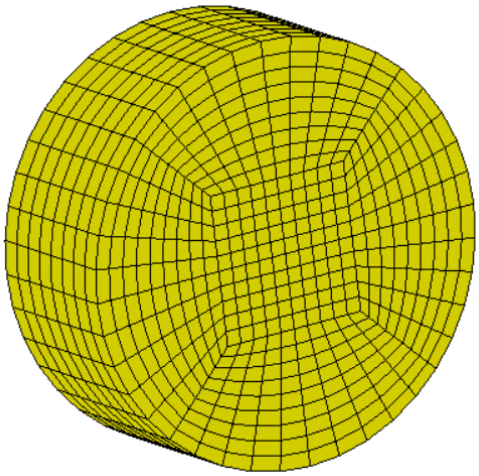

Figure 3.4: Impactor used to conduct the simulation with the Hybrid III Dummy. Highlighting the hexahedral solid reduced integration constant stress finite elements and mesh size used for the impactor.

to determine if higher sampling rates would alter the kinematic output by conducting a simulation at 5000 Hz and comparing linear acceleration components. Figure A.2 shows that the kinematic output is similar between different sampling rates with more unwanted disturbances seen at the higher sampling rate. Since the IMLA requires a data point within the peak linear acceleration phase rather than the exact peak value, 1000 Hz was deemed sufficient as it provided quicker simulation times and smaller output files to handle.

Finally, the setup used for Test 2 was utilised to understand if the IMLA would be able to provide impact locations with a moving model, as players are usually in motions at point of contact. In order to achieve this, for this test the shoulder piece was setup with initial velocity components, specifically -1 and 3 ms^{-1} in the Ox and Oz directions.

Table 3.3: Impactor setup and material properties.

		Test 1	Test 2	Test 3	Test 4	Test 5
Mass [kg]		12.5	12.5	12.5	12.5	12.5
Density [kg/m^3]		4×10^5	4×10^5	4×10^5	4×10^5	4×10^5
$\boldsymbol{u}$ [m/s]	x	2.5	1.5	1.5	1.0	-1.75
	y	0.0	0.0	0.5	0.0	0.0
	z	0.0	-1.5	-1.0	0.0	-1.75

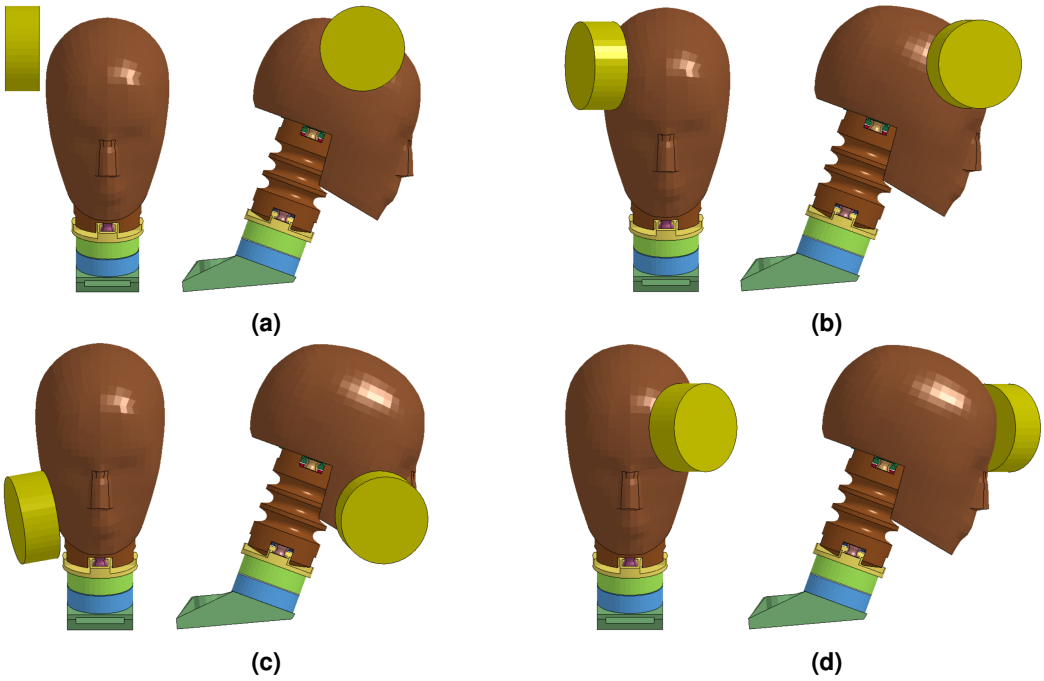

Figure 3.5: Finite Element (FE) simulation setups in LS-DYNA: (a) Test 1 and Test 4 replicating a side impact with impactor initial velocity in the Ox direction (b) Test 2 replicating a left-front-side-upper impact with impactor initial velocity in the Ox and negative Oz direction (c) Test 3 replicating a front-side-lower impact with impactor initial velocity in the Ox, Oy and negative Oz direction (d) Test 5 replicating a right-front-side-upper impact with impactor initial velocity in the negative Ox and negative Oz direction.

3.3.2 Experimental tests

The experimental impact tests were done with a Biokinetics medium-velocity head impact simulator, shown in Figure 3.6 (Siegmund, Guskiewicz, Marshall, DeMarco, & Bonin, 2014b), instrumented with a mouthguard developed by Force Impact Technologies (FIT), similar to the one described in Section 2.2.2. A dental impression was taken of the dentition of the test head which is used to mould a custom fitted mouthguard that affixed securely to the dentition. The same process that is used to make a custom fitted mouthguard for a human athlete is used to mould the instrumented mouthguard for the test head. This mouthguard incorporated a sensor strip anterior to the upper incisors, similar to the one that is being implemented in instrumented mouthguards worldwide (Hernandez et al., 2015; Kuo et al., 2018; Rich et al., 2019). The sensors included are the ones described in Section 2.2.1. The sensors are used in combination to implement an inertial measurement unit with data recorded over a 40 ms window. The test setup used to provide kinematic data to test the IMLA was a right-frontal impact with a 14 kg impactor at 5 m/s. The instrumented mouthguard was positioned over the upper dentition of the test head, replicating the location of an instrumented mouthguard during live impacts.

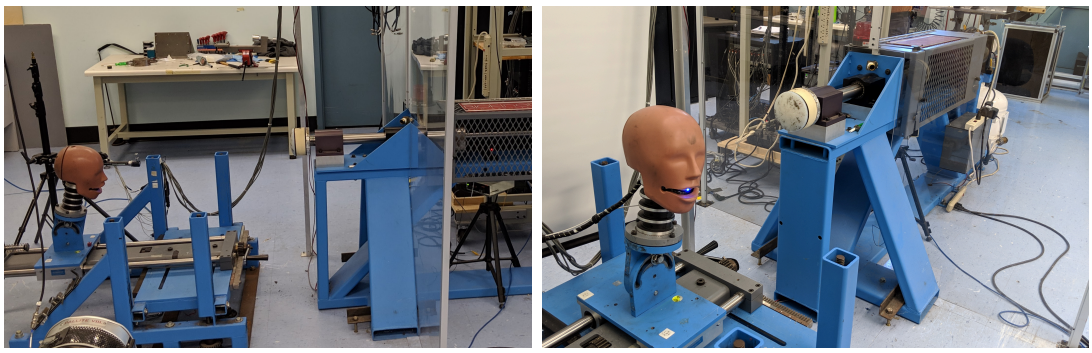

(a) (b)

Figure 3.6: Biokinetics medium-velocity head impact laboratory simulator used to conduct the experimental laboratory tests: (a) showcasing the linear impactor, target table, head-form and (b) highlighting the position of the mouthguard within the head-form.

3.4 Results

Results obtained from the validation studies is highlighted in the following section. This includes the kinematic data from the Experimental test and FE simulations utilised to help validate the IMLA, as well as the output from the IMLA for the validation studies.

3.4.1 Kinematic data

Kinematic data obtained from the experimental test measurements and finite element simulations are shown in Figure 3.7, Appendix A and Table 3.4. The linear acceleration data in Figure 3.7 is collected from the instrumented mouthguard that shows the impact occurring at around 6 ms with a noticeable peak linear acceleration of -8g, 77g and -46g in the Ox, Oy and Oz directions, respectively, starting at approximately 10 ms. The rotational velocity calculated from the laboratory test shows a constant increase after the impact in the negative Ox and positive Oz directions, as expected from a right-frontal impact. Rotational velocity values reached -15 and 14 rad/s in the Ox and Oz directions, respectively. From the obtained kinematic data, the impact duration of the laboratory test was found to be in the 8 to 12 ms range. The linear acceleration in the Oy direction approaches 0 at around 1.4 ms whereas in the Oz direction this happens at around 1.8 ms. Kinematic output obtained from the experimental test was utilised to compare impact locations determined by the IMLA and Bartsch methodologies. For the IMLA, kinematic values were obtained during the peak linear accelerations phase. However, for Bartsch, the kinematic values were taken from the initial phase of the impact, at 8 ms, as stated in the theory presented in Bartsch et al. (2014).

The kinematic response of the FE models, examples of which can be found in Appendix A, show similarities to the laboratory test with regards to the duration and magnitude of the impacts. The impactor material properties were selected to ensure the FE simulations that utilised a validated Hybrid III Dummy head model, provided PLA magnitudes that replicated

Table 3.4: Kinematic results from LS-DYNA simulations.

	PLA (g)				ω at PLA ($\mathbf{rads^{-1}}$)				Duration (ms)
	a_x	a_y	a_z	$\boldsymbol{a}$	ω_x	ω_y	ω_z	$\boldsymbol{\omega}$	
Test 1	70	-8	-5	70.6	-1	-0.2	-13	13	9
Test 2	45	-2	-18	48.5	0.5	13	-4	13.6	8
Test 3	32	15	-5	35.7	0.8	5.2	9.6	10.9	10.6
Test 4	29	-2.8	-1.6	29.2	-0.38	-0.7	-5.5	5.6	11.8
Test 5	-48	10	-40	63.3	-0.3	-10	4	10.8	8

head impacts within non-helmeted sports. The impact durations for all FE simulations are within a 8 to 12 ms range as seen in Table 3.4. Impact durations were established by analyzing the contact data between the head and impactor, as well as the kinematic output as described for the laboratory test. Additionally, PLA as seen in Table 3.4, were 70.6g, 48.5g, 35.7g, 29.2g and 63.3g for Tests 1 to 5 respectively. Furthermore, kinematic output obtained from the moving dummy test is also visible in Figure A.6, showing higher PLA than the ones seen for Test 2 as expected, due to the initial velocity components applied to the Dummy. Finally, the angular velocity obtained with the FE model were of similar magnitude to the laboratory test. Table 3.4 highlights the rotational velocity ($\boldsymbol{\omega}$) components for all tests during the PLA phase of the impacts.

3.4.2 Impact Location and Direction

The IMLA was used for all validation simulations to establish the location of the impact. Figures 3.8 and 3.9 show the direct output from the IMLA, which generates all the analysed coordinates on the surface of the head and highlights the BFN as the calculated location of the impacts. The experimental test was a right frontal impact, replicated by the algorithm, as shown in Figure 3.8e. Also seen in Figure 3.8e is the impact location determined using the Bartsch methodology with the same experimental dataset. The impact location was found to be 35 mm from the desired location.

Additionally, for the Hybrid Dummy III finite element simulations, the BFNs calculated by the IMLA for all impacts correlated to nodes that were struck by the impactor in the simulations. This can be seen when comparing Figure 3.5 with the IMLA output in Figures 3.8 and 3.9. As the impactor strikes more than one node, the distance from the BFN to the impact epicenter, which was defined as the initial point of contact between the impactor and the Hybrid III head, was calculated using LS Dyna measurement tools in order to quantify the accuracy of the impact location. All tests provided a BFN that was within the contact area with the BFN for Tests 4 and 5 replicating the same node as the epicenter of the impact. However, for Tests 1, 2 and 3, the calculated BFN was found to be a neighboring node with the impact epicenter being

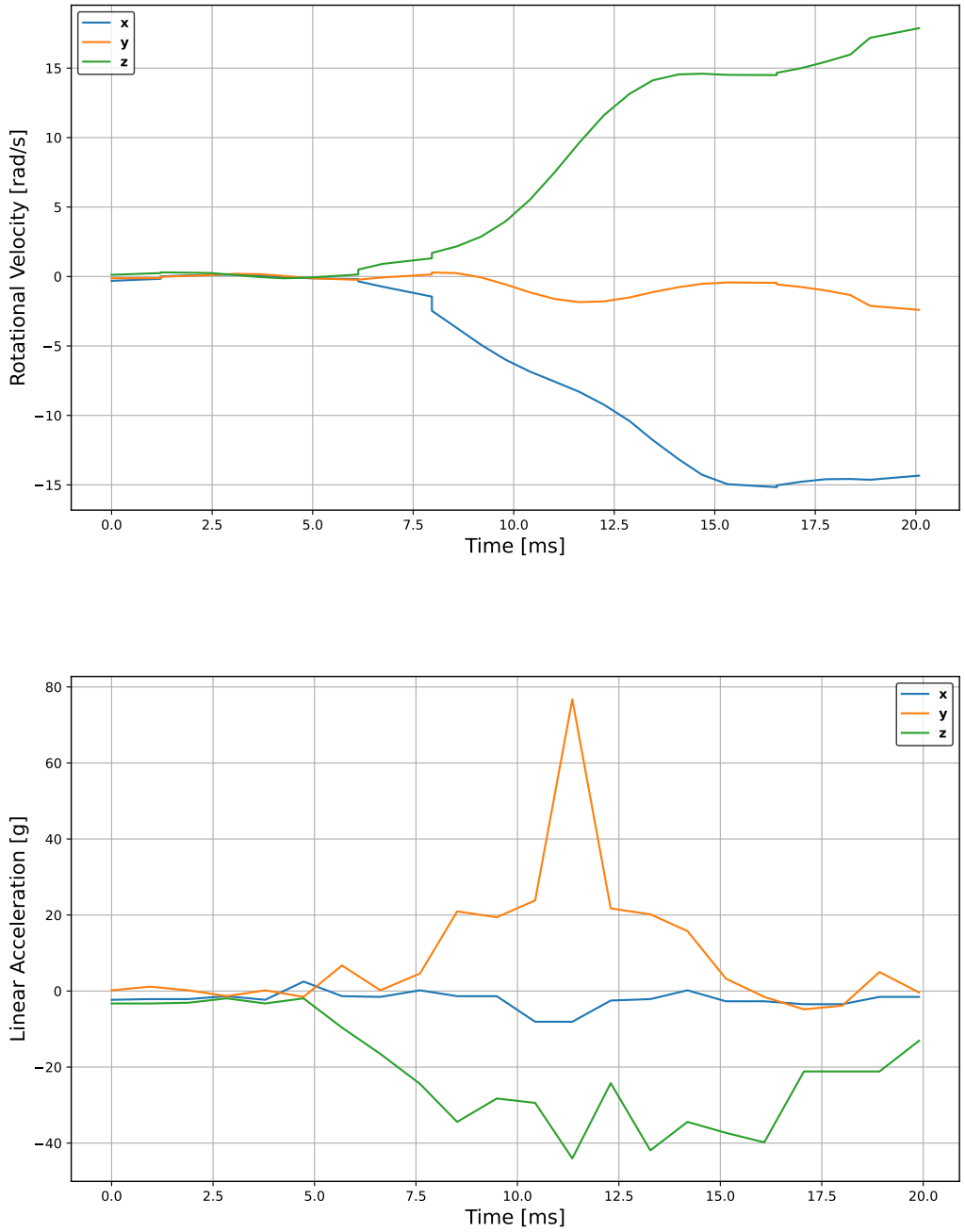

Figure 3.7: Kinematic response of the head during the laboratory test collected via FIT instrumented mouthguard in the Ox, Oy and Oz directions: rotational velocity and linear acceleration.

a distance of 10.8, 9.9 and 11.6 mm away respectively. Additionally, the moving dummy tests BFN, as seen in Figure 3.8g, replicated the node contact was made with by the impactor. As the setup used was the same as for Test 2 with the dummy also in motion, the impact location was expected to be more towards the side than the location determined for Test 2.

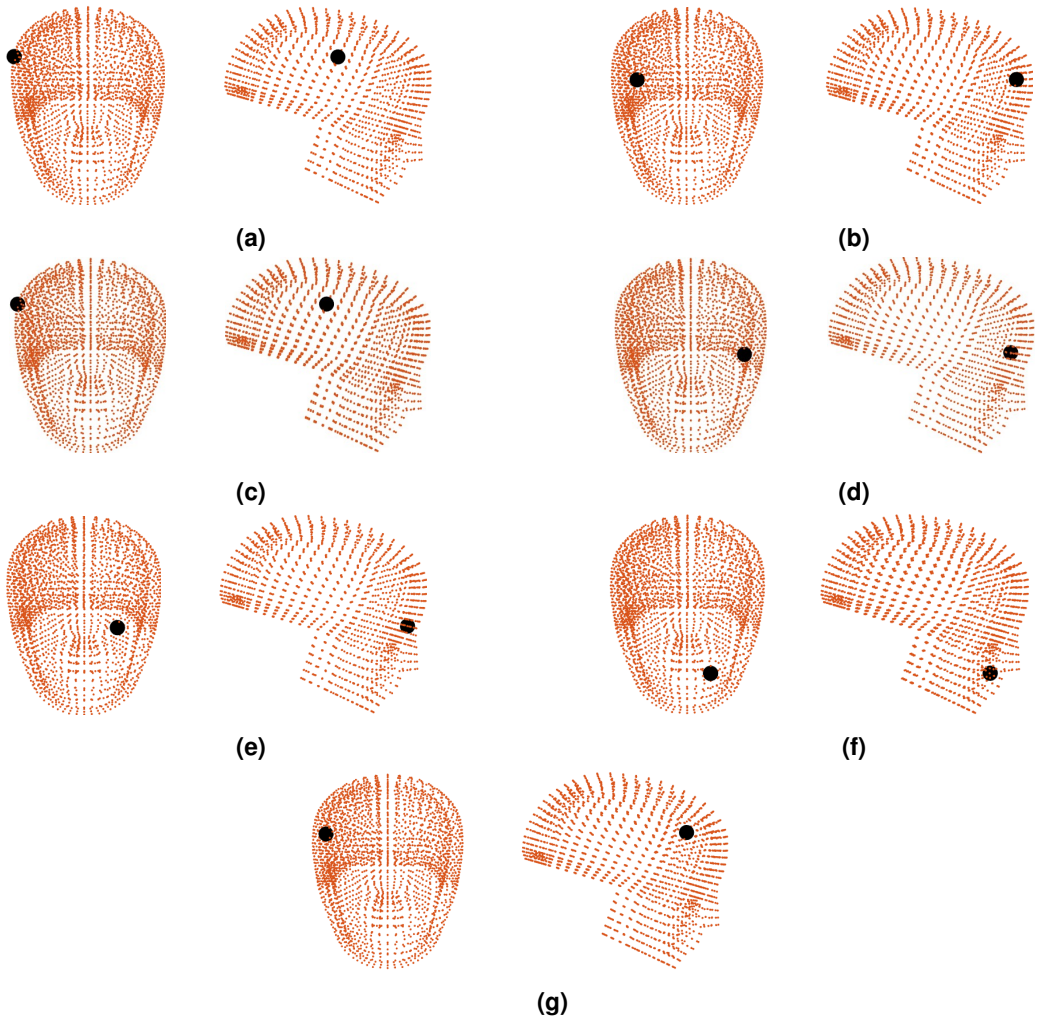

Figure 3.8: Impact location, highlighted in black, on the xy and yz planes for (a) Test 1, (b) Test 2, (c) Test 4, (d) Test 5, (e) Experimental test (IMLA), (f) Experimental test (Bartsch) and (g) Moving Dummy.

Furthermore, Figure 3.9 highlights the impact location process for Test 3, as described in Section 3.2. The initial stage of the process matches moment directions which eliminates the majority of the nodes, as shown in Figure 3.9a. Further nodes are eliminated by the addition of tolerances while matching moments and ensuring the impact vector can physically target the node, leaving a cluster of nodes in the cheek/jaw region, as seen in Figure 3.9b. At this stage, although a good approximation of the impact location can be determined, the BFN can be established by reducing tolerances for each direction as highlighted in Figure 3.9c.

Table 3.5: Moment values as calculated from Euler's and torque equations.

	$\boldsymbol{T}$ [Nm]			$\boldsymbol{T_t}$ [Nm]			$\boldsymbol{\delta}$ (%)		
	T_x	T_y	T_z	T_{tx}	T_{ty}	T_{tz}	δ_x	δ_y	δ_z
Test 1	-3.1	29.8	-83.3	-3.8	26.9	-82.5	22.5	9.7	1.0
Test 2	-4.0	81.0	-30.0	-3.9	81.8	-29.9	0.3	1.0	1.0
Test 3	-4.6	41.9	22.7	-7.0	30.0	23.3	52.2	28.4	2.6
Test 4	-1.0	8.4	-22.8	-0.8	7.7	-23.7	20.0	8.3	3.9
Test 5	-19.9	-51.6	23.9	-24.0	-46.1	17.0	20.6	10.7	28.9
Lab	-14.5	-2.5	17.3	-17.2	-2.0	4.5	18.6	20.0	74.0

Moreover, components of $\boldsymbol{T}$ established from Equation 3.1 for the peak acceleration phase of each impact, components of $\boldsymbol{T_t}$ from Equation 3.13 for the BFN and the tolerance ($\boldsymbol{\delta}$) components required for the algorithm to establish the BFN for all conducted tests are listed in Table 3.5. The $\boldsymbol{\delta}$ components are established relative to components of $\boldsymbol{T}$ using

$$\boldsymbol{\delta} = 100\left(\frac{\boldsymbol{T}-\boldsymbol{T_t}}{\boldsymbol{T}}\right) \tag{3.14}$$

Additionally, Table 3.6 lists the approximated force, $\boldsymbol{F_t}$, established from the MDOF and the corresponding unit vector ($\hat{\boldsymbol{F}}_{\boldsymbol{t}}$), as well as the unit vector of the applied force in the simulation ($\hat{\boldsymbol{F}}_{\boldsymbol{s}}$) to determine the accuracy of the impact directions as calculated by the IMLA. As seen in Table 3.6, the difference between components of $\hat{\boldsymbol{F}}_{\boldsymbol{s}}$ and $\hat{\boldsymbol{F}}_{\boldsymbol{t}}$ is within ± 0.03 with the percentage difference ($\%\Delta$) relative to $\hat{\boldsymbol{F}}_{\boldsymbol{s}}$ being less that 11% for all conducted tests, highlighting the accuracy at which the IMLA calculates impact direction.

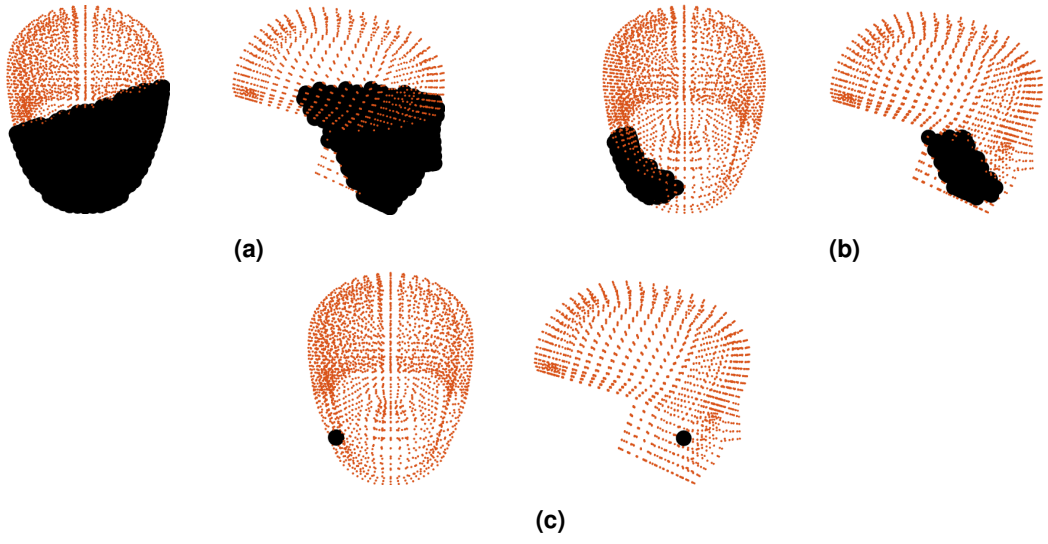

Figure 3.9: Impact location process for Test 3 on the xy and yz planes: (a) matching $\boldsymbol{T}$ and $\boldsymbol{T}_t$ signs (b) matching $\boldsymbol{T} \pm 100\%$ and $\boldsymbol{T}_t$ values and (c) reducing tolerances to find the BFN.

Table 3.6: Magnitude of the impact force as measured by the MDOF model ($\boldsymbol{F_t}$) and comparison between the orientations of the applied force (direction cosines) as obtained by the numerical model ($\hat{\boldsymbol{F}}_{\boldsymbol{s}}$) and the IMLA ($\hat{\boldsymbol{F}}_{\boldsymbol{t}}$). The relative difference between the two approaches is also listed (Δ).

Test	Component	$\boldsymbol{F_t}$ [N]	$\hat{\boldsymbol{F}}_{\boldsymbol{s}}$	$\hat{\boldsymbol{F}}_{\boldsymbol{t}}$	Δ [%]
Test 1	x	1230	0.99	0.99	0.13
	y	-150	-0.12	-0.12	2.52
	z	-102	-0.07	-0.08	6.94
Test 2	x	900	0.92	0.93	0.75
	y	-81	-0.09	-0.08	8.13
	z	-333	-0.37	-0.35	4.14
Test 3	x	550	0.91	0.91	0.23
	y	230	-0.36	-0.38	4.67
	z	-110	-0.21	-0.18	10.68
Test 4	x	400	0.99	0.99	0.60
	y	-46	-0.1	-0.11	6.86
	z	-27	-0.06	-0.06	4.76
Test 5	x	-834	-0.75	-0.75	0.43
	y	177	-0.15	-0.16	5.26
	z	-710	-0.66	-0.64	2.42
Lab	x	-118	–	-0.16	–
	y	250	–	0.35	–
	z	-660	–	-0.92	–

3.5 Discussion

The proposed algorithm utilises rigid body motion dynamics to establish impact locations, building upon the work of Bartsch et al. (2014). However, unlike the assumption that the head rotates about the CoG made by Bartsch et al., the IMLA establishes rotations about the head/C1 joint and uses an additional MDOF system to replicate the kinematics of the head and neck to determine the impact direction, rather than assuming it is a free body. Furthermore, the IMLA determines position vectors and inertias from a Hybrid III Dummy model, incorporating the non-spherical shape of the human head, as opposed to using a simpler spherical geometry. Finally, the moment matching technique stated in Section 3.2 allows nodes to be eliminated till the BFN is found, rather than determining the position vector, as stated by Bartsch et al.. Rather than approximating an impact region, this technique provides the ability to pinpoint the impact location to within 14 mm of the impact center, as

highlighted in Section 3.4. The methodology used by Bartsch was utilised on the experimental test to compare the output with the IMLA, where it was evident that the methodology could be used to establish an impact region, but isn't able to pin point the impact location as accurately as the IMLA.

Tables 3.5 and 3.6 highlight the numerical output from the algorithm with regards to Euler's moments , torque moments, approximated force magnitude and impact direction. The approximated force components calculated by the MDOF was 40% of the force values seen within the LS-DYNA simulations, which is potentially due to the MDOF stiffness not representing the complex human head and neck stiffness. For the purpose of this research, the MDOF was considered to be a linear system, incorporating the intervertable linear stiffness established by Luo and Goldsmith (1991), whereas the Hybrid III Dummy head replicates a human head incorporating stiffness of muscles as well as intervertebral joints in 6 degrees of freedom, and therefore stiffer than the MDOF. The impact direction vector, however, was unaffected, with components of $\hat{\boldsymbol{F}}_{\boldsymbol{t}}$ being within $\pm$ 0.03 (11%) of the components of $\hat{\boldsymbol{F}}_{\boldsymbol{s}}$, as can be seen in Table 3.6, due to the components of the force all being underestimated by the same fraction.

Despite the underestimated nature of the approximated force magnitude, the components of $\boldsymbol{T}_t$ listed in Table 3.5 for the BFN closely reflect the components of $\boldsymbol{T}$ established by Equation 3.1. This observation is potentially due to the head and neck acting as a two pivot point system as described by Van Drunen (2009), resulting in only a fraction of the total impact force rotating the head about the head/C1 joint. The approximated nature of the impact force magnitude causing rotations about the head/C1 joint is hypothesised as the primary reason for the difference between the components of $\boldsymbol{T}$ and $\boldsymbol{T}_t$, listed in Table 3.5 for all impacts.

Moreover, the difference seen in Table 3.5 for the experimental test was larger than that of the FE simulations with δ_z being as high as 74%. One potential reason for this could be due to the FIT instrumented mouthguard gyroscope and linear accelerometers operating at different frequencies, as stated in Section 3.3. For the purpose of the IMLA, rotational velocity components were established for the timestamp with the lowest difference to the linear acceleration components timestamps. This results in rotational velocity components utilised in Equations 3.1, and linear acceleration components in Equation 3.12 being for differing time stamps which in turn means $\boldsymbol{T}$ and $\boldsymbol{T}_t$ values are obtained for differing timestamps. Some instrumented mouthguards in use currently house an accelerometer and gyroscope that operate at the same frequency. However, like the FIT mouthguard, some mouthguards house sensors that operate at differing frequencies, and therefore will induce small errors as kinematic data required for the IMLA will be obtained for differing timestamps (Liu et al., 2020).

Furthermore, the experimental test replicated a live impact to validate the IMLA with variables that would be unknown to researchers utilising instrumented mouthguards. Player heads vary in size and shape and it is not possible to accurately measure head dimensions when analysing impacts which in turn will incur errors within variables such as $\boldsymbol{r}$ and $\boldsymbol{d}$ that require

accurate values (distances). For the experimental test, the head shape utilised differed from the Hybrid III however, the coordinates required to establish $\boldsymbol{r}$ in Equation 3.13 were obtained from the nodes on the surface of the Hybrid III Dummy FE model and the head/C1 rotation point of the Hybrid III. Additionally, $\boldsymbol{d}$ was also determined from the Hybrid III which will incur errors within the algorithm.

A detailed sensitivity analysis was conducted to establish how sensitive $\mathbf{a}_{CoG}$ and $\boldsymbol{T}_t$ are to changes in $\boldsymbol{d}$ and $\boldsymbol{r}$. The observations listed in Table 3.7 show that a change in $\boldsymbol{d}$ by 1% results in a change of 0.15, 0.11 and 0.07$\%$ in a_{CoGx}, a_{CoGy}, a_{CoGz}, respectively, meaning that inaccuracies within $\boldsymbol{d}$ do not affect significantly the IMLA's output. Inaccuracies within $\boldsymbol{d}$ are expected as the position vector from the CoG to the mouthguard would be estimated for live impacts as it is not possible to calculate the distance accurately in humans. Changes in $\boldsymbol{r}$, however, were found to be proportional to changes in components of $\boldsymbol{T}_t$, highlighting the sensitive nature of components of $\boldsymbol{T}_t$ to changes in $\boldsymbol{r}$ as can be seen in Table 3.8. The sensitive nature of $\boldsymbol{r}$ could result in the IMLA returning an impact location out with the 14 mm tolerance, if the shape of the head differs significantly from that of the FE head model. The test conducted in the laboratory, however, highlighted that head shape differing to the FE model still provided correct impact locations, with higher tolerances required to establish the BFN. Moreover, inertia values used in Equation 3.1 are established from the Hybrid III, which will result in small errors due to the shape of the Hybrid III Dummy differing from the head-form used in the experimental test.

Table 3.7: Sensitivity analysis of components of $\boldsymbol{a}_{CoG}$ to changes in $\boldsymbol{d}$.

$\%\Delta\boldsymbol{d}$	$\%\Delta a_{CoGx}$	$\%\Delta a_{CoGy}$	$\%\Delta a_{CoGz}$
-30	-4.58	3.20	-2.15
-20	-3.03	2.13	-1.43
-10	-1.51	1.06	-0.72
10	1.51	-1.08	0.72
20	3.04	-2.15	1.45
30	4.55	-3.22	2.17

Table 3.8: Sensitivity Analysis of components of $\boldsymbol{T}_t$ to changes in $\boldsymbol{r}$.

$\%\Delta\boldsymbol{r}$	$\%\Delta\ T_{tx}$	$\%\Delta\ T_{ty}$	$\%\Delta\ T_{tz}$
-30	-30.04	-30.41	-30.13
-20	-20.03	-20.41	-20.17
-10	-10.02	-10.41	-10.17
10	10.02	10.41	10.13
20	20.03	20.41	20.17
30	30.05	30.41	30.17

Finally, a limitation of the algorithm occurs with the moment matching technique described in Section 3.2.3, specifically with the matching component signs aspect of the algorithm. With live impact kinematic signals, components of $\boldsymbol{T}$ close to zero could change sign due to the unwanted disturbances within the signals. This in turn could result in nodes that are required being eliminated by the sign matching aspect of the IMLA described in Section 3.2.3, providing an inaccurate impact location. The algorithm is, nonetheless, efficient for the conducted tests in determining the location of the impact by eliminating nodes until only one remains, meaning the moments difference between $\boldsymbol{T}$ and $\boldsymbol{T}_t$ due to the discrepancies stated above does not hinder the algorithm's ability to provide an accurate impact location. However, further testing is required with live impact data collected from instrumented mouthguards to establish if the supplied methodology is able to provide accurate impact locations within non-helmeted contact sports with kinematic signals that may house unwanted disturbances as they could hinder the algorithm.

3.6 Conclusion

An algorithm to determine the impact magnitude and location of an impact on the head was developed to aid research regarding head impacts in non-helmeted contact sport. The algorithm utilises a combination of rigid body dynamics and a multi degree of freedom (MDOF) system, and is validated with kinematic data from Hybrid III Dummy FE simulations and laboratory testing with an instrumented mouthguard. The five FE simulations and the laboratory test replicated impacts of varying magnitudes and locations to test the performance of the proposed algorithm (IMLA). The output from the algorithm correctly determines the impact locations for the simulations as the best fitting node (BFN) calculated by the IMLA is within 14 mm of the impact center for all conducted tests, meeting the criteria for an accurate impact location. Additionally, the mean percentage difference in moments values established from Euler's equations (Equation 3.1) and the torque equation (Equation 3.13)for FE Tests 1 to 5 were calculated to be 11, 0.7, 27.7, 10.7 and 20$\%$. As expected, however, the mean percentage difference for the laboratory test was significantly higher (at 37.7$\%$) and therefore higher tolerances than the FE simulations were required to determine impact locations due to the uncertainty in head dimensions. Further testing with live on field impacts is required to test the methodology. The IMLA has, however, the potential to significantly aid researchers conducting field tests within non-helmeted sports with instrumented mouthguards by reducing the time required to analyze kinematic data and determine head impact locations.

Chapter 4

Impact Location Using Clustering Algorithms

4.1 Introduction

The work presented within this chapter provides an alternative method to determine impact locations to the method described in Chapter 3. This method may be more robust, have fewer limitations and be more easily integrated with existing mouthguard technology. Additionally, this method has the potential to be cost effective as computing time required to provide impact locations are hypothesised to be lower than the 17 seconds required to locate one impact using the IMLA. The methodology proposed in this chapter differs from the one utilised in Chapter 3 as it uses machine learning (ML) algorithms with kinematic data sets replicating ones obtained from instrumented mouthguards, to determine impact location regions. As discussed in Chapter 3, existing methodologies to determine impact locations by Bartsch et al. (2014) and Kuo et al. (2018) have provided results that can be improved on, therefore requiring a methodology to aid the research field.

Machine learning is a subset of Artificial Intelligence (AI) that makes predictions from data. ML algorithms are extensively being utilised in numerous sectors such as transport, finance and healthcare transforming the industries and enabling new capabilities. Within healthcare, ML models assist in disease diagnosis, treatment planning, and personalised medicine whereas within finance, they are used for fraud detection, credit scoring, algorithmic trading, and risk management as they are able to analyse large volumes of financial data to identify patterns and trends (Esteva et al., 2017; Ngai, Hu, Wong, Chen, & Sun, 2011).

ML comes in two main forms, Supervised and Unsupervised Learning. Supervised learning uses labelled training data sets to determine outputs and is usually used for classification and regression problems, whereas unsupervised learning algorithms learn and develop trends within unlabelled data sets. Unsupervised learning is often used for clustering similar data sets together (Alizadehsani et al., 2021; Caruana & Niculescu-Mizil, 2006). Both methods have been extensively utilised within wearable sensors in different fields, with supervised learning applications including classification models for electrocardiogram signals to monitor

cardiac disease (Saadatnejad, Oveisi, & Hashemi, 2019), and development of a classification model to identify breathing anomalies for patients (Acharya & Basu, 2020). Unsupervised clustering algorithm applications have included telemonitoring of patients with Parkinson's disease (Borthakur, Dubey, Constant, Mahler, & Mankodiya, 2017), detection of poor posture (Gupta, Gupta, & Aswal, 2021), and other applications (Mejia-Ricart, Helling, & Olmsted, 2017; Weber, Härmä, & Heskes, 2017). Within sports, existing research has used ML algorithms with wearable sensors in cricket (Jowitt, Durussel, Brandon, & King, 2020; McGrath, Neville, Stewart, Clinning, & Cronin, 2021), rowing (Bosch et al., 2015), running (McGinnis et al., 2017), general exercise (Um, Babakeshizadeh, & Kulić, 2017) and with instrumented mouthguard kinematic data, highlighting the potential for the proposed methodology within this chapter.

Existing research conducted with instrumented mouthguard kinematic data includes the use of supervised learning methods to classify impacts from non impacts such as the work conducted by L. C. Wu, Zarnescu, Nangia, Cam, and Camarillo (2014) and Fanton, Gaudio, and Ling (n.d.). These researchers utilised a Support Vector Machine (SVM) classifier and Neural Networks with feature data sets established from kinematic data to classify true impacts to great accuracy. Additionally, Zhan, Liu, Cecchi, et al. (2021), S. Wu, Zhao, Ghazi, and Ji (2019) and Zhan, Liu, Raymond, et al. (2021) successfully applied ML techniques to understand brain dynamics and brain strain. Clustering algorithms have also been successfully used by Zhan, Li, et al. (2021) to enable head impact subtyping for better traumatic brain injury prediction. They utilised the K-means algorithm to determine clusters of kinematics in a completely data driven manner. The research utilised 16 features within the features data set, which consisted of components of linear acceleration, rotational velocity, rotational acceleration and rotational jerk to split the entire data set in two, to great success.

The research described in this chapter focuses on utilising clustering algorithms to determine impact location regions from synthetic kinematic data replicating mouthguard data. This was conducted by using a combination of position values calculated from integrating kinematic signals, and Fast Fourier Transform (FFT) of kinematic signals within features data sets. Additionally, the research explores the potential concept of using clustering algorithms as a classifier for new data, which could be integrated with existing mouthguard technology.

4.2 Methodology

The method proposed to determine the impact location region is based on clustering algorithms with specific features obtained from mouthguard kinematic signals. Clustering algorithms provide the user with a method to group data samples together based of similarities between their features, which for the purpose of this study results in impacts from the same region on the head being grouped together in a data driven manner. The methodology requires the creation of synthetic data which replicates signals obtained from instrumented mouthguards with regards to frequency, magnitude and duration. The main steps taken within this research to determine impact location regions can be summarised as:

1. Creating a varied synthetic kinematic data set.
2. Determining important features from the synthetic kinematic data to create features data sets.
3. Preparing the features data set to be fit for use with clustering algorithms. This can include normalising features so they are all within the same order of magnitude.
4. Utilising clustering algorithms on the features data set to group together similar data samples and therefore determine impact regions for each impact.

4.2.1 Synthetic Data Creation

The model of the impactor used in the numerical simulations alongside the Hybrid III Dummy FE model, described in Section 3.3.1, was designed to allow for impact peak linear acceleration magnitudes between 20 and 100 g and peak durations between 8 and 12 ms, replicating on-field impacts within contact sports (D. King et al., 2015). However, since using that model to create kinematic impact data to validate the IMLA, an open-source Hybrid III dummy model has been made available by Biomechanics Consulting and Research, LC (Biocore) (LLC, 2024). The Biocore Hybrid III FE model has been extensively validated against experimental data, ensuring its accuracy and reliability in predicting human injury mechanisms. It features a comprehensive representation of human anatomical structures, including the head and neck, enabling researchers to investigate the effects of various impact parameters and allowing for validated kinematic output. Recently, the Biocore head and neck model has been consistently utilised within sports safety and protective equipment design research (Decker et al., 2020; Giudice et al., 2019). Additionally, the model consists of 53,000 nodes, which is fewer than the FE model utilized in Section 3.3.1, allowing for more efficient simulations and reducing simulation time and cost. Due to the significantly higher number of simulations required to test the theory presented in this chapter, as well as the need for longer simulations than those required in Section 3.3.1, the Biocore Hybrid III model was selected as the source to supply the kinematic synthetic data.

Biocore Hybrid III Model

Biocore hybrid III model was available to download from LLC (2024). The model downloaded was the "Helmet Assessment Tools v2", which incorporated a hybrid III dummy model, an impactor and a neck-mount, and was used on LS-DYNA. The parts of the hybrid III dummy, along with their corresponding nodes and elements, are listed in Table 4.1 and can be visualised in Figure 4.1. The impactor, as seen in Figure 4.2, is constructed with a ram, stoppers to halt the impactor, and a nylon end cap. The model was utilised mostly as downloaded; however, a *rigid body* constraint was applied between the neck mount and disk 1 after importing the neck mount into the Hybrid III model. Additionally, after importing the impactor, an *automatic surface to surface* contact card was applied to the impactor's nylon end cap and the head skin.

Table 4.1: Hybrid III Dummy parts list with number nodes, number of elements and mass of each part.

Part Name	**Nodes**	**Elements**	**Mass** [kg]
Head Skin	19696	19446	1.20
Head	7050	6988	3.53
Head Bottom	1369	752	0.84
Neck Rubber	15456	11360	0.37
Disk (x5)	9840	6840	0.75
Neck Top	953	564	0.32
Bottom Nut	173	104	0.18
Top Nut	135	80	0.02
Neck Cable Beams	50	48	0.04
Neck Mount	2127	1364	17.7
Total	**53297**	**47050**	**24.95**

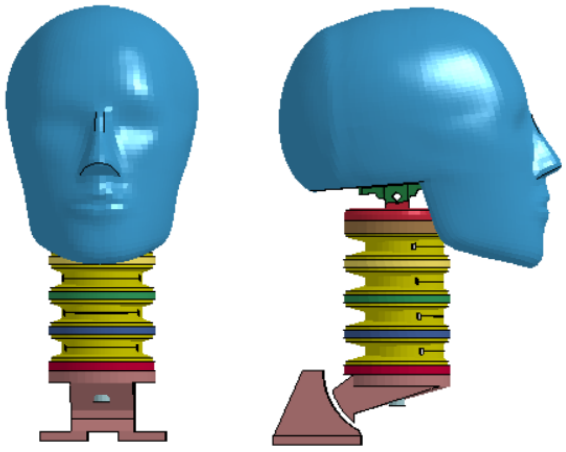

Figure 4.1: Biocore Hybrid III Dummy model visualised from multiple views

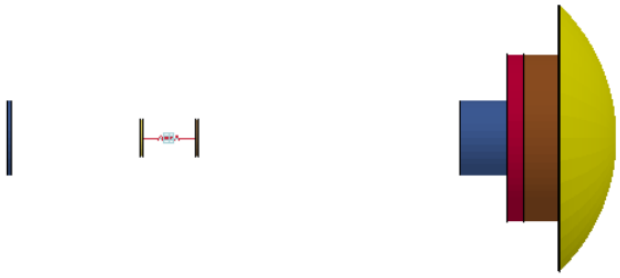

Figure 4.2: Biocore impactor utilised to produce synthetic head kinematics

Simulation Setup

Impact simulations were conducted on six impact zones on the head, as shown in Figure 4.3, in order to collect data sets from varying impact locations to test the clustering methodology. No impacts were simulated on the top and back of the head as impact zones were determined based of ones reported by existing research within Rugby, where it was found those impact zones were rarely impacted (D. King et al., 2015). 8 impacts were conducted within each impact zone with impactor velocity varying between 2 and 7 ms^{-1} complying with impactor velocities seen within existing research (Decker et al., 2020; Giudice et al., 2019). Additionally, the Hybrid III dummy was rotated creating a data set with impacts from different angles within the same region in order to add variability within the dataset. Additionally, to test the clustering algorithm further, additional 4 impacts were conducted in-between the above identified zones to understand how the clustering algorithms processes impacts that may exist in between zones, which were represented by a circle in Figure 4.3. Finally, the clustering methodology required a testing data set, which was simulated and highlighted as squares in Figure 4.3.

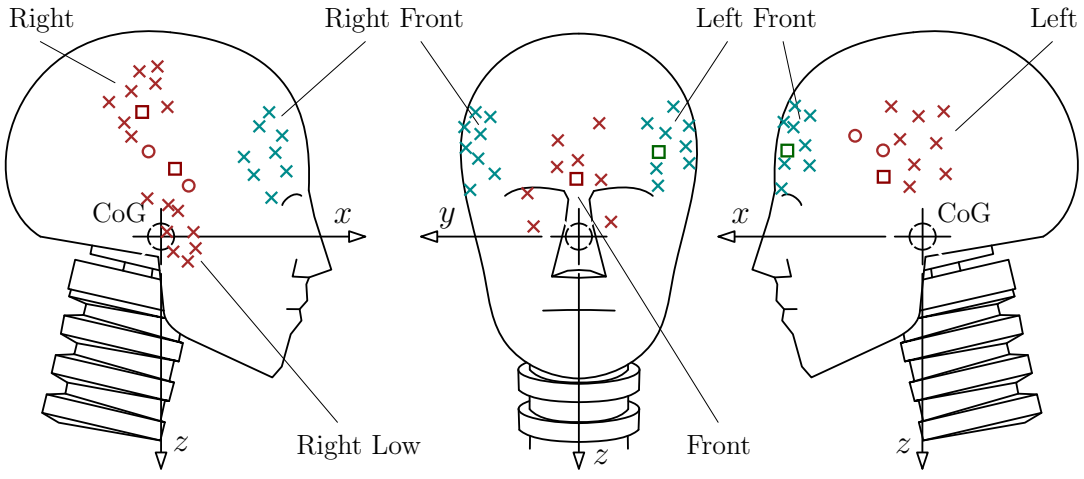

Figure 4.3: Locations of simulated impacts within the six identified zones. "X" are the original impact within identified zones, circle are impacts between zones and square are impact for the testing data set. Red impacts are visible in one plane, green are visible in two planes.

Boundary conditions were applied to the neck mount of the Hybrid III Dummy head/neck model, restricting rotational motion in all directions and linear motion in the Oz direction. This was done to replicate the motion of the model on the rails (allowing for linear motion only) during impact laboratory testing as stated in existing research (Giudice et al., 2019), differing from the boundary conditions applied in Chapter 3 which were setup to replicate the MDOF system. The 0.3125 ms time-step for the simulation was selected to replicate data from a 3200 Hz mouthguard as leading mouthguards operate at this frequency (B. Jones et al., 2022). Moreover, similarly to the kinematic data set obtained from the instrumented mouthguards, the simulations' output was rotational velocity and linear acceleration components. Linear accelerations were obtained for node 5631, situated below the nose of the Hybrid III dummy head on the center line, replicating the location of the central incisors. This correlated well with the location of kinematic data sensors in instrumented mouthguards while in use as described in Section 2.2.2.

4.2.2 Machine Learning Models

Two popularly utilised clustering algorithms in metric spaces were used to determine impact location regions: K-means and Fuzzy C-means clustering (Yuan & Yang, 2019). K-means clustering is a hard clustering algorithm with a primary goal of finding definitive groups in a data set by minimising the sum of distances between each sample and its cluster centroid as seen in Figure 4.4. The number of groups determined by the algorithm is calculated by a user-defined value of K. Initially, the algorithm estimates K cluster centroids and assigns all data points to the nearest cluster centroid based on squared euclidean distances. The centroids are then recalculated by taking the mean of all the data samples allocated to each specific cluster. The process is repeated till convergence or a user-defined stopping criteria is met. The objective of the algorithm is to minimise the squared error function:

$$J_{se} = \sum_{j=1}^{K} \sum_{i=1}^{n} ||x_i^{(j)} - c_j||^2 \tag{4.1}$$

where, K is the number of clusters, n is the number of cases, x_i refers to case i and c_j to the centroid of cluster j.

Fuzzy C-means (FCM) clustering on the other hand is a soft clustering algorithm that assigns a membership value of each sample to each cluster based on the distance between the data sample and the cluster centers, as highlighted in Figure 4.4. The sum of the cluster memberships for each data sample equates to 1, with the highest membership value determining the cluster centroid a data sample is closest to. Like K-means clustering, the FCM algorithm initially estimates cluster centers and calculates the fuzzy membership of each data point based of the centers, after which the fuzzy centers are recalculated and the process is

repeated. The main objective of the FCM algorithm is to repeat the process and minimise:

$$J_{se} = \sum_{j=1}^{C} \sum_{i=1}^{n} (\mu_{ji})^m ||x_i - c_j||^2 \tag{4.2}$$

where C is the number of clusters, μ_{ji} is the membership of the i^{th} data point to the j^{th} cluster and m is the fuzziness index. FCM was utilised as a method to understand impacts that may occur within the fringes of two impact zones. It is hypothesised that by quantifying the membership of a data sample, a better understanding of impact location can be made for impacts that may fall in between regions. Additionally, FCM houses a predict function that can be used to fit new data samples within an existing model. This provides FCM with the ability to become a classifier of new data as well as a clustering algorithm, which can be useful in this research field in quantifying live impact locations.

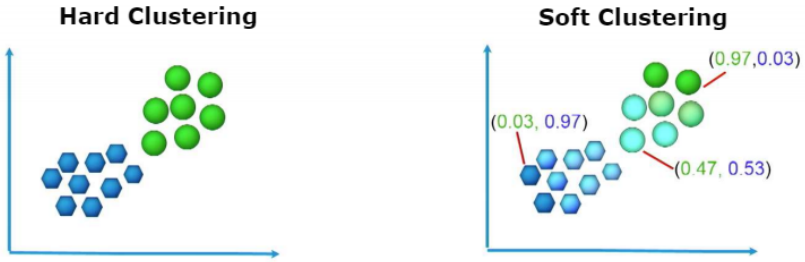

Figure 4.4: Example of difference between Hard and Soft Clustering (Chhikara, 2021).

4.2.3 Feature Selection

Features from the synthetic signals are selected to provide the clustering algorithm with the best opportunity to distinguish between data samples of differing impact zones. Combinations of linear and rotational displacement and the amplitudes from the Fast Fourier Transform (FFT) of linear acceleration and rotational velocity signals were utilised to create feature data sets for the clustering algorithms.

Linear and rotational displacements were selected as a feature, due to the promise shown from existing research. The work conducted by Kuo et al. (2018) utilised displacement vectors to help determine impact location, concluding that it was more effective than traditional peak linear acceleration methods. Linear acceleration and rotational velocity signals were converted to linear and rotational displacement vectors by mathematical integration. The raw signals were converted to mimic the type of signals that would be obtained from instrumented mouthguards. Displacement values for the features data set were selected for the timestamp that represented the end of impact resulting in a total of six displacement features, three rotational and three linear, added to the features data set.

Additionally, FFT of the kinematic signals obtained from the simulations were hypothesised as a promising method to create a features data set as highlighted in existing research Fanton et al. (n.d.); Zhan, Li, et al. (2021). FFT converts the signals into the frequency domain, as shown in Figure 4.5. It was, however, observed that there was a severe mirroring issue with regards to using FFT on its own within a features data set. For example, FFT amplitudes of linear acceleration components for an impact occurring in the "Right" and "Left" zones would provide similar results, hence the clustering algorithm would struggle to differentiate between the two impact zones. Therefore, displacement components were required alongside the FFT signals within the features data set to differentiate between said impacts. FFT amplitudes were computed in increments of 11.8 Hz from 0 to 1600 Hz, as each impact signal had an 85 ms time window sampling at 3200 Hz. This in turn resulted in 136 features per component of kinematic signal within the features data sets. Additionally, it was observed that the kinematic signals were low frequency signals, therefore an optimised linear acceleration signal and rotational velocity signal FFT, dismissing high frequency amplitudes, was also tested to see if feature reduction produced better results from the clustering algorithms.

The following three features data sets were tested:

FD1: Linear and rotational displacement (6 features)

FD2: Linear and rotational displacement (6 features) + linear acceleration and rotational velocity FFT (816 features)

FD3: Linear and rotational displacement (6 features) + optimised linear acceleration signal and rotational velocity signal FFT (60 features)

where components of optimised FFT features in FD3 included amplitudes from 0 to 100 Hz. From observation of all kinematic signals FFTs, it was determined that 100 Hz was a reasonable cutoff value, as it provided the valuable low frequency features that dominate kinematic signals, all the while ensuring a sufficient feature reduction from the original features data set. Additionally, because clustering algorithms use Euclidean distance, features within the features data sets were required to be within the same order of magnitude. Therefore, all features were normalised, reducing the magnitudes while still keeping the same ratios between the components. Displacement features were normalised between -1 and 1, with FFT features between 0 and 1 due to the FFT producing only positive values.

4.2.4 Performance Testing

The performance of the clustering algorithms was quantified by calculating the classification rate of all three feature datasets (FDs). Additionally for K-means clustering, principle component analysis (PCA) plots, that help visualise the groupings, are analysed to test if the algorithm produces cluster formations that follow logical sense, for example "Right Front" cluster is visually closer to "Front" than "Right" is to "Front". Furthermore, artificial noise signals were added to the original kinematic data, which were incrementally increased in

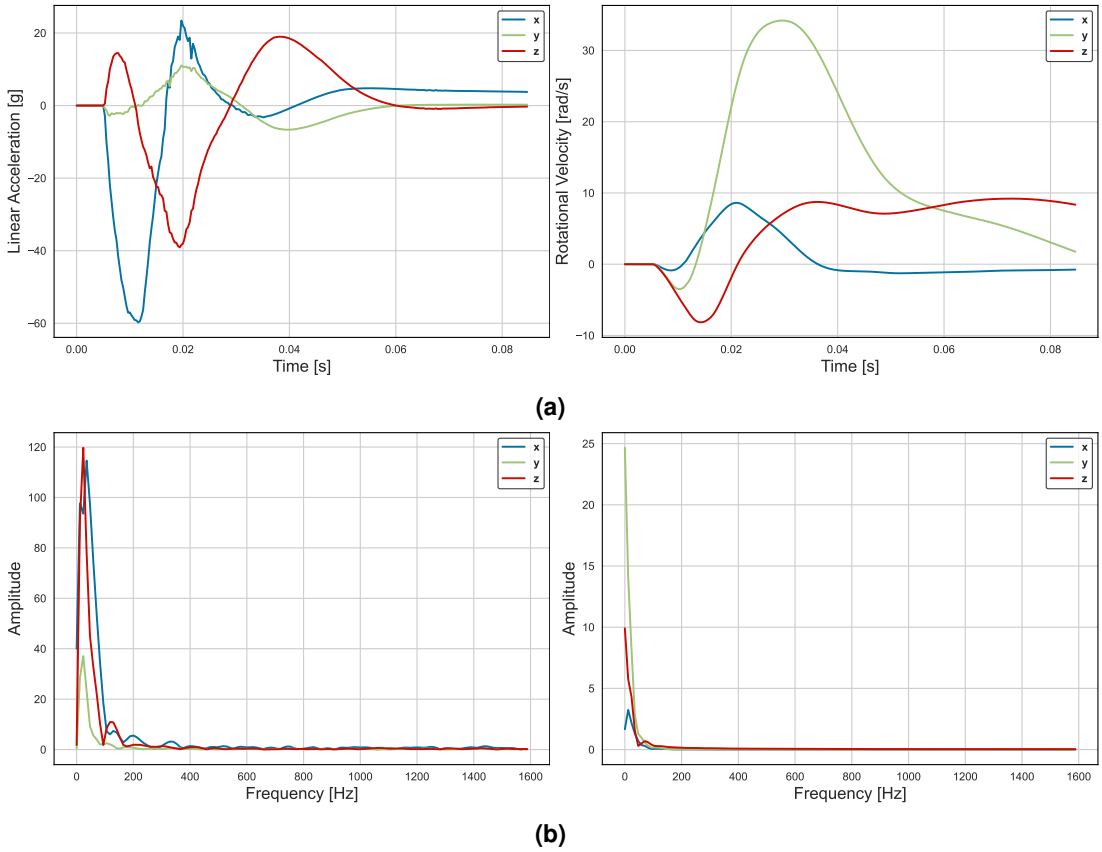

Figure 4.5: (a) Example of kinematics (linear acceleration and rotational velocity components) obtained from the LS-DYNA simulation and (b) its corresponding fast Fourier transform.

magnitude to evaluate the performance of the methodology at different levels. By introducing noise signals, the methodology was tested to see if the features data sets would be able to classify live impact kinematic data that will house varying levels of unwanted disturbances ('Noise'). Noise signals were randomly generated with a mean value of 0, and standard deviation increasing from 0.2 to 1 in increments of 0.2, providing 5 noise levels to test with. An example of the variation in noise signal generated between the highest SD and lowest SD setting can be seen in . The performance of features data set with K-means was evaluated by analysing the classification rate at each level of noise and therefore help to understand which features data set was the most robust. As seen in Figure 4.5 (see also Section 4.4.1), linear accelerations obtained from the LS-DYNA numerical simulations consisted of unwanted disturbance whereas the rotational velocity components were smooth. Therefore, artificial noise signal data points, like the ones seen in Figure 4.6, were added to the rotational velocity data points while testing K-means clustering, to better replicate live data via an instrumented mouthguard that produces signals with unwanted disturbances. Comparison between Figures 4.5 and 4.7 highlights how the addition of the random generated noise altered the original rotational velocity components obtained from the LS-DYNA simulations.

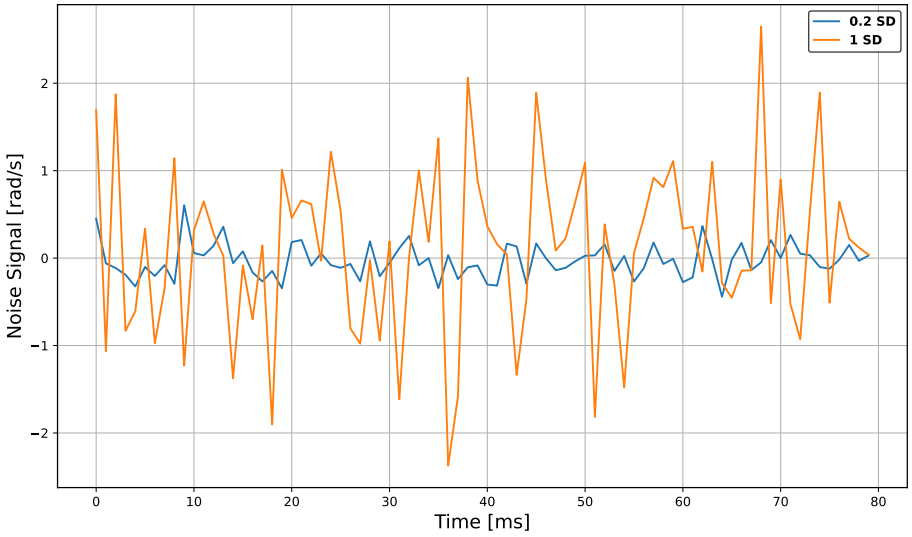

Figure 4.6: Example noise signals for the highest and lowest standard deviation used within this research.

The impacts between zones provided a good test of the C-means clustering ability to outline overlapping data. Membership values assigned for those impacts was used as a method to test the performance of C-means clustering for different features data sets. Moreover, an additional 5 impact simulations were conducted from varying locations to create a test data set which was used to test C-means ability to classify new data points. A small sample size was chosen to understand if the predict function is a feasible classification method, with the locations of the 5 impacts highlighted in Figure 4.3. The membership values provided from the algorithm via the predict function, was analysed to test the performance of the algorithm as a classifier.

4.3 Results

4.3.1 Kinematic Output

The LS-DYNA simulations were conducted to provide a kinematic data set of varying impact magnitudes at differing locations. Table 4.2 lists the mean linear acceleration and mean impact duration for impacts within each zone, showing that the results from the simulations are within the ranges seen within contact sports. Additionally, the standard deviations in Table 4.2 highlight the variation within the impact magnitude for each region, ensuring that the clustering methodology is being tested for a varied data set. Examples of the kinematic output from the simulations for each region can be visualised in figures in Appendix A.

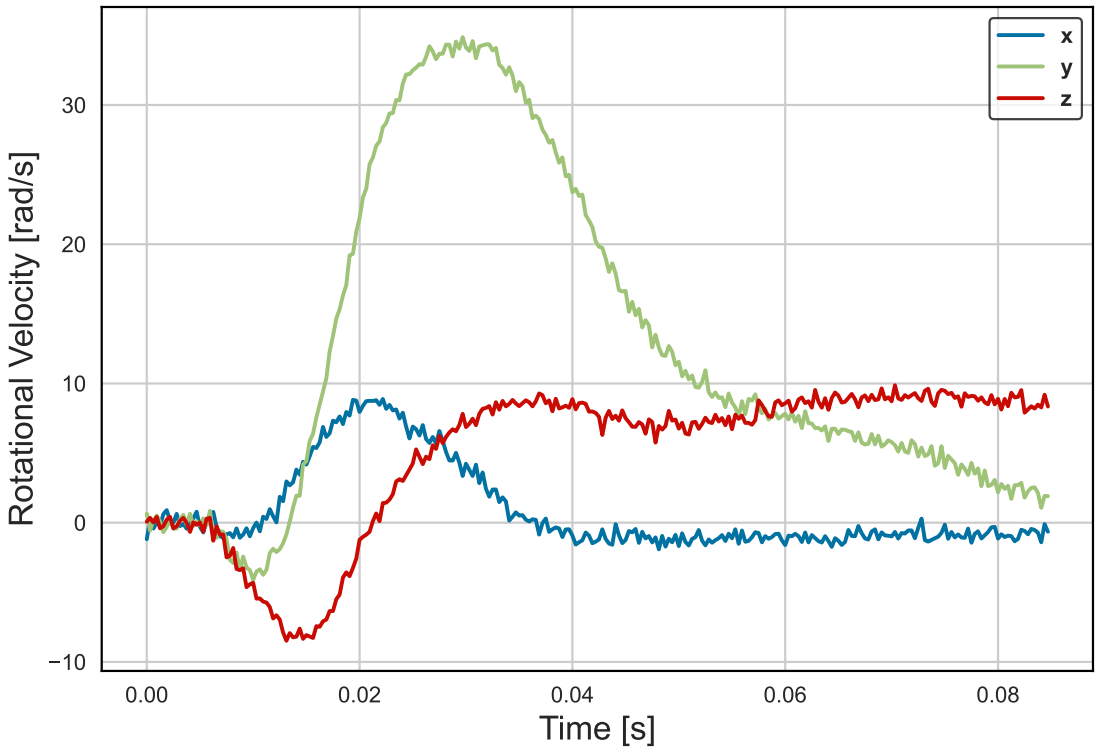

Figure 4.7: Rotational velocity signals with randomly generated noise signal added.

4.3.2 K-Means Clustering

K-Means clustering was used for the three stated feature data sets, which incorporated all 52 impact simulations. The simulations were conducted from 6 zones on the head, meaning that K-Means setup was for the algorithm to establish 6 clusters. The performance of K-Means clustering was initially measured by establishing the classification rate for each feature data set, which was determined by analysing if the algorithm successfully clustered together impacts within the same zone. Furthermore, the impacts located between zones, are said to have been accurately classified if the algorithm assigns them to either of the impact region clusters it is in between. Features data sets 2 and 3, incorporating displacements and FFT amplitudes, provided a 100% classification rate whereas FD1, which housed displacements

Table 4.2: Kinematic output from the finite element numerical simulations.

Region	Mean PLA (g)		Mean Duration (ms)	
	a	SD	t	SD
Front	49.1	16.4	10.9	0.5
Right Front	16	8	9.8	0.4
Right	14	6.1	12.1	0.6
Right Lower	53.6	22	9.6	0.3
Left Front	43	17.6	9.5	0.2
Left	27	14	9.8	0.6

only, misclassified impacts. The misclassification seen within the FD1 occurred from impacts being clustered to a neighbouring zone rather than the zone it should be assigned to. Additionally, two clusters were merged together, which led to the splitting of an established cluster zone into two elsewhere. Although this still provided 6 clusters, the data wasn't split within the desired impact regions making it not fit for purpose.

To visualise the clusters for the three feature data sets, PCA was utilised as it is able to display the features within two axes, while still incorporating majority of the data set. Figure 4.8 highlights the PCA plots for the three approaches, showcasing the 6 user-defined clusters from K-Means clustering. It is evident from looking at Figure 4.8, that the data sets that include FFT features, FD2 and FD3, provide differing cluster shapes to FD1. Additionally, it is noticeable from FD2 and FD3, in Figures 4.8b and 4.8c, that the "Right Low" and "Right" impact zones are close in proximity but the features data sets are able to differentiate between them. However, FD1 in Figure 4.8a shows one "Right" cluster having merged the two together. Additionally, FD1 split the "Front" cluster into two as discussed earlier, which can also be visualised in Figure 4.8a, further highlighting why FD1 was deemed unfit for purpose.

Further analysis of the K-Means algorithm was conducted to test the performance of the clustering when the desired number of the clusters was altered from the predefined 6. The algorithm was conducted with K =3 and K =5 for FD2, with the results visible in the corresponding PCA plots in Figure 4.9. The output highlights the ability of K-Means to determine the number of clusters in a logical sense, merging two of the "Right Front" impacts, all of the "Right Low" and "Right" into one cluster, as well as "Left Front" and "Left" into another, creating the desired three cluster output. For $K = 5$, the algorithm merged "Right Low" and "Right" into just a "Right" cluster, as shown in Figure 4.9b. This highlighted the flexibility of the clustering algorithm as it has the ability to calculate different number of clusters within the same data set. This is extremely useful as it has the capability to determine fewer number of clusters with larger impact zones, or smaller impact zones with more clusters, depending on the desired output.

4.3.3 Noise Analysis

As stated in Section 4.2.4, randomly generated noise signals were added to the rotational velocity components to test the clustering algorithm's ability to classify the results for the stated three feature data sets. Added noise signals were varied between components as well as between different impacts, creating the desired noise randomness between impacts that may be seen within live impact kinematic data acquired from an instrumented mouthguard. The displacement-only approach, FD1, performed even more poorly with the addition of noise signals with even more impacts being assigned to different clusters than intended, whereas both approaches that utilised FFT and Displacement, FD2 and FD3, classified 100% of the

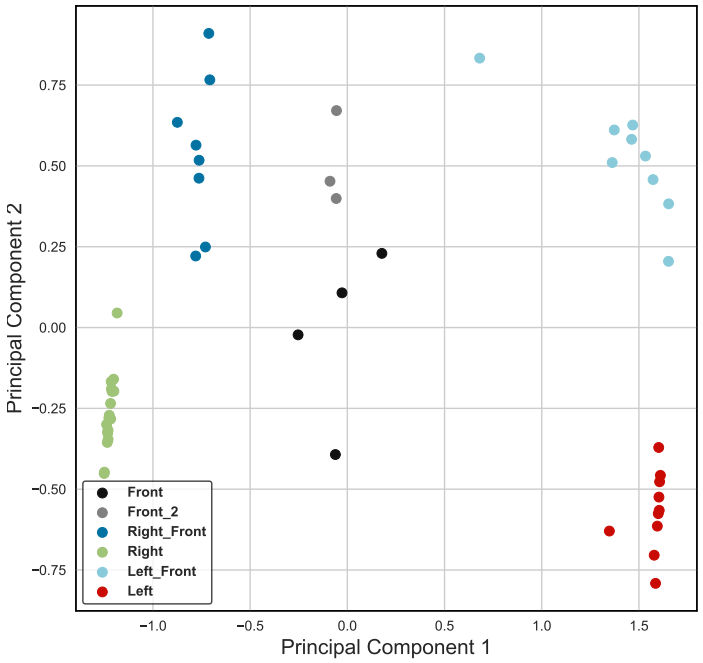

(a)

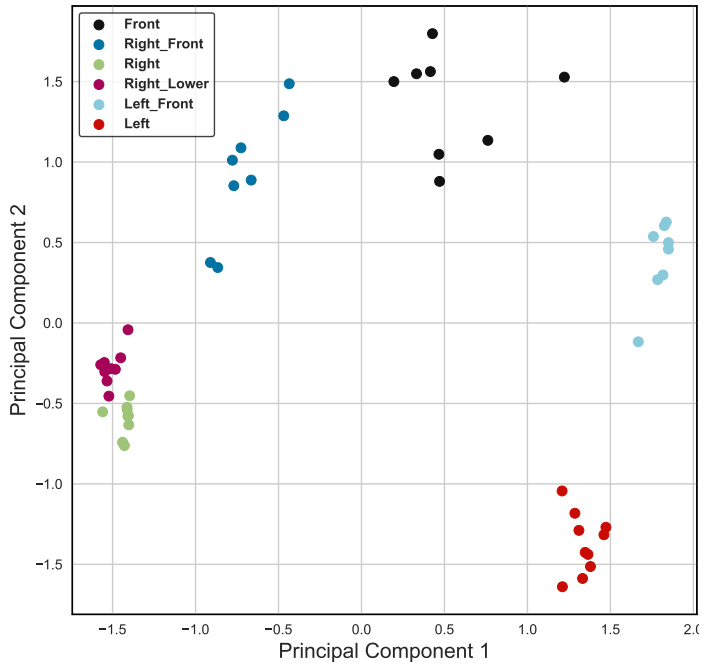

(b)

Figure 4.8: PC plots highlighting K-Means established 6 clusters for feature data sets: (a) displacement, (b) displacement + FFT, and (c) displacement + FFT Optimised.

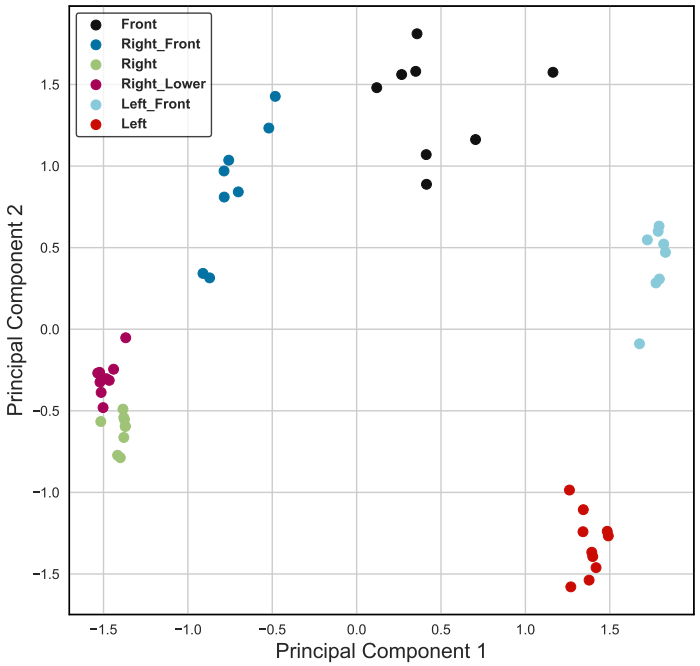

(c)

Figure 4.8: PC plots highlighting K-Means established 6 clusters for feature data sets: (a) displacement, (b) displacement + FFT, and (c) displacement + FFT Optimised. (cont.)

impacts correctly for all noise levels. The only difference seen between FD2 and FD3 was within the classification of impacts that occurred between two zones, as the two approaches assigned 2 of the impacts between zones to differing clusters after the addition of noise signals.

4.3.4 C-Means Clustering

C-Means clustering was chosen as a method to better understand overlapping data sets as its a soft clustering method. With impacts occurring between zones, hard clustering may not provide as much insight as soft clustering, which can distinguish between impacts that would be labelled within the same hard cluster. Four impacts between zones were simulated, 2 between the "Right", the "Right Low" and the "Right Front", and two between the "Left" and the "Left Front" zones. These four impacts were utilised to test C-means clustering ability to represent overlapping data, as the algorithm provides a membership value of each data point to the different clusters. Table 4.3 lists the cluster membership values assigned by the algorithm represented as a percentage, while utilising FD2 and FD3, to analyse which approach provided the most accurate representation of the conducted impact. From observation of the LS-DYNA simulation, Right 1 was an impact conducted in between the zones "Right", "Right Low" and "Right Front", with a focus of the impact being closer to the "Right" region on

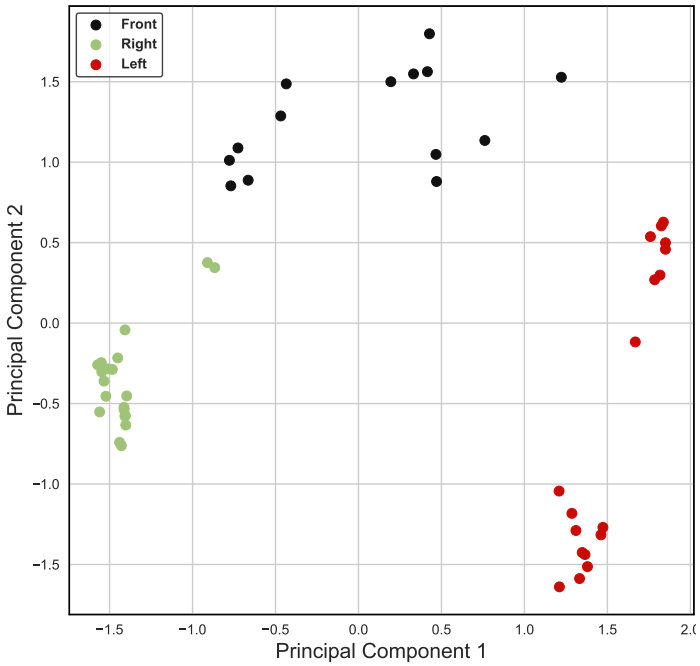

(a)

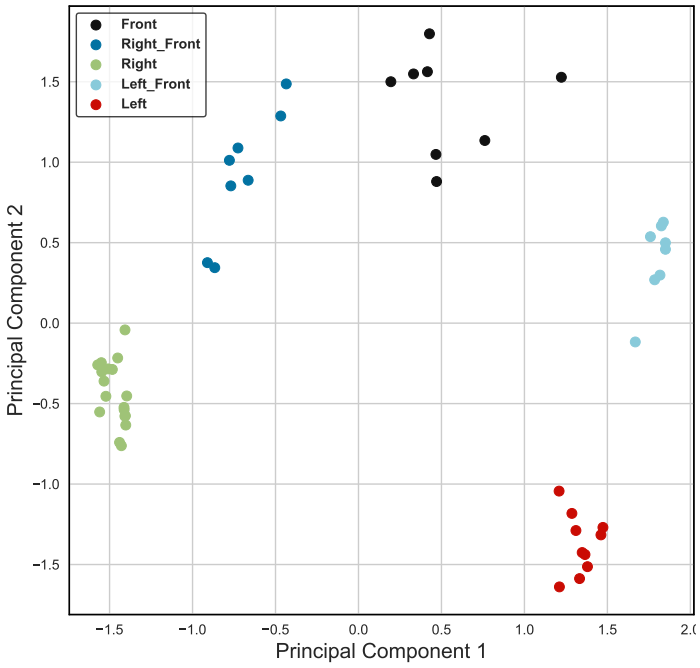

(b)

Figure 4.9: PC plots for Displacement + FFT feature data set showing: (a) 3 clusters established by K-Means clustering, and (b) 5 clusters established by K-Means clustering.

the Hybrid III Dummy head, whereas the Right 2 impact was conducted closer to the "Right Low" zone. This was accurately represented by both features data sets (FD2 and FD3) as seen in Table 4.3. Additionally, the Left 1 impact was conducted between the "Left" and "Left Front" zones, with Left 1 closer to the "Left" zone than Left 2, which was also accurately represented by the membership values assigned.

Table 4.3: Impact membership percentage values assigned to each cluster from the C-means algorithm utilising features data sets: displacements (FD1), displacements + FFT (FD2) and displacement + optimised FFT (FD3).

Region	**Right 1**		**Right 2**		**Left 1**		**Left 2**	
	FD2	FD3	FD2	FD3	FD2	FD3	FD2	FD3
Front	2	2	4	5	6	7	8	8
Right Front	5	5	15	17	4	6	8	9
Right	55	53	26	27	5	5	8	8
Right Low	34	36	49	44	6	5	7	8
Left Front	2	2	3	3	13	12	20	19
Left	2	2	3	4	66	65	49	48

Furthermore, C-Means was used with the FD3 approach to test the ability of soft clustering to be used as a classifier of new impacts. The algorithm uses existing cluster centers and establishes the distance of new data samples to the centers in order to identify the membership to existing clusters, hence classifying the new data samples. Five test impacts were simulated on different regions of the Hybrid III Dummy head, with one located in the "Front", two "Right", one "Left Front" and one "Left" impact regions as visualised in Figure 4.3. Table 4.4 lists the output from the algorithm, showcasing the ability of the C-Means algorithm to establish membership values that correlate to the region of the head where the impact occurred for the conducted simulations. The cluster with the highest membership value can be utilised as the cluster the new data sample belongs to, therefore classifying new data. Using this approach, all five tests were classified correctly as the cluster with the highest membership correlated to the region on the Hybrid III Dummy where the impact occurred. Additionally, Test 4 in Table 4.4 was conducted between impact zones to analyse the ability of the algorithm to classify overlapping data samples by identifying which clusters the impact overlaps with. The membership values assigned for the "Right" and "Right Lower" cluster were 68$\%$ and 21$\%$, correctly highlighting the impact location between the two zones but leaning more towards the "Right" zone. This provided confirmation that new data points can be analysed further to provide a better understanding of the location of the impact, especially ones that may fall between a few clusters, rather than classifying the impact to the cluster with the highest membership value.

Table 4.4: Membership percentage values assigned to each cluster from C-Means Predict for each impact, using FD2.

Region	Test 1	Test 2	Test 3	Test 4	Test 5
Front	16	66	1	2	5
Right Front	11	9	2	5	4
Right	5	5	87	68	4
Right Lower	5	6	8	21	3
Left Front	53	8	1	2	9
Left	10	6	1	2	75

4.4 Discussion

4.4.1 Kinematic Output

The research in this chapter was conducted to develop a method to create synthetic kinematic data that replicated signals obtained from an instrumented mouthguard to aid and test a new methodology to determine impact locations. The research used Biocores validated Hybrid III Dummy head FE model (LS-DYNA) to generate synthetic kinematic data that replicated on-field impact durations and magnitudes within contact sport. The use of the numerical model provided the desired kinematics. This methodology is, however, not able to replicate the complete level of variation seen within live impacts, such as double impacts where a player gets a primary impact followed closely by a secondary one from a different direction, among others.

Additionally, noise levels seen within kinematic data sets from live impacts are difficult to replicate, as players are constantly moving pre- and post-impact. The example synthetic kinematic data set shown in Appendix A highlights the level of noise within the linear acceleration and rotational velocity components obtained from the numerical simulations. Although linear acceleration components from the simulations included disturbances in the signal, the rotational velocities were found to be smooth with little to no disturbances, which may not replicate live impact data obtained from an instrumented mouthguard. To address this, artificial noise signals were added to the rotational velocity components, while testing the methodology, to establish if the clustering algorithms are able to classify impacts accurately. Furthermore, the unwanted disturbances seen within the linear acceleration data in Appendix A may not correlate to the ones seen within live impacts.

Nevertheless, the work described in this chapter provided a synthetic kinematic data set that replicated impact kinematics seen within contact sport, on a range of different impact locations. The varied data set allowed for the impact location methodology to be rigorously tested in order to understand its suitability.

4.4.2 Feature Selection

Three features data sets were utilised for the clustering algorithms, as described in Section 4.2, with the impact classification rates analysed in Section 4.3. FD1 included only displacements and was found to be the worst performing approach with regards to classification rate, more evidently when noise signals were added to the original kinematic data. This is due to the noise signals directly impacting the proportionality between the components of the kinematic data as they are integrated, which drives the distance-based clustering algorithm, hence resulting in the algorithm miss-classifying impacts to neighbouring clusters. Although FD2 and FD3 also incorporated displacement components, they proved to perform better than FD1 as the majority of the features in those data sets were FFT amplitudes. As noise signals were represented in the frequency domain as low amplitudes at high frequencies, the lower frequency amplitudes, which are deemed to drive the distance based clustering algorithm as impact kinematic signals are low frequency signals, were unaffected. The results show this as both FFT-based feature data sets provided a 100% classification rate at every noise level.

The FD1 approach also provided illogical cluster formation, as discussed in Section 4.3 and highlighted in Figure 4.8a. It is hypothesised that this may be due to the effect of noise within the linear acceleration signal, which altered the proportionality between components during the signals double integration to convert the acceleration signals to linear displacements. Additionally, rotational displacement values do not represent the entire impact signal, as the displacement values are taken when the contact between the impactor and head has finished, therefore not including any post-impact rotational velocity signal within FD1. FD2 and FD3, however, were able to incorporate the entire signal within the frequency domain including post-impact, which enables a clearer distinction between clusters and therefore provide a better representation of the impact location, as seen in Table 4.3.

Furthermore, their was little to no difference between FD2 and FD3s clustering output as seen in Section 4.3, highlighting that reducing features to only incorporate lower frequency amplitudes within the features data set doesn't hamper performance of the output. Therefore, it is deemed that the FD3 is the most fit for purpose features data set.

4.4.3 Performance Testing

The proposed methodology that uses unsupervised learning methods to classify impacts, performed well compared to research that has been conducted (Bartsch et al., 2014; Kuo et al., 2018). Existing research has focused on using peak linear acceleration components to approximate a direction of impact and hence the region the impact occurred in, which has been deemed an inaccurate method (Kuo et al., 2018). Additionally, the research conducted by Kuo et al. (2018) used displacement components but was only able to classify 37% of the impacts to the correct region. The clustering method proposed in this research, utilising a feature data set that houses displacements and optimised FFT, is able to improve upon this

with a classification rate of 100% for the 52 conducted simulations. The methodology clusters together impacts with similar features, for a user-defined number of clusters with the region each cluster is assigned to being established by video verification of one impact within each cluster. Additionally, the use of C-Means clustering highlights the capability of understanding overlapping data sets, providing more insight to impact locations within each cluster, rather than assigning each impact to a hard cluster. Furthermore, C-Means highlighted the ability of clustering algorithms to be used as classifiers for new data, as the 5 new impact data points were assigned to the correct clusters. With traditional classifiers, such as neural networks, requiring high volume of data to train the network before it is capable of classifying impacts, the ability of clustering classifiers can be extremely useful as large amounts of impact data from various impact zones is not readily available.

One limitation of using clustering algorithms is the determination of the correct number of clusters that the algorithm is splitting the data into. For this research, impacts were conducted within 6 regions of the head ($K = C =$6), for which the algorithm classified 100% of impacts correctly. However, for an unseen data set, correctly guessing the values of K and C may prove difficult. The Elbow method for K-Means and the Fuzzy Partition Coefficent (FPC) for C-Means can be used to select the most efficient values of K and C for each specific data set, allowing the hard or soft clustering algorithms to split the data set in an optimal fashion.

Additionally, another potential limitation of using clustering algorithms is the requirement of video footage to verify the regions each cluster is associated with. The algorithms will provide the specified number of clusters as its output, however determining the impact region assigned to a cluster will require one data sample per cluster to be video verified. Video verification is a major part of determining impact regions currently within contact sports, therefore using video to define the clusters should not be an issue.

Nevertheless, clustering algorithms show great promise in determining impact regions with kinematic signals, similar to one obtained from instrumented mouthguards. The clustering algorithms can be used on large data sets, such as those encompassing an entire season, to establish hard or soft clusters that will require video verification of one data point per cluster. Additionally, a small verified impact data set, similar to the one used in this research, could be used to establish cluster centers replicating regions of the head researchers want to classify impacts to. C-Means can then be used to classify new data to specific regions, based of the cluster with highest membership value, as stated in Section 4.3. This provides the most promising results in classifying impacts to specific regions, and could be implemented with existing instrumented mouthguard technologies. Furthermore, the computational cost of running K-Means clustering algorithm with the entire 52 impact data set was found to be 3 seconds with 0.4 seconds required to classify one impact using C-Means predict function. This in comparison to 17 seconds required to determine one impacts location using the IMLA confirms the hypothesis that the clustering methodology reduces computational costs.

4.5 Conclusion

The research described in this chapter proposed, implemented and tested a different method to determine the impact location on the head to aid ongoing research in contact sports, utilising unsupervised learning clustering algorithms with features data sets housing features from synthetic head impact kinematic signals. 52 numerical simulations were conducted on multiple regions of the head, providing impact magnitudes and durations that closely replicate those reported within contact sports in existing research (D. King et al., 2015; Tooby et al., 2022). Mean peak resultant linear accelerations in the range of 14g to 53.6g were observed for the six impact regions defined. Three features data sets utilising combinations of linear and rotational position values, established by mathematical integration of linear acceleration and rotational velocity signals, and Fast Fourier Transform (FFT) of the kinematic signals, were used with K-Means and Fuzzy C-Means clustering algorithms. Additionally, the C-Means algorithm was tested as a potential classifier of new data, by using the predict function within the algorithm.

Two features data sets (FD2 and FD3) housing a combination of displacement and FFT were found to perform better than the features data set (FD1) housing displacements only with clustering algorithms. FD2 and FD3 clustered together 100% of the impacts within the correct region, even after artificial noise signals were added to the synthetic kinematic signals to replicate unwanted disturbances observed in live impact data gathering. FD1, however, misclassified impacts as well as creating unwanted cluster groups. Additionally, C-Means clustering was used to determine impacts within zones, for which FD2 and FD3 were found to provide accurate results, in replicating the impact location. Furthermore, 100% of new impacts were successfully classified using the C-Means predict function, highlighting the potential for clustering algorithms to be used as a classifiers of new data. Although further testing is required with live impact data collected from instrumented mouthguards, the use of clustering algorithms with features data sets housing displacement and FFT of kinematic signals has the potential to determine head impact locations and aid the ongoing battle against mTBI in contact sports.

Chapter 5

Closing Remarks

5.1 Conclusion

The research conducted in this Thesis was multifaceted and was designed to understand head impacts sustained within non-helmeted contact sports. The research focused on conducting a feasibility study for a new instrumented mouthguard device developed by Force Impact Technologies, as well as the analysis of instrumented mouthguard kinematic data to determine the location of head impacts in an attempt to aid the clinical understanding of concussion within contact sport.

Force Impact Technologies introduced a new instrumented mouthguard aimed at identifying head kinematics during and after impacts in contact sports. Since the mouthguard had only undergone lab testing, a feasibility and validity study was performed to assess its suitability for professional sports by analysing the comfort and fit of the device, the on-field kinematic data, and the overall usability of the system and working closely with Edinburgh Rugby professional team. The feasibility study found the mouthguard performed similar to existing devices in industry with regards to comfort and fit, and performed well with regards to the usability of the system. However, FIT's mouthguard needs significant further development before it can be considered suitable for professional contact sports due to the poor performance with on field kinematic data testing. The on-field kinematics require more rigorous testing to enhance the quality of the output, along with implementing the changes recommended in this study.

Additionally, a key aim of the conducted research was to establish a method to determine head impact location from kinematic data obtained via an instrumented mouthguard. Two methodologies were proposed to achieve this, with one using rigid body dynamics coupled with a multi-degree of freedom (MDOF) lumped mass system to determine the impact location and approximated force magnitudes, and the other utilising machine learning clustering algorithms to determine the impact region on the head. The rigid body methodology, labeled in this research as the Impact Magnitude and Location Algoruthm (IMLA), was tested with kinematic data obtained from a lab test using an instrumented mouthguard and five impact

simulations conducted on a Hybrid III Dummy Finite Element model, with the algorithms output compared to the location of the impacts within the simulations/lab test. The methodology performed well, with the impact location determined by the algorithm being within 12 mm of the impact center for all conducted tests.

The clustering methodology utilised K-Means and Fuzzy C-Means clustering algorithms with features data sets housing features from kinematic data. In order to test out the clustering methodology, a synthetic data set was created by using a Hybrid III Dummy Finite Element head model with a bespoke impactor created with layers to represent the scalp, the skull and the mass of the impactor. 52 impacts were simulated on 6 different impact regions on the head, generating linear acceleration and rotational velocity components to replicate instrumented mouthguard kinematic data. Features data sets with a combination of linear and rotational position values, and Fast Fourier Transform (FFT) of linear acceleration and rotation velocity components provided the best results with K-Means clustering algorithm, as 100$\%$ of impacts simulated within the same region were correctly grouped together. Additionally, this features data set provided good representation of impacts between regions when utilised with Fuzzy C-Means soft clustering algorithm as well as correctly classifying 100$\%$ of new data, while testing Fuzzy C-Means algorithms capabilities as a potential classifier of new data samples.

The main limitation of both methodologies was the inability to test them with live instrumented mouthguard impact kinematic data. The use of synthetic data sets via FE models and laboratory tests provided impacts that replicate the desired kinematics with regards to duration and magnitude. These were, however, unable to replicate scenarios seen in live match play such as double impacts and unwanted disturbances from player motion, which could affect the output from the IMLA. Additionally, the IMLA requires accurate head dimensions for each player in order to utilise the rigid body dynamics methodology, which may not be feasible. Furthermore, the MDOF developed for the IMLA was a simplified representation of the complex human head and neck system, using intervertebral stiffness in three linear directions. This resulted in the impact force values to be underestimated by 60%. Due to the double pivot nature of the human head and neck system, the underestimated nature of the approximated force did not hinder the output from the IMLA for the conducted tests. However, during further testing with live data this could potentially hinder the algorithms output. The clustering methodology provided a more robust method, however limitations within include the inability to determine the number of clusters required for an unseen data set, as well as the requirement to video verify one impact per cluster to assign said cluster to a head region. Nevertheless, both methodologies proposed and developed in this research have strong potential to significantly aid the the work conducted to understand concussion in contact sport.

5.2 Future Work

Future work predominantly should focus on testing the impact location methodologies stated in this research with live impact data as this was not possible for the duration of this study. This would require, raw kinematic data obtained from mouthguards used with both methodologies to understand if the impact locations provide accurate results.

Additionally, this research utilised a simple MDOF to replicate the human head and neck. Additional future research should focus on using the methodology proposed within the MDOF, adding elastic components to more accurately replicate neck muscles. This could potentially be a useful method to understand the relationship between neck strength and head motion alongside understanding impact force magnitudes. Minimal muscle stiffness values are stated in conducted research, with some research stating one stiffness value per muscle rather than a 6×6 stiffness matrix including linear and rotational coupling force values, as seen for the intervertrebal disks (Luo & Goldsmith, 1991). Understanding the muscle stiffness couples would allow the MDOF to be a more accurate representation than the one utilised within this research of the human head neck system. The human head and neck system is very complex, which may mean achieving complete accuracy using the MDOF approach could be challenging.

Appendix A

IMLA

A.1 Implemented Code

```
NodesData = table2array(readtable('nodes1.xlsx')); %Load head model
    nodes
%%
M = 4.5;                        %Mass of head
I1=12300e-6;                    %Moment of Inertia
I2=15400e-6;
I3=11500e-6;

D_R = [98-64;3.86;717-691]*10^-3;       %distance to rotation point from
     CoG
Iy = I1+ M*((D_R(2,1))^2+(D_R(3,1))^2);
Iz = I2+ M*((D_R(1,1))^2+(D_R(3,1))^2);
Ix = I3+ M*((D_R(1,1))^2+(D_R(2,1))^2);

%% Acceleremoter Data  -  Linear Accel
D = table2array(readtable('highglin.csv'));
t_lin  = (D(:,2)-D(1,2));
lina = D(:,3:5)*9.81*196/1000;
[val,row] = max(lina(:,2));
maxlin = transpose(lina(row,1:3));
maxt = t_lin(row,1);

%% Acceleremoter Data  -  Rotational Velocity
Data = table2array(readtable('gyroimpac-data.csv'));
t = Data(:,6);

vX = Data(:,7);
vY = Data(:,8);
vZ = Data(:,9);

rot_v = [vX,vY,vZ]*(pi/180);
%% Angular Acceleration

ax=diff(rot_v(:,1))./diff(t);
ay=diff(rot_v(:,2))./diff(t);
```

```
az=diff(rot_v(:,3))./diff(t);

ra = [aX,aY,aZ];

%% Linear Acceleration at CoG
for i =8:1:24
[~,ans] = (min(abs(t - t_lin(i,1))));
rota(:,i-7) = transpose(ra(ans,1:3));
rotv(:,i-7) = transpose(rot_v(ans,1:3));

r = ([0;42.619091;-87.202049]*10^-3);
aCog(:,i-7)= transpose(lina(i,:)) + cross(rota(:,i-7), r)+(cross(rotv(:,
    i-7), (cross(rotv(:,i-7),r))))

Mx = (Ix*rota(1,i-7))+((Iz-Iy)*rotv(2,i-7)*rotv(3,i-7));
My = (Iy*rota(2,i-7))+((Ix-Iz)*rotv(1,i-7)*rotv(3,i-7));
Mz = (Iz*rota(3,i-7))+((Iy-Ix)*rotv(2,i-7)*rotv(1,i-7));
Ms(:,i-7) = [Mx;My;Mz];
end
```

Listing A.1: Establishing Eulers Moments and linear acceleration at CoG

```

vCOG = cumtrapz(t_lin,aCOG);
xCOG = cumtrapz(t_lin,vCOG);
%%
k = [122,0,0;
     0,390,25;
     0,25,140]*10^3;
ratio = [1.56;0.5;0.64;0.92];
m = [3.5;0.312;0.312;0.361];

  Mat = [M_a,M_a,M_a,m(2,1),m(2,1),m(2,1),m(3,1),m(3,1),m(3,1),m(4,1),m
    (4,1),m(4,1)];
M = diag(Mat);
k1 = ratio(1,1)*k;
k2 = ratio(2,1)*k;
k3 = ratio(3,1)*k;
k4 = ratio(4,1)*k;
%%
K = zeros(12);
K(1:3, 1:3) = k1;
K(1:3, 4:6) = -k1;
K(1:3, 7:9) = 0;
K(1:3, 10:12) = 0;
K(4:6, 1:3) = -k1;
K(4:6, 4:6) = k1+k2;
K(4:6, 7:9) = -k2;
K(4:6, 10:12) = 0;
```

```
K(7:9, 1:3) = 0;
K(7:9, 4:6) = -k2;
K(7:9, 7:9) = k3+k2;
K(7:9, 10:12) = -k3;
K(10:12, 1:3) = 0;
K(10:12, 4:6) = 0;
K(10:12, 7:9) = -k3;
K(10:12, 10:12) = k3+k4;

cor = M^(-1)*K

[Mod1, Eigs1] = eig(cor);
%%
syms x7 x8 x9 x10 x11 x12 Fx Fy Fz x4 x5 x6
 F = [Fx;Fy;Fz;0;0;0;0;0;0;0;0;0];
for j = 1:1:11
MM = transpose(Mod1)*M*Mod1;
MK = transpose(Mod1)*K*Mod1;
Q = transpose(Mod1)*F;
w =sqrt(Eigs1);
for i = 1:1:12
 q(i,1) = ((Q(i,1)/w(i,i))*(1-cos(w(i,i)*t_lin(j))))/w(i,i);
end
  x = transpose([(xCOG(j,2)),(xCOG(j,3)),(xCOG(j,1)),x4,x5,x6, x7, x8,
    x9, x10, x11, x12]);
eqn = Mod1*q == x;
sol = solve(eqn,[x4,x5,x6, x7, x8, x9, x10, x11, x12, Fx, Fy, Fz]);
fs(j,:) =  (double([sol.Fx, sol.Fy, sol.Fz]))

end
```

Listing A.2: Using MDOF to find approximated force magnitudes

```

Fx = -188;
Fy = 215;
Fz = -660;

F = [Fx;Fy;Fz];
%%
l=0
 for i =1:1:4002
 rax = NodesData2(i,3)*10^-3 - 0.0039;
 ray = NodesData2(i,4)*10^-3 - 0.691;
 raz = NodesData2(i,2)*10^-3 - 0.0640 ;
r_m = [rax;ray;raz];
Mu(:,i) = cross(r_m,F);
c(:,i) = sign(Ms(1,6))==sign(Mu(1,i)) && sign(Ms(2,6))==sign(Mu(2,i)) &&
     sign(Ms(3,6))==sign(Mu(3,i));
```

```
16
17      x1(1,i) =(Mu(1,i) - Ms(1,6));
18      x1(2,i) = (Mu(2,i) - Ms(2,6));
19      x1(3,i) = (Mu(3,i) - Ms(3,6));
20
21      %%
22
23 if x1(1,i) > -6 && x1(1,i) < 6 && x1(2,i) > -10 && x1(2,i) < 10 && x1(3,
       i) > -13.1 && x1(3,i) < 15 && c(1,i)==1 && raz>0
24 l=l+1
25     M_diff(1,l) = x1(1,i);
26     M_diff(2,l) = x1(2,i);
27     M_diff(3,l) = x1(3,i);
28     o(1,l) = (i);
29     R(1,l) = rax;
30     R(2,l) = ray;
31     R(3,l) =raz;
32 else
33
34 end
35  end
36  %% Visualise Impact Location
37  [row,col] = size(R)
38 scatter3(Data2(:,2),Data2(:,3),Data2(:,4),5,[0.8500 0.3250 0.0980], '
       filled')
39 hold on
40 for i=1:1:col
41 scatter3(Data2(o(1,i),2),Data2(o(1,i),3),Data2(o(1,i),4),250,'k','filled
       ')
42 hold on
43 end
44 hold off
45 grid off
46  xlim([-50 250])
47  ylim([-150 150])
```

Listing A.3: Moment matching to determine the impact location

A.2 Kinematic Output

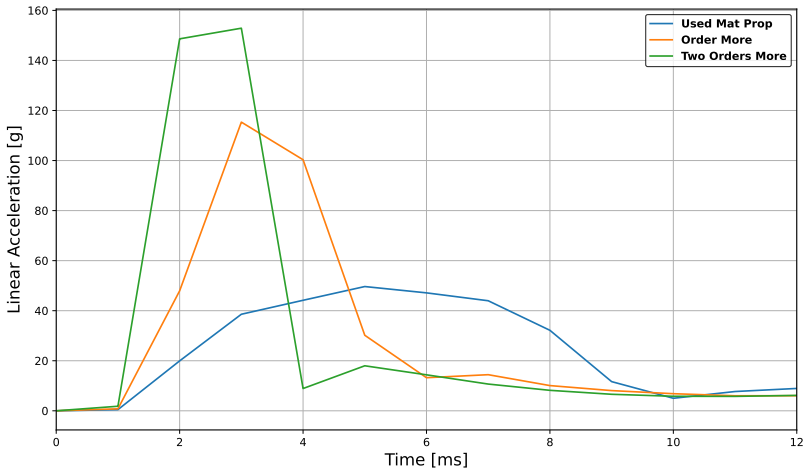

Figure A.1: Impact kinematics showing the impactor iteration process, showcasing the resultant linear acceleration obtained from three impactor softness settings.

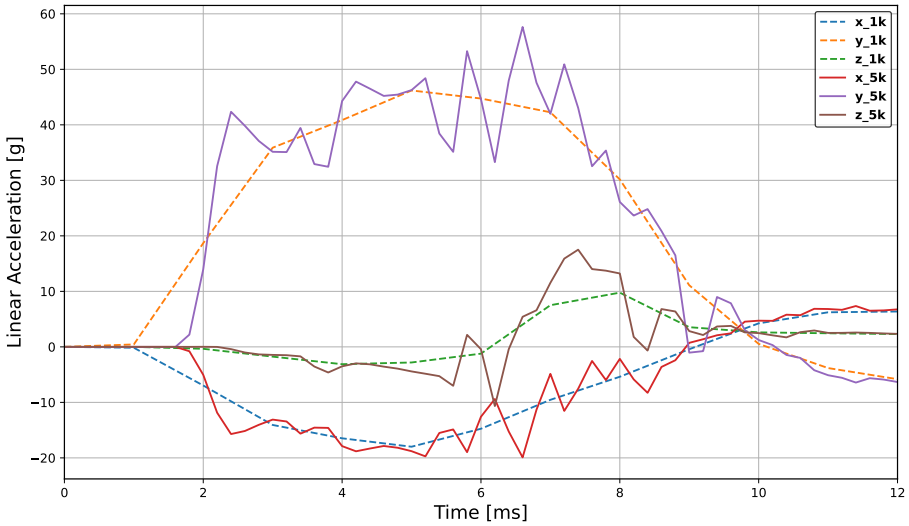

Figure A.2: Impact kinematics for Hybrid III dummy impact, showcasing the linear acceleration components obtained at 1000Hz and 5000Hz sampling rates.

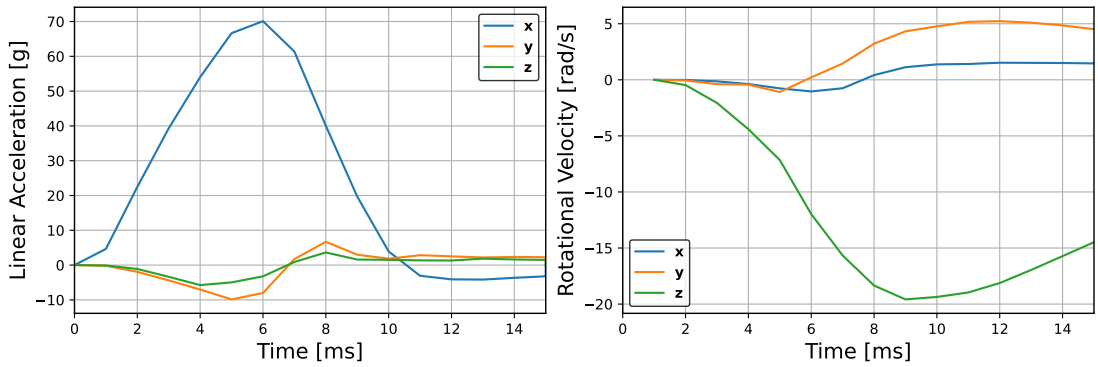

Figure A.3: Impact kinematics for a side impact, showcasing the linear acceleration and rotational velocity components

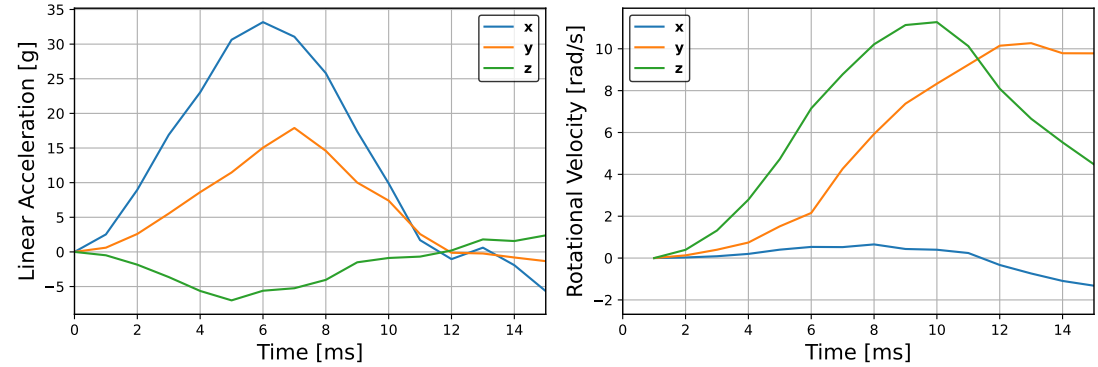

Figure A.4: Impact kinematics for a right low impact, showcasing the linear acceleration and rotational velocity components

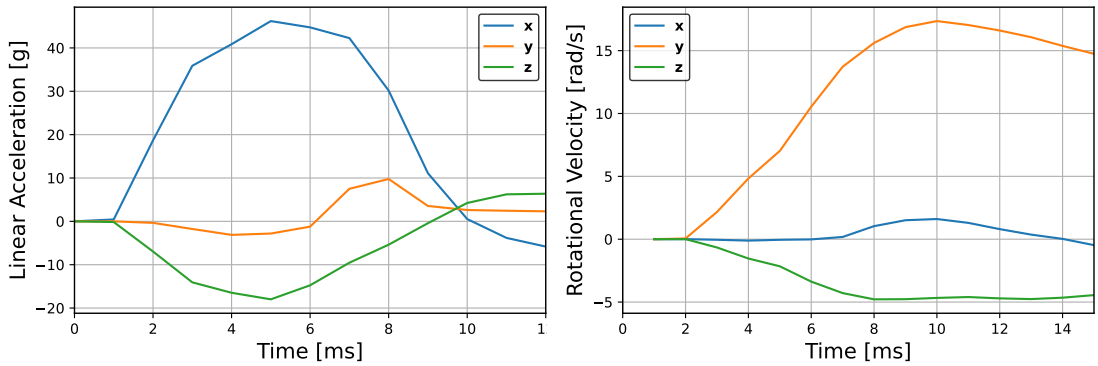

Figure A.5: Impact kinematics for a right front impact, showcasing the linear acceleration and rotational velocity components

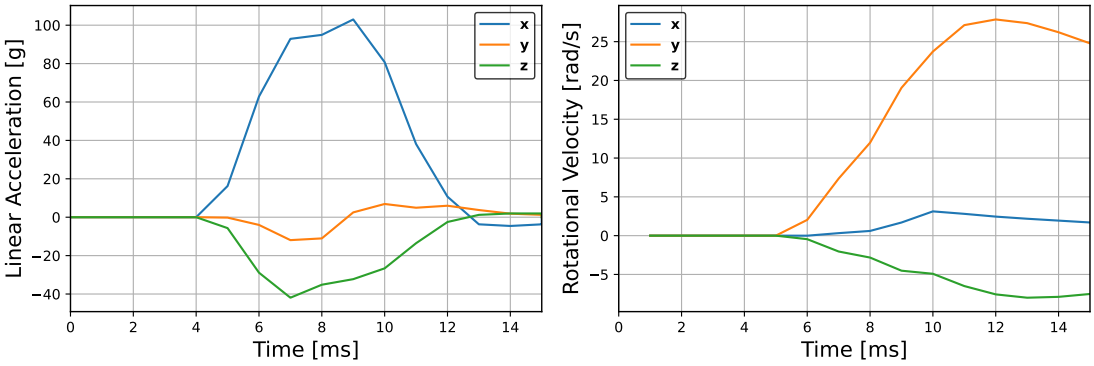

Figure A.6: Impact kinematics for a moving Hybrid III dummy impact, showcasing the linear acceleration and rotational velocity components

Appendix B

Clustering

B.1 Implemented Code

```
import pandas as pd
import numpy as np
import matplotlib.pyplot as plt
import os
import skfuzzy as fuzz

from numpy.fft import fft, ifft, fftfreq, fftshift
from sklearn.cluster import KMeans
from sklearn.decomposition import PCA
from scipy import integrate

import matplotlib as mpl
from yellowbrick.cluster import SilhouetteVisualizer
from yellowbrick.cluster import KElbowVisualizer


# Import Data files into variables

linx_files = os.listdir(r'C:\Users\Uni\OneDrive - University of
    Edinburgh\newFEData\textfiles\linx')
liny_files = os.listdir(r'C:\Users\Uni\OneDrive - University of
    Edinburgh\newFEData\textfiles\liny')
linz_files = os.listdir(r'C:\Users\Uni\OneDrive - University of
    Edinburgh\newFEData\textfiles\linz')
rotx_files = os.listdir(r'C:\Users\Uni\OneDrive - University of
    Edinburgh\newFEData\textfiles\rotx')
roty_files = os.listdir(r'C:\Users\Uni\OneDrive - University of
    Edinburgh\newFEData\textfiles\roty')
rotz_files = os.listdir(r'C:\Users\Uni\OneDrive - University of
    Edinburgh\newFEData\textfiles\rotz')

for i,j in zip(linx_files, range(len(linx_files))) :
    path = r'C:\Users\Uni\OneDrive - University of Edinburgh\newFEData\
    textfiles\linx\\'
```

```
28      globals()[i] = pd.read_csv(path + linx_files[j], header=None,
        skiprows=8, skipfooter=1, engine='python', sep=" ").fillna(0)
29
30  for i,j in zip(liny_files, range(len(liny_files))) :
31      path = r'C:\Users\Uni\OneDrive - University of Edinburgh\newFEData\
        textfiles\liny\\'
32      globals()[i] = pd.read_csv(path + liny_files[j], header=None,
        skiprows=8, skipfooter=1, engine='python', sep=" ").fillna(0)
33
34  for i,j in zip(linz_files, range(len(linz_files))) :
35      path = r'C:\Users\Uni\OneDrive - University of Edinburgh\newFEData\
        textfiles\linz\\'
36      globals()[i] = pd.read_csv(path + linz_files[j], header=None,
        skiprows=8, skipfooter=1, engine='python', sep=" ").fillna(0)
37
38  for i,j in zip(rotx_files, range(len(rotx_files))) :
39      path = r'C:\Users\Uni\OneDrive - University of Edinburgh\newFEData\
        textfiles\rotx\\'
40      globals()[i] = pd.read_csv(path + rotx_files[j], header=None,
        skiprows=8, skipfooter=1, engine='python', sep=" ").fillna(0)
41
42  for i,j in zip(roty_files, range(len(roty_files))) :
43      path = r'C:\Users\Uni\OneDrive - University of Edinburgh\newFEData\
        textfiles\roty\\'
44      globals()[i] = pd.read_csv(path + roty_files[j], header=None,
        skiprows=8, skipfooter=1, engine='python', sep=" ").fillna(0)
45
46  for i,j in zip(rotz_files, range(len(rotz_files))) :
47      path = r'C:\Users\Uni\OneDrive - University of Edinburgh\newFEData\
        textfiles\rotz\\'
48      globals()[i] = pd.read_csv(path + rotz_files[j], header=None,
        skiprows=8, skipfooter=1, engine='python', sep=" ").fillna(0)
49
50
51  # Compile all impacts into 6 dataframes, 3 linear acceleration and 3
        rotational velocities
52
53  dframe = ['linx', 'liny', 'linz', 'rotx', 'roty', 'rotz']
54  d_files = ['linx_files','liny_files','linz_files','rotx_files','
        roty_files','rotz_files',]
55
56
57
58
59  #append data is not the created data frames per direction
60  n = 272
61  for i,j in zip(dframe, d_files):
62      globals()[i] = pd.DataFrame(f_1linx.iloc[0:n,4])*0.001
```

```
63      for k in range(len(linx_files)):
64          var = globals()[j][k]
65          df_1 = pd.Series(globals()[var].iloc[0:n,7]+globals()[var].iloc
    [0:n,8])*1000
66          #df_1 = df - df.mean()
67          globals()[i] = pd.concat([globals()[i],df_1], axis=1)
68      labels = ['t'] + globals()[j]
69      globals()[i].columns = labels
70
71
72  fft_dframe = ['fftlinx', 'fftliny', 'fftlinz', 'fftrotx', 'fftroty', '
    fftrotz']
73
74  for i,j in zip(fft_dframe, dframe) :
75      T = 1.0 / 3200
76      Freq = pd.DataFrame(fftfreq(n, T)[:n//2])
77      globals()[i] = Freq
78      for k in range(1,len(rotx.columns),1):
79          yf = pd.DataFrame(fft(globals()[j].iloc[:,k]))
80          globals()[i][k] = 2.0/n * np.abs(yf[0:n//2])
81      globals()[i] = globals()[i].drop(labels=range(1), axis=1)    #
    dropping frequency for Kmeans
82
83  # Displacement of each signal
84  rot = ['rotx', 'roty', 'rotz']
85  lin = ['linx', 'liny', 'linz']
86
87  rot_disp = ['rotx_disp', 'roty_disp', 'rotz_disp']
88  lin_disp = ['linx_disp', 'liny_disp', 'linz_disp']
89
90  for i,j in zip(rot_disp, rot):
91      globals()[i] = pd.DataFrame([])
92      for k in range(1,len(rotx.columns),1):
93          globals()[i][k-1] = integrate.cumtrapz(globals()[j].iloc[:,k],
    globals()[j].iloc[:,0], initial=0)
94
95  for i,j in zip(lin_disp, lin):
96      globals()[i] = pd.DataFrame([])
97      for k in range(1,len(rotx.columns),1):
98          y_int = integrate.cumtrapz(globals()[j].iloc[:,k], globals()[j].
    iloc[:,0], initial=0)
99          globals()[i][k-1] = integrate.cumtrapz(y_int, globals()[j].iloc
    [:,0], initial=0)
100
101 # Compile features for Kmeans
102
103 lin_features = pd.concat([fftlinx,fftliny,fftlinz])
104 lin_features = lin_features.div(lin_features.max())
```

```
105 rot_features = pd.concat([fftrotx, fftroty, fftrotz])
106 rot_features = rot_features.div(rot_features.max())
107
108 fft_features = pd.concat([lin_features, rot_features])
109 fft_features = fft_features.reset_index(drop=True)
110 fft_features = fft_features.T
111 fft_features = fft_features.reset_index(drop=True)
112
113 s = 65
114 c = 65
115 lin_disp_features = pd.concat([linx_disp.iloc[c],liny_disp.iloc[c],
        linz_disp.iloc[c]], axis=1)
116 lin_disp_features = lin_disp_features.div(abs(lin_disp_features).max(
        axis=1), axis=0)
117 rot_disp_features1 = pd.concat([rotx_disp.iloc[s],roty_disp.iloc[s],
        rotz_disp.iloc[s]], axis=1)
118 rot_disp_features = rot_disp_features1.div(abs(rot_disp_features1).max(
        axis=1), axis=0)
119
120 s2 = 90
121 c2 = 90
122 lin_disp_features2 = pd.concat([linx_disp.iloc[c2],liny_disp.iloc[c2],
        linz_disp.iloc[c2]], axis=1)
123 lin_disp_features2 = lin_disp_features2.div(abs(lin_disp_features2).max(
        axis=1), axis=0)
124 rot_disp_features2 = pd.concat([rotx_disp.iloc[s2],roty_disp.iloc[s2],
        rotz_disp.iloc[s2]], axis=1)
125 rot_disp_features2 = rot_disp_features2.div(abs(rot_disp_features2).max(
        axis=1), axis=0)
126
127 disp_features = pd.concat([lin_disp_features,rot_disp_features], axis=1)
128 disp_features2 = pd.concat([lin_disp_features2,rot_disp_features2], axis
        =1)
129
130 nan_rows = disp_features[disp_features.isna().any(axis=1)].index
131 disp_features.loc[nan_rows] = disp_features2.loc[nan_rows]
132
133
134 features = pd.concat([fft_features, disp_features], axis=1)
135 features.columns = range(features.shape[1])
136
137 Km = KMeans(n_clusters=6)
138 clusters = pd.DataFrame(Km.fit_predict(features), columns = ['clusters'
        ])
139
140
141 df = features
142 pca = PCA(n_components=2)
```

```
143 principalComponents = pca.fit_transform(df)
144 principalDf = pd.DataFrame(data = principalComponents
145              , columns = ['principal component 1', 'principal component
    2'])
146 finalDf = pd.concat([principalDf, clusters[['clusters']]], axis = 1)
147 print(finalDf)
148
149
150 #C means Clustering
151
152 cntr_f, u_f, u0_f,d_f,jm_f,p_f,fpc_f= fuzz.cluster.cmeans(
153         features.T, 6, 2, error=0.005, maxiter=1000, init=None)
```

Listing B.1: Clustering algorithm implementation

B.2 Kinematic Output

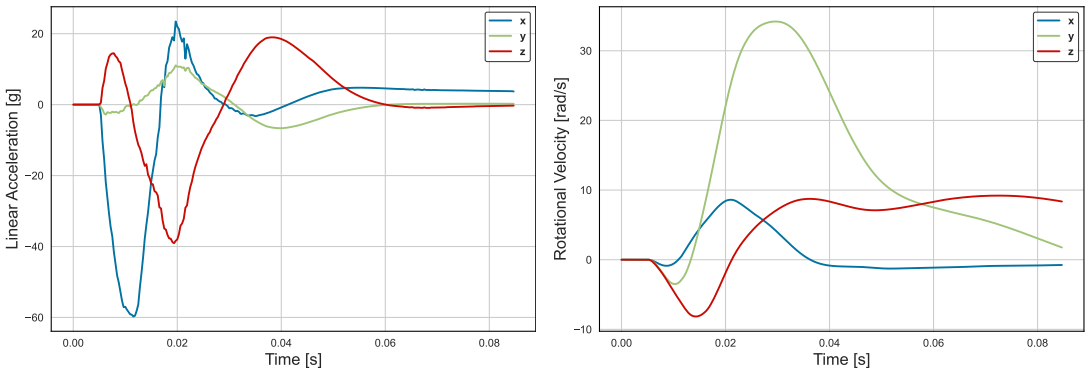

Figure B.1: Example impact kinematics for a "Front" impact, showcasing the Linear acceleration and rotational velocity components

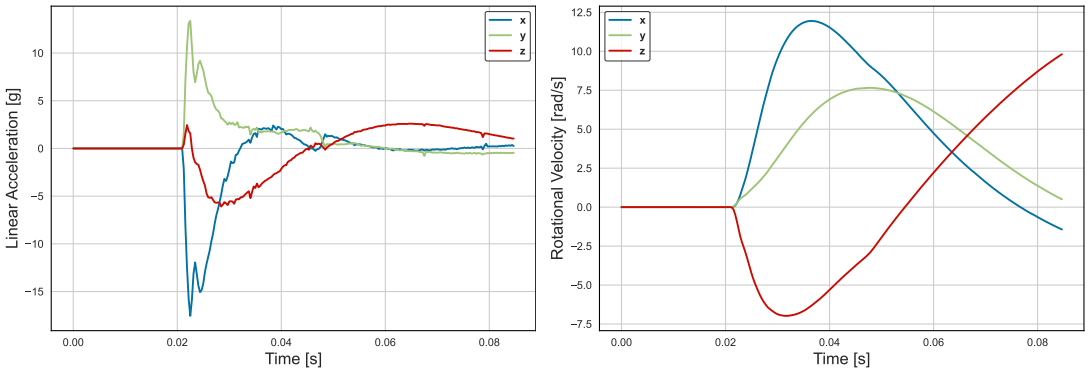

Figure B.2: Example impact kinematics for a "Right Front" impact, showcasing the Linear acceleration and rotational velocity components

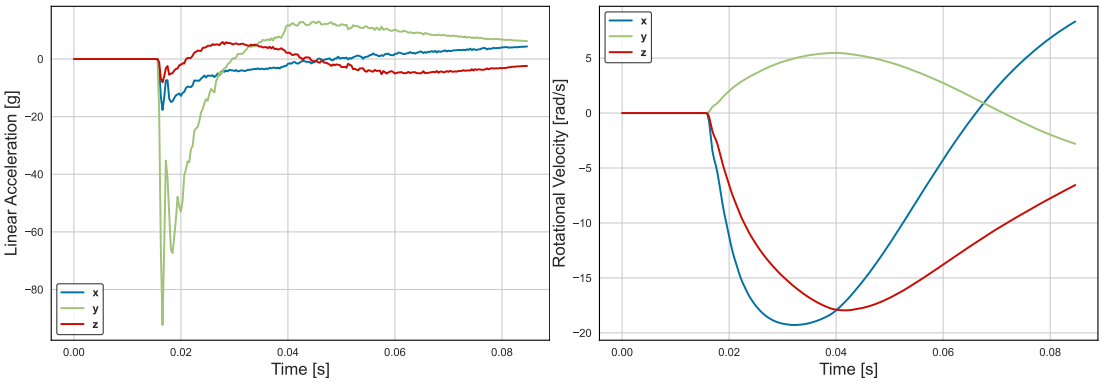

Figure B.3: Example impact kinematics for a "Right Lower" impact, showcasing the Linear acceleration and rotational velocity components

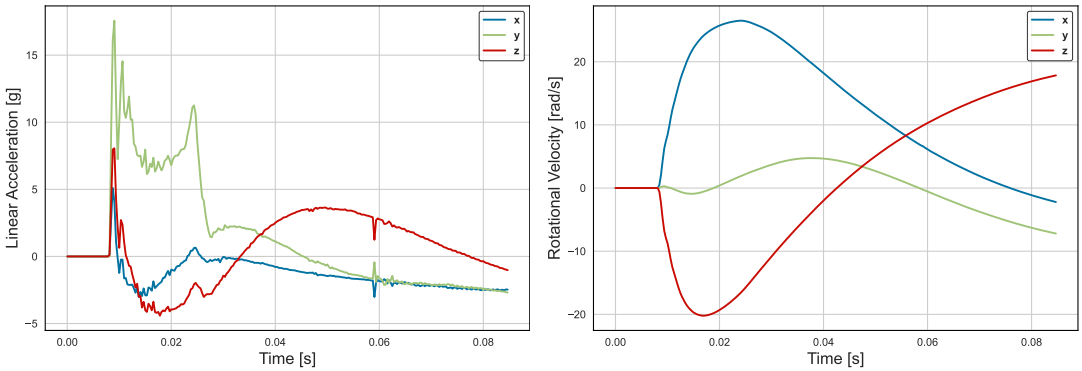

Figure B.4: Example impact kinematics for a "Right" impact,showcasing the Linear acceleration and rotational velocity components

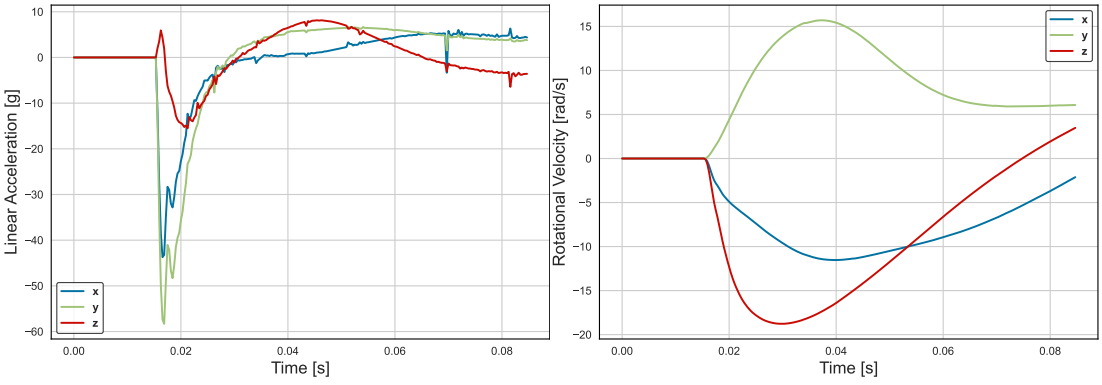

Figure B.5: Example impact kinematics for a "Left Front" impact, showcasing the Linear acceleration and rotational velocity components

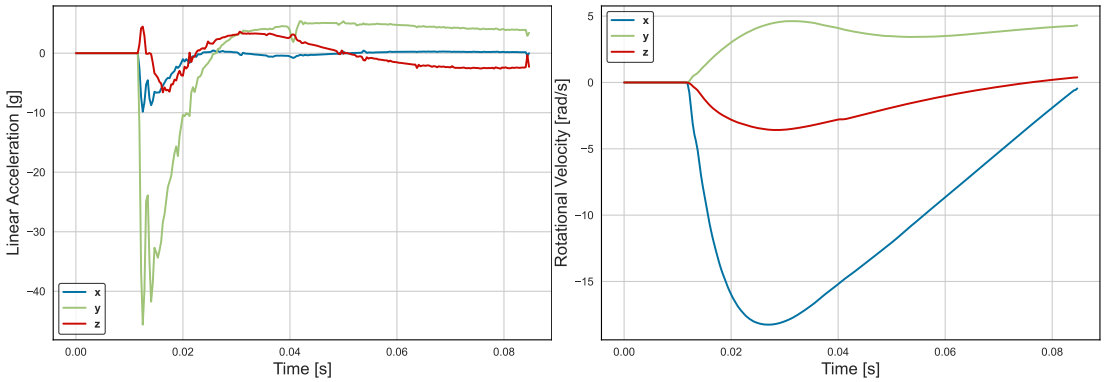

Figure B.6: Example impact kinematics for a "Left" impact, showcasing the Linear acceleration and rotational velocity components

Bibliography

Acharya, J., & Basu, A. (2020). Deep neural network for respiratory sound classification in wearable devices enabled by patient specific model tuning. *IEEE transactions on biomedical circuits and systems*, *14*(3), 535–544.

Alizadehsani, R., Khosravi, A., Roshanzamir, M., Abdar, M., Sarrafzadegan, N., Shafie, D., ... others (2021). Coronary artery disease detection using artificial intelligence techniques: A survey of trends, geographical differences and diagnostic features 1991–2020. *Computers in Biology and Medicine*, *128*, 104095.

Allison, M. A., Kang, Y. S., Bolte, J. H., Maltese, M. R., Arbogast, K. B., et al. (2014). Validation of a helmet-based system to measure head impact biomechanics in ice hockey. *Medicine and science in sports and exercise*, *46*(1), 115–123.

Bartsch, A., Benzel, E., Miele, V., & Prakash, V. (2012). Impact test comparisons of 20th and 21st century american football helmets. *Journal of neurosurgery*, *116*(1), 222–233.

Bartsch, A., Samorezov, S., Benzel, E., Miele, V., & Brett, D. (2014). *Validation of an "intelligent mouthguard" single event head impact dosimeter* (Tech. Rep.). SAE Technical Paper.

Beckwith, J. G., Greenwald, R., & Chu, J. J. (2012). Measuring head kinematics in football: correlation between the head impact telemetry system and hybrid iii headform. *Annals of biomedical engineering*, *40*(1), 237–248.

Benaroya, H., & Rehak, M. (1988). Finite element methods in probabilistic structural analysis: a selective review.

Borthakur, D., Dubey, H., Constant, N., Mahler, L., & Mankodiya, K. (2017). Smart fog: Fog computing framework for unsupervised clustering analytics in wearable internet of things. In *2017 ieee global conference on signal and information processing (globalsip)* (pp. 472–476).

Bosch, S., Shoaib, M., Geerlings, S., Buit, L., Meratnia, N., & Havinga, P. (2015). Analysis of indoor rowing motion using wearable inertial sensors. In *Proceedings of the 10th eai international conference on body area networks* (pp. 233–239).

Brolinson, P. G., Manoogian, S., McNeely, D., Goforth, M., Greenwald, R., & Duma, S. (2006). Analysis of linear head accelerations from collegiate football impacts. *Current sports medicine reports*, *5*(1), 23–28.

Cajigal, S. (2007). Brain damage may have contributed to former wrestler's violent demise. *Neurology Today*, *7*(18), 1–16.

Camarillo, D. B., Shull, P. B., Mattson, J., Shultz, R., & Garza, D. (2013). An instrumented mouthguard for measuring linear and angular head impact kinematics in american football. *Ann Biomed Eng*, *41*(9), 1939–1949.

Caruana, R., & Niculescu-Mizil, A. (2006). An empirical comparison of supervised learning algorithms. In *Proceedings of the 23rd international conference on machine learning* (pp. 161–168).

Caswell, S. V., Cortes, N., Mitchell, K., Liotta, L., & Petricoin, E. F. (2015). Development of nanoparticle-enabled protein biomarker discovery: implementation for saliva-based traumatic brain injury detection. In *Advances in salivary diagnostics* (pp. 121–129). Springer.

Chan, H. S. (1974). Mathematical model for closed head impact. *SAE Transactions*, 3814–3825.

Chen, X., & Liu, Y. (2018). *Finite element modeling and simulation with ansys workbench*. CRC press.

Chhikara, K. (2021, Jul). *K-means clustering from scratch in python.* Medium. Retrieved from `https://chhikarakunal96.medium.com/k-means-clustering-from-scratch-in-python-ff2c681b73be`

Colantonio, A., Mroczek, D., Patel, J., Lewko, J., Fergenbaum, J., & Brison, R. (2010). Examining occupational traumatic brain injury in ontario. *Canadian journal of public health*, *101*(1), S58–S62.

Crisco, J., Chu, J., & Greenwald, R. (2004). An algorithm for estimating acceleration magnitude and impact location using multiple nonorthogonal single-axis accelerometers. *J. Biomech. Eng.*, *126*(6), 849–854.

Crisco, J., Fiore, R., Beckwith, J. G., Chu, J. J., Brolinson, P. G., Duma, S., ... Greenwald, R. M. (2010). Frequency and location of head impact exposures in individual collegiate football players. *Journal of athletic training*, *45*(6), 549–559.

Decker, W., Baker, A., Ye, X., Brown, P., Stitzel, J., & Gayzik, F. S. (2020). Development and multi-scale validation of a finite element football helmet model. *Annals of biomedical engineering*, *48*(1), 258–270.

De Kruijk, J., Leffers, P., Menheere, P., Meerhoff, S., Rutten, J., & Twijnstra, A. (2002). Prediction of post-traumatic complaints after mild traumatic brain injury: early symptoms and biochemical markers. *Journal of Neurology, Neurosurgery & Psychiatry*, *73*(6), 727–732.

Deng, Y.-C., & Goldsmith, W. (1987). Response of a human head/neck/upper-torso replica to dynamic loading—ii. analytical/numerical model. *J. Biomech.*, *20*(5), 487–497.

Domingos, P. (2015). *The master algorithm: How the quest for the ultimate learning machine will remake our world*. Basic Books.

Duan, Y., Wang, S., & Yau, J. (2019). Vector form intrinsic finite element method for analysis of train–bridge interaction problems considering the coach-coupler effect. *International Journal of Structural Stability and Dynamics*, *19*(02), 1950014.

Duma, S., Crandall, J., Rudd, R. W., & Kent, R. (2003). Small female head and neck interaction with a deploying side airbag. *Accident Analysis & Prevention*, *35*(5), 811–816.

Esteva, A., Kuprel, B., Novoa, R. A., Ko, J., Swetter, S. M., Blau, H. M., & Thrun, S. (2017). Dermatologist-level classification of skin cancer with deep neural networks. *nature*, *542*(7639), 115–118.

Evans, R. W. (1994). The postconcussion syndrome: 130 years of controversy. In *Seminars in neurology* (Vol. 14, pp. 32–39).

Fanton, M., Gaudio, N., & Ling, A. (n.d.). Neural network for detecting head impacts from kinematic data.

FIT. (2014). *Force impact technologies.* Retrieved from `https://fitguard.me/`

Foster, J. K., Kortge, J. O., & Wolanin, M. J. (1977). Hybrid iii—a biomechanically-based crash test dummy. *SAE Transactions*, 3268–3283.

Friedman, K., Hutchinson, J., & Mihora, D. (2007). Finite element modeling of rollover crash tests with hybrid iii dummies. In *Summer bioengineering conference* (Vol. 47985, pp. 611–612).

Fuller, C. W., Taylor, A., & Raftery, M. (2015). Epidemiology of concussion in men's elite rugby-7s (sevens world series) and rugby-15s (rugby world cup, junior world championship and rugby trophy, pacific nations cup and english premiership). *British journal of sports medicine*, *49*(7), 478–483.

Funk, J. R., Rowson, S., Daniel, R. W., & Duma, S. M. (2012). Validation of concussion risk curves for collegiate football players derived from hits data. *Annals of biomedical engineering*, *40*(1), 79–89.

Geddes, J., Vowles, G., Nicoll, J., & Revesz, T. (1999). Neuronal cytoskeletal changes are an early consequence of repetitive head injury. *Acta neuropathologica*, *98*(2), 171–178.

Gennarelli, T. A., Pintar, F. A., & Yoganandan, N. (2003). Biomechanical tolerances for diffuse brain injury and a hypothesis for genotypic variability in response to trauma. In *Annual proceedings/association for the advancement of automotive medicine* (Vol. 47, p. 624).

Gennarelli, T. A., Thibault, L., & Ommaya, A. (1972). Pathophysiologic responses to rotational and translational accelerations of the head. In *Proceedings: Stapp car crash conference* (Vol. 16).

Gennarelli, T. A., Thibault, L. E., Adams, J. H., Graham, D. I., Thompson, C. J., & Marcincin, R. P. (1982). Diffuse axonal injury and traumatic coma in the primate. *Annals of Neurology: Official Journal of the American Neurological Association and the Child Neurology Society*, *12*(6), 564–574.

Gennarelli, T. A., Thibault, L. E., Tomei, G., Wiser, R., Graham, D., & Adams, J. (1987). Directional dependence of axonal brain injury due to centroidal and non-centroidal acceleration. *SAE Transactions*, 1355–1359.

Gessel, L. M., Fields, S. K., Collins, C. L., Dick, R. W., & Comstock, R. D. (2007). Concussions among united states high school and collegiate athletes. *Journal of athletic training*, *42*(4), 495.

Giudice, J. S., Park, G., Kong, K., Bailey, A., Kent, R., & Panzer, M. B. (2019). Development of open-source dummy and impactor models for the assessment of american football helmet finite element models. *Annals of biomedical engineering*, *47*, 464–474.

Gupta, R., Gupta, A., & Aswal, R. (2021). Detection of poor posture using wearable sensors and unsupervised learning. In *2021 7th international conference on advanced computing and communication systems (icaccs)* (Vol. 1, pp. 527–531).

Gurdjian, E., & Lissner, H. (1944). Mechanism of head injury as studied by the cathode ray oscilloscope preliminary report. *Journal of Neurosurgery*, *1*(6), 393–399.

Gurdjian, E., & Webster, J. (1943). Experimental head injury with special reference to the mechanical factors in acute trauma. *Surg. Gynec. Obstet*, *76*, 623–634.

Gurdjian, E. S., Lissner, H., & Patrick, L. (1963). Concussion: mechanism and pathology. In *Proceedings: American association for automotive medicine annual conference* (Vol. 7, pp. 470–482).

Guskiewicz, K. M., Marshall, S. W., Bailes, J., McCrea, M., Cantu, R. C., Randolph, C., & Jordan, B. D. (2005). Association between recurrent concussion and late-life cognitive impairment in retired professional football players. *Neurosurgery*, *57*(4), 719–726.

Guskiewicz, K. M., Marshall, S. W., Bailes, J., McCrea, M., Harding, H. P., Matthews, A., ... Cantu, R. C. (2007). Recurrent concussion and risk of depression in retired professional football players. *Medicine and science in sports and exercise*, *39*(6), 903.

Guskiewicz, K. M., Mihalik, J. P., Shankar, V., Marshall, S. W., Crowell, D. H., Oliaro, S. M., ... Hooker, D. N. (2007). Measurement of head impacts in collegiate football players: relationship between head impact biomechanics and acute clinical outcome after concussion. *Neurosurgery*, *61*(6), 1244–1253.

Hardy, C. H., & Marcal, P. V. (1973). Elastic analysis of a skull.

Hecimovich, M., King, D., Dempsey, A., Gittins, M., & Murphy, M. (2018). Youth australian footballers experience similar impact forces to the head as junior-and senior-league players: a prospective study of kinematic measurements. *J. Sports Sci, Med.*, *17*(4), 547.

Hernandez, F., Wu, L. C., Yip, M. C., Laksari, K., Hoffman, A. R., Lopez, J. R., ... Camarillo, D. B. (2015). Six degree-of-freedom measurements of human mild traumatic brain injury. *Ann Biomed Eng*, *43*(8), 1918–1934.

Hibbeler, R. (2004). *Engineering mechanics: dynamics*. Pearson Educación.

Hodgson, V., Thomas, L. M., Gurdjian, E., Fernando, O., Greenberg, S., & Chason, J. (1969). Advances in understanding of experimental concussion mechanisms.

Hoge, C. W., McGurk, D., Thomas, J. L., Cox, A. L., Engel, C. C., & Castro, C. A. (2008). Mild traumatic brain injury in us soldiers returning from iraq. *New England journal of medicine*, *358*(5), 453–463.

Hootman, J. M., Dick, R., & Agel, J. (2007). Epidemiology of collegiate injuries for 15 sports: summary and recommendations for injury prevention initiatives. *Journal of athletic training*, *42*(2), 311.

Horgan, T. J., & Gilchrist, M. D. (2003). The creation of three-dimensional finite element models for simulating head impact biomechanics. *International Journal of Crashworthiness*, *8*(4), 353–366.

Huang, M.-X., Nichols, S., Robb, A., Angeles, A., Drake, A., Holland, M., ... others (2012). An automatic meg low-frequency source imaging approach for detecting injuries in mild and moderate tbi patients with blast and non-blast causes. *Neuroimage*, *61*(4), 1067–1082.

Jadischke, R., Viano, D. C., Dau, N., King, A. I., & McCarthy, J. (2013). On the accuracy of the head impact telemetry (hit) system used in football helmets. *Journal of biomechanics*, *46*(13), 2310–2315.

JE, W., & HR, L. (1955). Observations on the mechanism of brain concussion, contusion, and laceration. *Surgery, gynecology & obstetrics*, *101*(6), 680–690.

Jellinger, K. A. (2004). Head injury and dementia. *Current opinion in neurology*, *17*(6), 719–723.

Jones, B., Tooby, J., Weaving, D., Till, K., Owen, C., Begonia, M., ... others (2022). Ready for impact? a validity and feasibility study of instrumented mouthguards (imgs). *British journal of sports medicine*, *56*(20), 1171–1179.

Jones, C. M., Austin, K., Augustus, S. N., Nicholas, K. J., Yu, X., Baker, C., ... Ghajari, M. (2023). An instrumented mouthguard for real-time measurement of head kinematics under a large range of sport specific accelerations. *Sensors*, *23*(16), 7068.

Jones, D. A., Gaewsky, J. P., Saffarzadeh, M., Putnam, J. B., Weaver, A. A., Somers, J. T., & Stitzel, J. D. (2019). Multidirection validation of a finite element 50th percentile male hybrid iii anthropomorphic test device for spaceflight applications. *Journal of biomechanical engineering*, *141*(3).

Jowitt, H. K., Durussel, J., Brandon, R., & King, M. (2020). Auto detecting deliveries in elite cricket fast bowlers using microsensors and machine learning. *Journal of sports sciences*, *38*(7), 767–772.

Kan, C.-D., Marzougui, D., & Bedewi, N. E. (2003). Development of a 50th percentile hybrid iii dummy model. In *Proceedings of the fourth european ls-dyna users conference, ulm, germany* (pp. 22–23).

Kang, H.-S., Willinger, R., Diaw, B. M., & Chinn, B. (1997). Validation of a 3d anatomic human head model and replication of head impact in motorcycle accident by finite element modeling. *SAE transactions*, 3849–3858.

Kang, S., & Xiao, P. (2008). Comparison of hybrid iii rigid body dummy models. In *10th international lsdyna users conference.*

Kenner, V., & Goldsmith, W. (1972). Dynamic loading of a fluid-filled spherical shell. *International Journal of Mechanical Sciences*, *14*(9), 557–568.

Kerr, H. A., Curtis, C., Micheli, L. J., Kocher, M. S., Zurakowski, D., Kemp, S., & Brooks, J. (2008). Collegiate rugby union injury patterns in new england: a prospective cohort study. *British journal of sports medicine*, *42*(7), 595–603.

Khalil, T. B., & Hubbard, R. P. (1977). Parametric study of head response by finite element modeling. *Journal of Biomechanics*, *10*(2), 119–132.

Kieffer, E. E., Vaillancourt, C., Brolinson, P. G., & Rowson, S. (2020). Using in-mouth sensors to measure head kinematics in rugby. In *Ircobi conference* (Vol. 13, pp. 846–58).

King, A. I., Yang, K. H., Zhang, L., Hardy, W., & Viano, D. C. (2003). Is head injury caused by linear or angular acceleration. In *Ircobi conference* (Vol. 12).

King, D., Hume, P., Clark, T., Tarvirdizade, K., & Hind, K. (2024). Head impacts measured with a monitoring mouthguard for an amateur women's rugby union team in new zealand. *J Clin Images Med Case Rep*, *5*(2), 2889.

King, D., Hume, P., Gissane, C., Brughelli, M., & Clark, T. (2016). The influence of head impact threshold for reporting data in contact and collision sports: systematic review and original data analysis. *Sports medicine*, *46*(2), 151–169.

King, D., Hume, P., Gissane, C., & Clark, T. (2017). Measurement of head impacts in a senior amateur rugby league team with an instrumented patch: Exploratory analysis. *ARC J. Res. Sports Med.*, *2*(1), 9–20.

King, D., Hume, P. A., Brughelli, M., & Gissane, C. (2015). Instrumented mouthguard acceleration analyses for head impacts in amateur rugby union players over a season of matches. *Am. J. Med.*, *43*(3), 614–624.

Kleiven, S., & Hardy, W. N. (2002). Correlation of an fe model of the human head with local brain motion: consequences for injury prediction. *Stapp car crash journal*, *46*, 123–144.

Kristman, V. L., Cote, P., Hogg-Johnson, S., Cassidy, J. D., Eerd, D. V., Vidmar, M., ... Wennberg, R. A. (2010). The burden of work disability associated with mild traumatic brain injury in ontario compensated workers: a prospective cohort study. *The Open Occupational Health & Safety Journal*, *2*(1).

Kuo, C., Wu, L., Loza, J., Senif, D., Anderson, S. C., & Camarillo, D. B. (2018). Comparison of video-based and sensor-based head impact exposure. *PloS one*, *13*(6), e0199238.

Laker, S. R. (2011). Epidemiology of concussion and mild traumatic brain injury. *PM&R*, *3*, S354–S358.

Lincoln, A. E., Caswell, S. V., Almquist, J. L., Dunn, R. E., Norris, J. B., & Hinton, R. Y. (2011). Trends in concussion incidence in high school sports: a prospective 11-year study. *The American journal of sports medicine*, *39*(5), 958–963.

Liu, Y., Domel, A. G., Yousefsani, S. A., Kondic, J., Grant, G., Zeineh, M., & Camarillo, D. B. (2020). Validation and comparison of instrumented mouthguards for measuring head kinematics and assessing brain deformation in football impacts. *Annals of Biomedical Engineering*, *48*(11), 2580–2598.

LLC, B. (2024). Biocore hybrid iii finite element model [Computer software manual]. (Available from: `https://biocorellc.com/resources/finite-element-models`)

Löwenhielm, P. (1975). Mathematical simulation of gliding contusions. *Journal of biomechanics*, *8*(6), 351–356.

LSTC. (2014). *Ls-dyna keyword user's manual - volume i i - material models - r7.* Retrieved from https://ftp.lstc.com/anonymous/outgoing/jday/manuals/LS-DYNA_manual_Vol_II_R7.1.pdf

Lundin, A., de Boussard, C., Edman, G., & Borg, J. (2006). Symptoms and disability until 3 months after mild tbi. *Brain Injury*, *20*(8), 799–806.

Luo, Z., & Goldsmith, W. (1991). Reaction of a human head/neck/torso system to shock. *J. Biomech.*, *24*(7), 499–510.

Mahon, N. (2014). *This is rugby in america.* ESPN Internet Ventures. Retrieved from http://www.espn.com/espn/photos/gallery/_/id/11816568/image/1/in-middle-maul-rugby-america

Marques, E. S., Silva, F. J., & Pereira, A. B. (2020). Comparison of finite element methods in fusion welding processes—a review. *Metals*, *10*(1), 75.

Marshall, S. W., & Spencer, R. J. (2001). Concussion in rugby: the hidden epidemic. *Journal of athletic training*, *36*(3), 334.

McCrory, P., Meeuwisse, W., Dvorak, J., Aubry, M., Bailes, J., Broglio, S., ... others (2017). Consensus statement on concussion in sport—the 5th international conference on concussion in sport held in berlin, october 2016. *British journal of sports medicine*, *51*(11), 838–847.

McGinnis, R., Cain, S. M., Davidson, S. P., Vitali, R. V., McLean, S. G., & Perkins, N. C. (2017). Inertial sensor and cluster analysis for discriminating agility run technique and quantifying changes across load. *Biomedical Signal Processing and Control*, *32*, 150–156.

McGrath, J., Neville, J., Stewart, T., Clinning, H., & Cronin, J. (2021). Can an inertial measurement unit (imu) in combination with machine learning measure fast bowling speed and perceived intensity in cricket? *Journal of Sports Sciences*, *39*(12), 1402–1409.

McIntosh, A. S., McCrory, P., & Comerford, J. (2000). The dynamics of concussive head impacts in rugby and australian rules football. *Med. Sci. Sports Exercise*, *32*(12), 1980–1984.

McKee, A. C., Cantu, R. C., Nowinski, C. J., Hedley-Whyte, E. T., Gavett, B. E., Budson, A. E., ... Stern, R. A. (2009). Chronic traumatic encephalopathy in athletes: progressive tauopathy after repetitive head injury. *Journal of Neuropathology & Experimental Neurology*, *68*(7), 709–735.

Meehan, W. P., d'Hemecourt, P., & Dawn Comstock, R. (2010). High school concussions in the 2008-2009 academic year: mechanism, symptoms, and management. *The American journal of sports medicine*, *38*(12), 2405–2409.

Mejia-Ricart, L. F., Helling, P., & Olmsted, A. (2017). Evaluate action primitives for human activity recognition using unsupervised learning approach. In *2017 12th international conference for internet technology and secured transactions (icitst)* (pp. 186–188).

Menon, D. K., Schwab, K., Wright, D. W., Maas, A. I., et al. (2010). Position statement: definition of traumatic brain injury. *Archives of physical medicine and rehabilitation*, *91*(11), 1637–1640.

Meriam, J. L., Kraige, L. G., & Bolton, J. N. (2020). *Engineering mechanics: dynamics*. John Wiley & Sons.

Mertz, H. J., & Patrick, L. M. (1971). Strength and response of the human neck. *SAE transactions*, 2903–2928.

Mertz Jr, H., & Patrick, L. M. (1968). Investigation of the kinematics and kinetics of whiplash. *SAE Transactions*, 2952–2980.

Mohan, P., Park, C.-K., Marzougui, D., Kan, C.-D., Guha, S., Maurath, C., & Bhalsod, D. (2010). Lstc/ncac dummy model development. In *11th international ls-dyna users conference.*

Ngai, E. W., Hu, Y., Wong, Y. H., Chen, Y., & Sun, X. (2011). The application of data mining techniques in financial fraud detection: A classification framework and an academic review of literature. *Decision support systems*, *50*(3), 559–569.

O'Connor, K. L., Rowson, S., Duma, S. M., & Broglio, S. P. (2017). Head-impact–measurement devices: a systematic review. *Journal of athletic training*, *52*(3), 206–227.

Ommaya, A. K., & Gennarelli, T. (1974). Cerebral concussion and traumatic unconsciousness: correlation of experimental and clinical observations on blunt head injuries. *Brain*, *97*(4), 633–654.

Ono, K., Kikuchi, A., Nakamura, M., Kobayashi, H., & Nakamura, N. (1980). Human head tolerance to sagittal impact—reliable estimation deduced from experimental head injury using subhuman primates and human cadaver skulls. *SAE Transactions*, 3837–3866.

Panjabi, M. M. (1973). Three-dimensional mathematical model of the human spine structure. *J. Biomech.*, *6*(6), 671–680.

Pellman, E., Viano, D. C., Tucker, A. M., Casson, I. R., & Waeckerle, J. F. (2003). Concussion in professional football: reconstruction of game impacts and injuries. *Neurosurgery*, *53*(4), 799–814.

Pellman, E., Viano, D. C., Withnall, C., Shewchenko, N., Bir, C. A., & Halstead, P. D. (2006). Concussion in professional football: helmet testing to assess impact performance—part 11. *Neurosurgery*, *58*(1), 78–95.

Pfister, T., Pfister, K., Hagel, B., Ghali, W. A., & Ronksley, P. E. (2016). The incidence of concussion in youth sports: a systematic review and meta-analysis. *Br. J. Sports Med.*, *50*(5), 292–297.

Post, A., & Blaine Hoshizaki, T. (2015). Rotational acceleration, brain tissue strain, and the relationship to concussion. *Journal of biomechanical engineering*, *137*(3).

Post, A., Hoshizaki, T. B., Gilchrist, M. D., & Cusimano, M. D. (2017). Peak linear and rotational acceleration magnitude and duration effects on maximum principal strain in the corpus callosum for sport impacts. *Journal of biomechanics*, *61*, 183–192.

Prien, A., Grafe, A., Rössler, R., Junge, A., & Verhagen, E. (2018). Epidemiology of head injuries focusing on concussions in team contact sports: a systematic review. *Sports Med.*, *48*(4), 953–969.

Rahmzadeh, A., Alam, S., & Tremblay, R. (2018). Analytical prediction and finite-element simulation of the lateral response of rocking steel bridge piers with energy-dissipating steel bars. *Journal of Structural Engineering*, *144*(11), 04018210.

Rao, S. S. (2011). *Mechanical vibrations*. Prentice Hall.

Rees, A. (2020, Jun). *Rugby rules 101: What does "ruck" mean?* FloSports. Retrieved from `https://www.florugby.com/articles/6749489-rugby-rules-101-what-does-ruck-mean`

Rich, A., Filben, T., Miller, L., Tomblin, B., Van Gorkom, A. R., Hurst, M. A., ... Stitzel, J. D. (2019). Development, validation and pilot field deployment of a custom mouthpiece for head impact measurement. *Ann Biomed Eng*, *47*(10), 2109–2121.

Roe, G., Sawczuk, T., Owen, C., Tooby, J., Starling, L., Gilthorpe, M. S., ... others (2024). Head acceleration events during tackle, ball-carry, and ruck events in professional southern hemisphere men's rugby union matches: A study using instrumented mouthguards. *Scandinavian Journal of Medicine & Science in Sports*, *34*(6), e14676.

Rousseau, P., & Hoshizaki, T. (2009). The influence of deflection and neck compliance on the impact dynamics of a hybrid iii headform. *Proceedings of the Institution of Mechanical Engineers, Part P: Journal of Sports Engineering and Technology*, *223*(3), 89–97.

Rugby, W. (2019). *Global Reach of Rugby 2019* (Tech. Rep.). Author.

Russell, S., & Norvig, P. (2016). *Artificial intelligence: a modern approach*. Pearson.

Ryan, L., & Warden, D. L. (2003). Post concussion syndrome. *International review of psychiatry*, *15*(4), 310–316.

Saadatnejad, S., Oveisi, M., & Hashemi, M. (2019). Lstm-based ecg classification for continuous monitoring on personal wearable devices. *IEEE journal of biomedical and health informatics*, *24*(2), 515–523.

Samadani, U., Ritlop, R., Reyes, M., Nehrbass, E., Li, M., Lamm, E., ... others (2015). Eye tracking detects disconjugate eye movements associated with structural traumatic brain injury and concussion. *Journal of neurotrauma*, *32*(8), 548–556.

Schnebel, B., Gwin, J. T., Anderson, S., & Gatlin, R. (2007). In vivo study of head impacts in football: a comparison of national collegiate athletic association division i versus high school impacts. *Neurosurgery*, *60*(3), 490–496.

Schulz, M., Marshall, S. W., Mueller, F. O., Yang, J., Weaver, N. L., Kalsbeek, W. D., & Bowling, J. M. (2004). Incidence and risk factors for concussion in high school athletes, north carolina, 1996–1999. *American journal of epidemiology*, *160*(10), 937–944.

Shaw, N. (2002). The neurophysiology of concussion. *Progress in neurobiology*, *67*(4), 281–344.

Shuck, L., & Advani, S. (1972). Rheological response of human brain tissue in shear.

Shugar, T. (1975). Transient structural response of the linear skull-brain system. In *Proceedings: Stapp car crash conference* (Vol. 19, pp. 581–614).

Siegmund, G., Guskiewicz, K. M., Marshall, S. W., DeMarco, A. L., & Bonin, S. J. (2014a). A headform for testing helmet and mouthguard sensors that measure head impact severity in football players. *Annals of biomedical engineering*, *42*, 1834–1845.

Siegmund, G., Guskiewicz, K. M., Marshall, S. W., DeMarco, A. L., & Bonin, S. J. (2014b). A headform for testing helmet and mouthguard sensors that measure head impact severity in football players. *Ann. Biomed. Eng.*, *42*(9), 1834–1845.

Sohail, J., Teixeira-Dias, F., & Merriman, S. (2022). Head impacts in non-helmeted sports: Measuring and locating the impact force. *Proceedings of the Institution of Mechanical Engineers, Part P: Journal of Sports Engineering and Technology*, 17543371221130894.

Song, Y. (2019). Finite-element implementation of piezoelectric energy harvesting system from vibrations of railway bridge. *Journal of Energy Engineering*, *145*(2), 04018076.

Stemper, B., & Pintar, F. A. (2014). Biomechanics of concussion. *Concussion*, *28*, 14–27.

Takhounts, E., Eppinger, R. H., Campbell, J. Q., Tannous, R. E., Power, E. D., & Shook, L. S. (2003). *On the development of the simon finite element head model* (Tech. Rep.). SAE Technical Paper.

Tiernan, S., Byrne, G., & O'Sullivan, D. M. (2019). Evaluation of skin-mounted sensor for head impact measurement. *Proc. Inst. Mech. Eng., Part H*, *233*(7), 735–744.

Tooby, J., Weaving, D., Al-Dawoud, M., & Tierney, G. (2022). Quantification of head acceleration events in rugby league: an instrumented mouthguard and video analysis pilot study. *Sensors*, *22*(2), 584.

Tooby, J., Woodward, J., Tucker, R., Jones, B., Falvey, É., Salmon, D., ... Tierney, G. (2023). Instrumented mouthguards in elite-level men's and women's rugby union: the incidence and propensity of head acceleration events in matches. *Sports medicine*, 1–12.

Tooby, J., Woodward, J., Tucker, R., Jones, B., Falvey, É., Salmon, D., ... Tierney, G. (2024). Instrumented mouthguards in elite-level men's and women's rugby union: the incidence and propensity of head acceleration events in matches. *Sports medicine*, *54*(5), 1327–1338.

Tucker, R. (2017). Head injury events in rugby union: Description of high risk tackle events. *Br. J. Sports Med.*, *51*(4), 398–398.

Um, T., Babakeshizadeh, V., & Kulić, D. (2017). Exercise motion classification from large-scale wearable sensor data using convolutional neural networks. In *2017 ieee/rsj international conference on intelligent robots and systems (iros)* (pp. 2385–2390).

Unterharnscheidt, F. (1971). *Translational versus rotational acceleration-animal experiments with measured input* (Tech. Rep.). SAE Technical Paper.

Van Drunen, P. (2009). *Identification of a two pivot human neck model using linear anterior-posterior perturbations* (Unpublished master's thesis).

VanItallie, T. (2019). Traumatic brain injury (tbi) in collision sports: Possible mechanisms of transformation into chronic traumatic encephalopathy (cte). *Metab. Clin. Exp.*, *100*, 153943.

Waldron, M., Jones, C., Melotti, L., Brown, R., & Kilduff, L. P. (2021). Collision monitoring in elite male rugby union using a new instrumented mouth-guard. *J Sport Exerc Sci*, *5*(3), 179–87.

Weber, N., Härmä, A., & Heskes, E. P. D. T. (2017). *Unsupervised learning in human activity recognition: A first foray into clustering data gathered from wearable sensors* (Unpublished doctoral dissertation). Radboud University Nijmegen, The Netherlands.

Wilk, J., Thomas, J. L., McGurk, D. M., Riviere, L. A., Castro, C. A., & Hoge, C. W. (2010). Mild traumatic brain injury (concussion) during combat: lack of association of blast mechanism with persistent postconcussive symptoms. *The Journal of head trauma rehabilitation*, *25*(1), 9–14.

Willmott, C., McIntosh, A. S., Howard, T., Mitra, B., Dimech-Betancourt, B., Donovan, J., & Rosenfeld, J. V. (2018). Scat3 changes from baseline and associations with x2 patch measured head acceleration in amateur australian football players. *J. Sci. Med. Sport*, *21*(5), 442–446.

Wu, L. C., Nangia, V., Bui, K., Hammoor, B., Kurt, M., Hernandez, F., ... Camarillo, D. B. (2016). In vivo evaluation of wearable head impact sensors. *Ann Biomed Eng*, *44*(4), 1234–1245.

Wu, L. C., Zarnescu, L., Nangia, V., Cam, B., & Camarillo, D. B. (2014). A head impact detection system using svm classification and proximity sensing in an instrumented mouthguard. *IEEE Transactions on Biomedical Engineering*, *61*(11), 2659–2668.

Wu, S., Zhao, W., Ghazi, K., & Ji, S. (2019). Convolutional neural network for efficient estimation of regional brain strains. *Scientific reports*, *9*(1), 1–11.

Yuan, C., & Yang, H. (2019). Research on k-value selection method of k-means clustering algorithm. *J*, *2*(2), 226–235.

Zhan, X., Li, Y., Liu, Y., Cecchi, N. J., Gevaert, O., Zeineh, M. M., ... Camarillo, D. B. (2021). Kinematics clustering enables head impact subtyping for better traumatic brain injury prediction. *arXiv preprint arXiv:2108.03498*.

Zhan, X., Liu, Y., Cecchi, N. J., Gevaert, O., Zeineh, M. M., Grant, G. A., & Camarillo, D. B. (2021). Data-driven decomposition of brain dynamics with principal component analysis in different types of head impacts. *arXiv preprint arXiv:2110.14116*.

Zhan, X., Liu, Y., Raymond, S. J., Alizadeh, H. V., Domel, A. G., Gevaert, O., ... Camarillo, D. B. (2021). Rapid estimation of entire brain strain using deep learning models. *IEEE Transactions on Biomedical Engineering*, *68*(11), 3424–3434.

Zhang, J., Yoganandan, N., Pintar, F. A., & Gennarelli, T. A. (2006). Role of translational and rotational accelerations on brain strain in lateral head impact. *Biomed Sci Instrum*, *42*, 501–506.

Zhang, L., Yang, K. H., Dwarampudi, R., Omori, K., Li, T., Chang, K., ... King, A. I. (2001). Recent advances in brain injury research: a new human head model development and validation.

Zhang, L., Yang, K. H., & King, A. I. (2004). A proposed injury threshold for mild traumatic brain injury. *J. Biomech. Eng.*, *126*(2), 226–236.